Title

Tuning the Excitonic Properties of Two-Dimensional Molecular Aggregates Across the Visible and Shortwave Infrared

Author

Deshmukh, Arundhati Prakash

Publication Date

2021

Peer reviewed|Thesis/dissertation

UNIVERSITY OF CALIFORNIA

Los Angeles

Tuning the Excitonic Properties of Two-Dimensional Molecular Aggregates Across the Visible and Shortwave Infrared

A dissertation submitted in partial satisfaction of the

requirements for the degree Doctor of Philosophy

in Chemistry

by

Arundhati Prakash Deshmukh

2021

ABSTRACT OF THE DISSERTATION

Tuning the Excitonic Properties of

Two-Dimensional Molecular Aggregates

Across the Visible and Shortwave Infrared

by

Arundhati Prakash Deshmukh

Doctor of Philosophy in Chemistry

University of California, Los Angeles, 2021

Professor Justin Ryan Caram, Chair

Molecular aggregates are non-covalent self-assemblies of chromophores wherein excitations on individual molecules couple coherently over long distances. This leads to the formation of delocalized excitons with drastically altered photophysical properties from the monomers, including extreme blue or red shifts, narrow linewidths and high molar absorptivities. Kasha's model relates the observed blue or red shifts to the underlying molecular arrangements in 1-dimensional systems, known as H- or J-aggregates, respectively. In this dissertation, I explore how to modulate the excitonic couplings within an aggregate via molecular packing and topology in order to explore new photophysical behaviors. Chapter 1 covers the basic definitions, describes

the origins of the excitonic properties and the relevance towards various applications, and orients the readers to the overall goals of this dissertation.

In Chapter 2, we extend Kasha's model to 2-dimensional systems and show the unusual situation that arises from 2-dimensional (2D) transition dipole coupling in extended sheet-like aggregates. In addition to traditional H- and J-aggregation, we find a new case of 'I-aggregation' which shows intermediate characteristics of H- and J-aggregates. We demonstrate two examples of I-aggregates – extended 2D sheet aggregates of the dyes Cy7-Ph and Cy7-DPA, whose absorption spectra look quite like traditional J-aggregates but temperature dependence shows critical differences. This work shows the relative distance of the bright state from the band-edge can be tuned via relative slip between adjacent molecules, thus providing design principles to tune photophysical properties over a broader spectral range across visible (400 - 700 nm), near-infrared (NIR 700 - 1000 nm), and shortwave infrared (SWIR, 1000 - 2000 nm).

Chapter 3 provides insights on controlling the self-assembly of aggregates, achieving selective stabilization of H- or J-aggregate morphologies. Independent control of solvation conditions allows us to access a large aggregation phase space which can be modelled using a three-component equilibrium model. We obtain new insights into the self-assembly of the 2D aggregates. Mainly, the large sizes make the self-assembly highly cooperative and charge screening is important for stabilizing large aggregate morphologies. Such insights translate into general guidelines for thermodynamically controlling the aggregate self-assembly. We demonstrate this by aggregating several cyanine dyes into 2D sheet-like morphologies with narrow red shifted absorption spectra, enabling a library of 2D aggregates with absorptions spanning the visible and shortwave infrared (SWIR) regions.

In Chapter 4, we describe the subtle differences in the excitonic band structures across the aforementioned library of 2D aggregates. We show that various observables from absorption, emission and temperature dependent spectroscopy reveal the complex band structures of 2D aggregates, and thus form a comprehensive tool for probing excitonic band structures in general. With subtle control of geometric parameters such as length of the dye molecules and relative slip between adjacent molecules, we modify the excitonic band structure from mid-band I-aggregates that are weakly emissive to band-edge J-aggregates with high quantum yields and superradiance.

The above work demonstrates the importance of supramolecular packings within the aggregates in modulating the excitonic properties. A high resolution structure of the supramolecular aggregates will, therefore, pave the way for precise chemical design with desired excitonic properties. In Chapter 5, we present the first high-resolution cryo-electron microscopy structure of a prototypical tubular J-aggregate - double-walled light harvesting nanotubes (LHNs) of amphiphilic cyanine dye C8S3. We employ a cryogenic fixation technique to preserve the native structure, followed by a single particle analysis using the Iterative Helical Real Space Reconstruction (IHRSR) algorithm and obtain density maps of the inner wall at 3.3 Å resolution. Our structure shows a 3 dimer (6 monomers total) asymmetric unit with brick layer arrangement, as opposed to the previously thought herringbone arrangement. We uncover important structural features that were previously unknown, providing new pathways for chemical modulation of the supramolecular self-assemblies and thereby, the excitonic properties.

Several fundamental aspects about the structures and excitonic couplings remain open questions. Some of these challenges and experimental plans to address them are discussed in Chapter 6. Overall, this work establishes molecular aggregation as a tunable avenue for accessing unusual photophysical properties such as extreme spectral shifts, high SWIR quantum yields and

molar absorptivities, and narrow linewidths. Thereby, this work opens up organic chromophores to new functionalities including SWIR imaging, photonics, and telecommunications. Chemical modulation of exciton transport and practical applicability will be the main challenges to be addressed in the future. This work lays down the foundational principles that will enable researchers to approach such challenges.

The dissertation of Arundhati Prakash Deshmukh is approved.

Daniel Neuhauser

Benjamin Joel Schwartz

Ellen May Sletten

Justin Ryan Caram, Committee Chair

University of California, Los Angeles

2021

To my family, who has always stood with me.

TABLE OF CONTENTS

LIST OF FIGURES

LIST OF TABLES

ACKNOWLEDGEMENTS

I was naturally very nervous when I first came to UCLA. I moved to a new country all alone and started a challenging Ph.D. program. This journey would never be possible without the following individuals, whose support and togetherness was the strength I needed to accomplish this.

Let me start by thanking my advisor Justin Caram for all the knowledge and guidance imparted on to me. When I first met Justin during his interview process at UCLA, it was clear that our scientific interests aligned very well. Ever since then, working with Justin and setting up the new lab has been an exhilarating learning experience. He is such an encouraging and supportive mentor. Whenever I had trouble navigating a difficult situation, all I had to do was talk to him and he always had my back. I have also learnt from him, a great deal about being a professional scientist, be it launching numerous interdisciplinary collaborations or cultivating an open environment within the lab, all of which I hope to follow in my own lab someday.

I am grateful for the time and expertise of the rest of my committee members – Danny Neuhauser, Ben Schwartz, and Ellen Sletten. Their suggestions on this work were extremely helpful and ended up strengthening my dissertation. Discussions and group meetings with Ben were always a joy to attend. Collaborations with Danny have really opened several avenues in my research and also turned out to be incredibly valuable in Chapter 4 of this dissertation. Ellen was very gracious in letting me to use her lab when we did not have our own lab space, for which I am so grateful. It really allowed me to get a head start on some of my projects. Collaborations with her lab and her advice on Chapters 3-5 in this dissertation tremendously valuable. She has always been an inspiration. I also want to express my gratitude to my undergraduate advisor Dr. Abhijit

Patra, who has been a longtime mentor to me. He really shaped my thinking and approach to science as a young researcher.

I was lucky to be surrounded by amazing colleagues in the Chem & Biochem department. I got to learn so much about different research areas, even outside of my field which has really helped expand the boundaries my scientific knowledge. Bill Gelbart, Ben Schwartz, and Sarah Tolbert, were all very supportive and helped me navigate the difficulties of the grad program during my first year. Also, a huge thanks to the Grad Office staff – Justyna, Nick, Annie and Stephanie. I want to give a shout out to the very helpful staff members at UCLA Chemistry & Biochemistry – Janette, Nati, Ricky, Jose and others, whose efforts keep our labs running smoothly.

A huge thank you to all the members of the Caram Lab, for being such an amazing and caring bunch who have all grown to be valued friends. Timothy Atallah, has been nothing short of a second mentor. I really appreciate all debates and critical discussions I had with Tim, which have made me grow as a scientist. Tim's willingness to help others is really inspiring. I have learnt so much from Hannah Friedman, about science and otherwise. I am thankful to have had both Tim and Hannah as companions during the set up phase of the lab. Most of the early days were spent with all three of us discussing our plans for building a new set up or assembling new equipment in the lab. Austin, Leandra, Niklas, and Jill were the grad students involved in aggregates related projects and I am grateful their contributions. Niklas took extensive temperature dependent absorption and emission for Chapter 4, Leandra did aggregate screenings in Chapter 3 and some NMR characterizations. Austin did NMR characterizations in Chapter 3 as well as synthesis and spectroscopic characterizations in Chapter 5. Austin's extensive work with tubular aggregates was extremely relevant in Chapter 5. All of this work has contributed in some way to improve our

understanding of this complicated topic. I am so glad to have Jill and Ash, who are going carry some of these projects forward. Anthony, Stephanie, and Ashley have also been great lab mates and friends, always willing to help each other out in times of need. I have made so many memories in the lab, all of which will be cherished for a very long time. Grad school would have been a very sad place without all of you.

I have had the opportunity to mentor really talented undergraduates and high school students over the years. I am grateful for all of their contributions to this dissertation. Danielle Koppel, did the modeling for Chapter 2 in this work. Daniel Cadena, worked on photochemical reactions involving tubular aggregates. Xingyu Shen, did some photobleaching and screening studies (Chapter 3) with 2D aggregates. Ray Huang developed aggregate melting experiments and their modeling, and helped in image analysis of tubular aggregates (Chapter 6). High school volunteer Everett Tolbert-Schwartz fitted large data sets from kinetic lifetime studies of aggregates (Chapter 6). It was very rewarding to see them start with little research experience and grow into independent researchers who could design and troubleshoot their own experiments.

I want to thank our collaborators whose work and expertise were instrumental for this dissertation. Chern Chuang's theory nicely complements the work in Chapter 1 and together, they form the basis for Chapter 4. I am really thankful for several discussions with Chern that helped me understand the complicated theory and for his contributions to Chapters 4 and 5. Weili Zheng and Ed Egelman's expertise on cryoEM reconstruction techniques really made Chapter 5 materialize. Discussions with Ed were always enlightening and offered different perspectives. Nadine Bradbury (Neuhauser lab) did all the modeling work and Monica Pengshung (Sletten lab) took quantum yield measurements for Chapter 4.

I cannot go without mentioning my family – mom, dad, dada and vahini, who have always stood by me in all of my crazy decisions and who go out of their way to ensure my well-being. Their incessant love and support is what keeps me going. I want to thank Sri Mohan Thute, whose directions and support along every step of way have been a guiding light. Finally, I wouldn't have survived a single day here if it weren't for Sudhanshu, my fiancé and best friend. Whether I needed an ear to vent my frustrations or an affirming voice to pull me up, he was always there for me. None of this would amount to anything if I do not get to share it with all of you.

This work was supported by NSF CHE grant no. 1905242 and Faculty Research Grant (UCLA Academic Senate). I am thankful for several fellowships received during my time here: Graduate Division Dissertation Year Fellowship as well as several departmental fellowships - Excellence in Second Year Research and Academics Award, Excellence in Research Fellowship, SG Fellowship and travel grants such as UCLA Research Showcase Fellowship. I am grateful for the Thomas L. and Ruth F. Jacobs dissertation award. Also, thanks to instrumentation facilities at UCLA that allowed me to carry out several characterizations: Materials Instrumental Center and the Biochemistry DOE Facility in the Dept. of Chemistry and Biochemistry, Electron Imaging Center for Nanomachines and Nano- and Pico Characterization Lab at California NanoSystems Institute, UCLA.

Chapters 1 and 6 contain parts from an unpublished perspective by Arundhati Deshmukh.

Chapter 2 is adopted from the published paper, "Deshmukh, A. P.; Koppel, D.; Chaung, C.; Cadena, D.; Cao, J.; Caram, J. R. Design Principles for 2-Dimensional Molecular Aggregates using Kasha's Model: Tunable Photophysics in Near and Shortwave Infrared. *J. Phys. Chem. C* **2019**,

123 (30), 18702-18710." Experiments: APD and DC; modeling: DK and CC; writing: APD, DK, CC; editing: all authors; advising: JRC.

Chapter 3 is adopted from the published paper, "Deshmukh, A. P.; Bailey, A. D.; Forte, L. S.; Shen, X.; Geue, N.; Sletten, E. M.; Caram, J. R. Thermodynamic Control over Molecular Aggregate Assembly Enables Tunable Excitonic Properties Across the Visible and Near-Infrared. *J. Phys. Chem. Lett.* **2020**, *11* (19), 8026-8033." Experiments and data analysis: APD, ADB, LSF, NG, XS; modeling: APD; writing: APD; editing: all authors; advising: EMS, JRC.

Chapter 4 is adopted from the unpublished manuscript, "Deshmukh, A. P.; Geue, N.; Bradbury, N. C.; Atallah, T. L.; Pengshung, M.; Chuang, C.; Cao, J.; Daniel Neuhauser, D.; Sletten, E. M.; Caram, J. R. Temperature dependent spectroscopy reveals excitonic band structure of 2-dimensional molecular aggregates. *In preparation*." Experiments and data analysis: APD, NG, TLA, MP; modeling: NB, CC; writing: APD, NB, CC; editing: all authors; advising: DN, EMS, JRC.

Chapter 5 is adopted from the unpublished manuscript, "Zheng, W.;[†] Deshmukh, A. P.;[†] Chuang, C.; Bailey, A. D.; Egelman, E. H.; Caram, J. R. High-resolution cryoEM structure of self-assembled supramolecular helical light harvesting nanotubes. *In preparation*. [†]Co-first authors." Experiments: WZ, APD, ADB; modeling: CC; writing: APD, WZ, CC; editing: all authors; advising: EHE, JRC.

Chapter 6 contains preliminary results from studies yet to be published. Aggregate melting studies experimental set up and modeling: Ray Huang. In-situ time resolved photoluminescence experiments and data processing: Timothy Atallah and Arundhati Deshmukh, data fitting: Everett Tolbert-Schwartz.

BIOGRAPHICAL SKETCH

Education

2016 **B.S - M.S.** in **Chemistry** (major), **Earth and Environmental Sciences** (minor), Indian Institute of Science Education & Research, Bhopal (IISERB)

Publications (Selected)

5. Zheng, W.;† **Deshmukh, A. P.**;† Chuang, C.; Bailey, A. D.; Egelman, E. H.; Caram, J. R. High-resolution cryoEM structure of self-assembled supramolecular helical light harvesting nanotubes. *In preparation*. †Co-first authors.

4. **Deshmukh, A. P.**; Geue, N.; Bradbury, N. C.; Atallah, T. L.; Pengshung, M.; Chuang, C.; Cao, J.; Neuhauser, D.; Sletten, E. M.; Caram, J. R. Temperature dependent spectroscopy reveals excitonic band structure of 2-dimensional molecular aggregates. *In preparation.*

3. **Deshmukh, A. P.**; Bailey, A. D.; Forte, L. S.; Shen, X.; Geue, N.; Sletten, E. M.; Caram, J. R. Thermodynamic Control over Molecular Aggregate Assembly Enables Tunable Excitonic Properties Across the Visible and Near-Infrared. *J. Phys. Chem. Lett.* **2020**, *11* (19), 8026-8033.

2. **Deshmukh, A. P.**; Koppel, D.; Chaung, C.; Cadena, D.; Cao, J.; Caram, J. R. Design Principles for 2-Dimensional Molecular Aggregates using Kasha's Model: Tunable Photophysics in Near and Shortwave Infrared. *J. Phys. Chem. C* **2019**, *123* (30), 18702-18710.

1. **Deshmukh, A**.; Bandyopadhyay, S.; James, A.; Patra, A. Trace level detection of nitroanilines by amplified fluorescence quenching of a solution processable porous organic polymer. *J. Mater. Chem. C* **2016**, *4*, 4424-4433.

Presentations

2021 ACS Fall National Meeting, Atlanta (Oral)

2021 University of California Chemical Symposium (Oral)

2020 Materials Research Society Virtual Spring/Fall Meeting (Oral)

2019 ACS National Meeting, San Diego (Oral)

2019 Photochemistry Gordon Research Conference, Stonehill College, MA (Poster)

2019 Pacific Conference on Spectroscopy and Dynamics, San Diego (Poster)

2018 & 2019 Seaborg Symposium, UCLA (Posters)

Awards and Honors

2021 *Thomas L. and Ruth F. Jacobs* Dissertation Award

2020-21 UCLA Graduate Division *Dissertation Year Fellowship*

2020 UCLA Chem & Biochem *Excellence in Research Fellowship* and *SG Fellowship*

2019 Excellence in Second Year Academics and Research Award

2018 *Link Energy Fellowship*, Honorary mention

2014 *Indian Academy of Sciences* - Summer research fellowship

2012 *CNR Rao* Award for excellence in academic performance

Service

2021 *Reviewer*, J. Phys. Chem. Lett. & J. Mater. Chem. A

2020 *Member*, Graduate Admissions and Recruitment Committee at UCLA Chem & Biochem

2019-20 *President & co-founder*, Joint Research Safety Initiative at UCLA

2018-20 *Panelist* at Annual Teaching Assistants Conference at UCLA

2018-20 *Mentor*, Nanovation Competition organized by CNSI at UCLA

2018-20 *Volunteer*, Teacher training workshops and demos, CNSI Outreach program at UCLA

2017-19 *Booth leader*, Exploring Your Universe, UCLA

Chapter 1

Introduction to Excitonic Molecular Aggregates

1.1 Chromophore molecular aggregates

Molecular aggregates are non-covalent assemblies of chromophores that exhibit very distinct photophysical properties compared to their monomer counterparts. π-conjugated planar molecules stack on each other in specific geometries, facilitated by an interplay of sterics, solubility, and π–π interactions. Several examples of molecular aggregates are known in the literature among various classes of materials - (i) photosynthetic antenna complexes (Fenna-Mathews-Olson complex in green sulfur bacteria, LH2 complex in purple bacteria),[1–5] (ii) melanin-based biological pigments,[6] (iii) conjugated polymers, e.g. polydiacetylenes, poly(3-hexylthiophenes),[7–10] (iv) a host of small organic molecules like porphyrins, perylene bisimides, cyanines, pseudoisocyanines, squaraines, boron-dipyrromethene (BODIPY) derivatives,[1,11–17] and (v) more recently, in microwave metamaterials.[18]

1.2 Kasha's model of H- and J-aggregates

Kasha's seminal work from 1950s provides simple relations between molecular arrangement and photophysical properties in dimers and linear aggregates and has been successfully implemented in several types of chromophore systems mentioned above (Figure 1.1).[19,20] In this model, we treat molecules as bricks with a transition dipole moment (TDM) pointing along its length. Absorption of a photon by a molecule creates an exciton represented by the oscillating TDM. In molecular aggregates, these TDMs undergo dipole-dipole coupling over long distances

(upto micron scale). When the molecules are arranged cofacially (Figure 1.1), the lowest energy configuration will have a net zero TDM (all dipoles cancelling out) while the highest energy configuration (all dipoles in-phase, $k = 0$) will have a non-zero TDM. Fermi's golden rule says that the probability of an optical transition is directly proportional to the transition dipole moment operator ($\hat{\mu}$) squared.

$$\frac{dP_{ab}}{dt} = \frac{2\pi}{\hbar}|\langle\psi_a|\hat{\mu}|\psi_b\rangle|^2\rho(E) \tag{1.1}$$

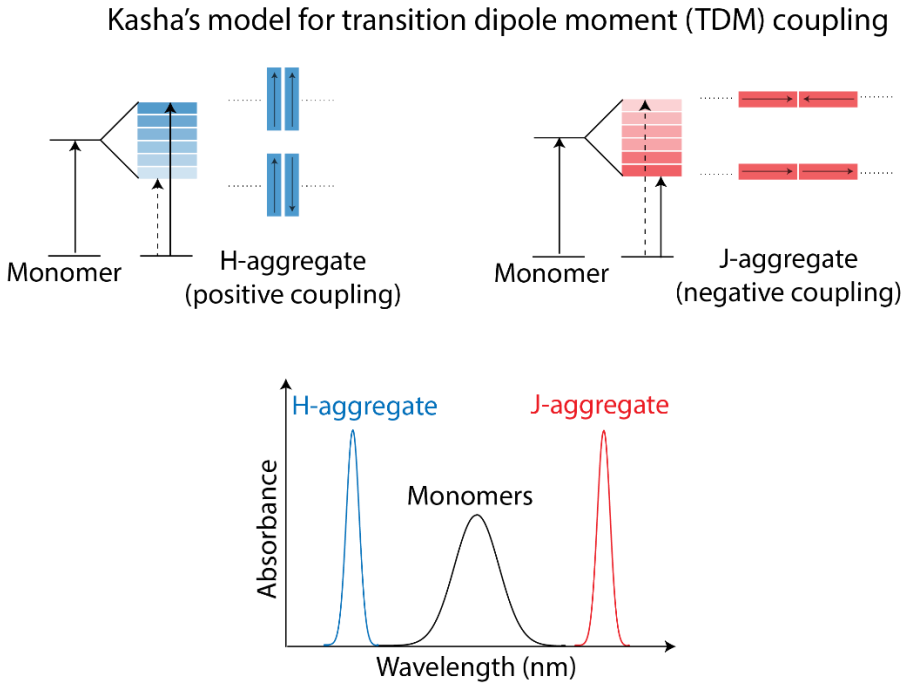

Figure 1.1 Kasha's model for 1D transition dipole moment coupling: H- and J-aggregates Schematic representing transition dipole coupling in H-aggregates with co-facial linear arrangements (top left), J-aggregates with head-to-tail linear arrangements (top right), and spectral shifts corresponding to each arrangement.

Therefore, based on Fermi's golden rule, the lowest energy state will be optically dark while the higher energy one will have an allowed optical transition (called *bright state*). As a result, we observe a blue shift in the optical spectra of the aggregate compared to the monomer. Conversely,

when the molecules are arranged in a head-to-tail fashion, the lowest energy configuration has a net non-zero TDM and therefore, we observe a red shift in the optical spectra. The blue shifted or cofacial aggregates are called H-aggregates where 'H' stands for 'hypsochromic' whereas the red shifted or head-to-tail ones are called as J-aggregates named after the scientist Jelley, who first observed this phenomenon in 1936.[21] J-aggregates are also, sometimes called as Scheibe aggregates, as Scheibe also observed this effect independently in 1937.[11,22,23] Due to the dipole-dipole coupling, extended H- and J-aggregates have characteristic spectral signatures with extremely narrow linewidths (~ hundreds of wavenumbers) and hundreds to thousands of wavenumbers of red or blue shifted absorption and emission compared to the monomers. In some cases, the ratio of the vibronic peaks in the spectra changes upon aggregation.[1,24] For example, in H-aggregates the 0-1/0-0 vibronic peak ratio is enhanced compared to monomers while J-aggregates have higher 0-0/0-1 peak ratio.[1]

1.3 Frenkel exciton model

In extended aggregate systems with large number (> 10^2) of monomers, several TDMs constructively add up over long ranges, i.e. they undergo non-nearest neighbor coupling resulting in huge enhancements of the net aggregate TDM. This long range coupling of chromophore TDMs has huge ramifications towards their excitonic properties. The long range coupling of TDMs leads to strong coupling that can allow for delocalized excitons to persist despite the high disorder that is present in solvated forms at room temperature.[25] Such couplings and the resulting excitonic properties can be calculated using the Frenkel exciton Hamiltonian (Figure 1.2), which consists of monomer energies (ϵ_n) on the diagonal terms and couplings between individual monomer sites (J_{nm}) on the off diagonal terms,[20,26]

$$H_s = \sum_n \epsilon_n |n\rangle\langle n| + \sum_{n \neq m} J_{\mathrm{nm}} |n\rangle\langle m| \quad (1.2)$$

Throughout this work, we may discuss the zero disorder case or the diagonal disorder case. All ϵ_n are to a same value (which can be scaled to zero) for the no disorder case or span a Gaussian distribution of energies for diagonal disorder case. Diagonalizing this Hamiltonian allows us to find its eigenstates and eigenvalues (Figure 1.2).

$$H_s = \sum_k E_k |k\rangle\langle k| \quad (1.2)$$

where $|k\rangle$ is the k^{th} eigenstate with energy E_k. Eigenstates of the Frenkel exciton Hamiltonian form the exciton basis with a redistributed oscillator strength. The bright state (with all the dipoles oscillating in-phase) can be found using Fermi's golden rule from eq. (1.1). In some cases, instead of the Frenkel exciton model, the essential state model has been applied to account for ground state charge transfer interactions in addition to excitonic coupling.[27,28]

Frenkel exciton model with the dipole treatment for the coupling terms was first used by Kuhn and co-workers where the couplings between individual monomers were determined by dipole-dipole coupling relations.[29–31] A noteworthy point is that these terms extend over the entire Hamiltonian, and not just the first off-diagonal (which would only correspond to nearest-neighbor coupling). In other words, the matrix is not tridiagonal.

The total number of states is conserved i.e. the total number of excitonic states are the same as the number of interacting monomeric states. In the large N limit, this effectively leads to an excitonic band with a density of states (DOS) out of which, the optically bright state can be determined using Fermi's golden rule. It should be noted that these 'dark' excitonic states are always present irrespective of H- or J-aggregation. The geometric arrangements in H- or J-aggregates only influence which of these states will be optically active. The optically active state

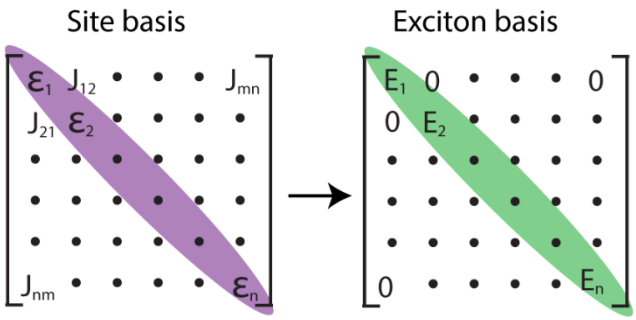

Figure 1.2 Schematic representation of a Frenkel exciton Hamiltonian with non-nearest neighbor coupling.

Left: Frenkel exciton Hamiltonian with site energies on the diagonal (ϵ_n) and respective inter-site couplings (J_{nm}) on all off-diagonal terms. Diagonalization provides the excitonic states and their energies.

corresponds to the highest or the lowest energy state in linear H- or J-aggregates, respectively. In other words, the optically active state is always at the band edge in 1D systems. Later on (Chapters 2 and 4), we will show that this condition is not always true in higher dimensional aggregates with significant implications towards the photophysical properties.

1.4 Other consequences of long range coupling

Another direct consequence of the delocalized excitons is *motional narrowing* or exchange narrowing.[32–34] This phenomenon explains the extremely narrow linewidths of these aggregates that persist even at room temperature in solution phase. As the excitons delocalize over several monomeric sites with slightly different energies, the fluctuations get averaged out following a Poisson distribution where $\Gamma_{inhom} \propto \frac{1}{\sqrt{N}}$ (width of the distribution is inversely proportional to the square root of the number of samples). Exciton localization and finite size of the aggregates has often been explore as a line broadening mechanism.[35–37] In the strong coupling regime (to which

the cyanine dyes aggregates belong), this leads to the distinctly narrow lineshapes of the extended aggregate systems.

The bright state in such systems is comprised of a large number to TDMs oscillating coherently with each other. This leads to cooperative effects in the emission of the aggregates where the radiative rates are non-linearly enhanced compared to the monomeric counterparts. This phenomenon is called superradiance (η_{SR}) and is usually quantified as the ratio of radiative rate of aggregate to the monomer.[38–42]

$$\eta_{SR} = \frac{k_r^{agg}}{k_r^{mon}} \tag{1.3}$$

The radiative rate itself has a fundamental dependence on the energy gap due to the energy gap law.[43,44] As a result, comparing the radiative rates across the drastically different energy gaps of monomers and aggregates is not accurate. We, therefore, correct these for the energy gap as -

$$\eta_{SR} = \frac{k_r^{agg}/E_g^{agg}}{k_r^{mon}/E_g^{mon}} \tag{1.4}$$

Due to such enhanced radiative rates, excitonic aggregates are able to undergo very fast excited state energy or charge transfer with surrounding moieties. One example of this is the enhanced coupling with quantum dots enabling fast picosecond FRET.[45–47] This is also one of the reasons for a huge interest in aggregates as photosensitizers for silver halide photographic plates prior to commercialization of digital photography.[48] There is a vast literature studying photosensitization, adsorption and aggregation of dye molecules on silver halide surfaces summarized in a review by Herz.[49]

1.5 Applications of excitonic aggregates

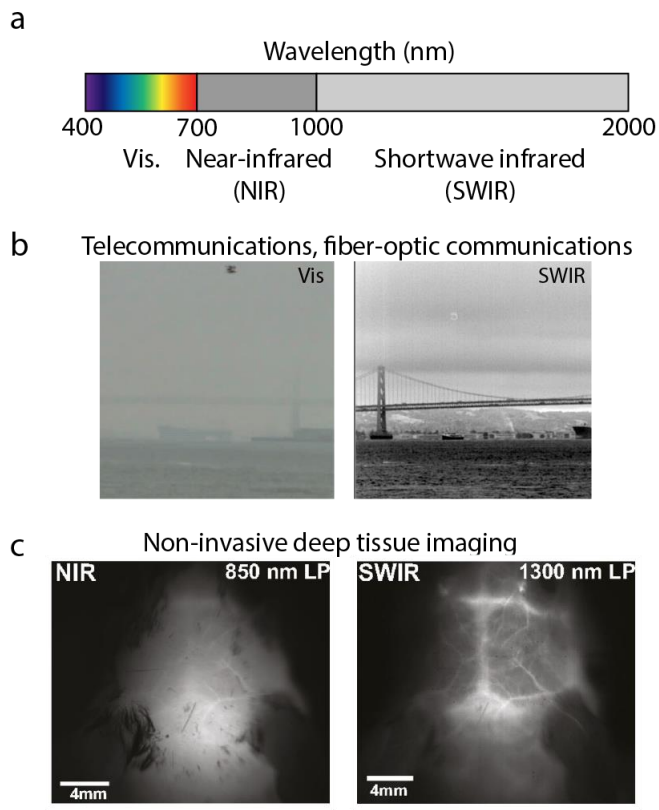

Figure 1.3 Advantages of shortwave infrared region of the electromagnetic spectrum
a. Depiction of the visible, near-infrared (NIR) and shortwave infrared (SWIR) regions of the electromagnetic spectrum, b. An image showing the higher penetration of SWIR light through atmosphere (adopted from Sensors Unlimited[63]) and c. Non-invasive image of a mouse skull in NIR (left) and SWIR (right) showing brain vasculature (adopted from Carr et al., 2018[64]).

The aforementioned properties, directly imparted by the long range TDM coupling, are extremely relevant to several new technological and biological applications. The excitonic states with strong TDMs can be coupled to cavity mode or a plasmon mode, leading to hybrid states.[50–57] This has led to the new areas of research in polaritonics and plexcitonics. As mentioned before, these systems can also act as efficient energy transfer donors, acceptors or even as relay bridges between another donor and acceptor.[46,47,58,59] Due to their narrow emission linewidths, energy

transfer with quantum dots as donors can be used to convert a broadband excitation into a narrow emission.[46] Excitonic aggregates also be applied in several optoelectronic devices such as luminescent solar concentrators, organic light-emitting diodes, and solar cells.[60–62]

Our interest in these systems arises from the fact that aggregation can afford a very high degree of spectral tunability, enabling spectral shifts beyond the visible region (400-700 nm) into near-infrared (700-100 nm) and shortwave infrared (1000-2000 nm), abbreviated as NIR and SWIR respectively (Figure 1.3a).[65] Due to reduced Rayleigh scattering ($\propto 1/\lambda^4$), SWIR wavelengths are able to transmit up to longer distances through atmospheric fog, smoke or even, animal tissue as demonstrated in Figure 1.3b-c. SWIR is particularly useful for telecommunications and fiber-optic communication where the fast radiative rates of aggregates can enable rapid transmission of information.[66] In biology, SWIR imaging is a powerful tool that can enable non-invasive therapies and surgeries with minimal background autofluorescence, resulting in high contrast images (Figure 1.3c).[64,67,68] Because of the concentration of the total oscillator strength in a narrow spectral lineshape, aggregates have high molar absorptivities that may enable higher quantum efficiencies required for biological imaging, the narrow emission lines can enable multicolor imaging with minimal crosstalk.[67,69,70] Rare earth metals, quantum dots and nanoplatelets are some examples of inorganic SWIR emitting materials.[71–73] Other than polymethine dyes, BODIPY derivatives, and single-walled carbon nanotubes, there are few examples of organic species with strong SWIR absorption and emission.[70,74,75] Aggregation can therefore be a new avenue for tuning the optical properties of organic materials into SWIR.

1.6 Importance of the supramolecular structure

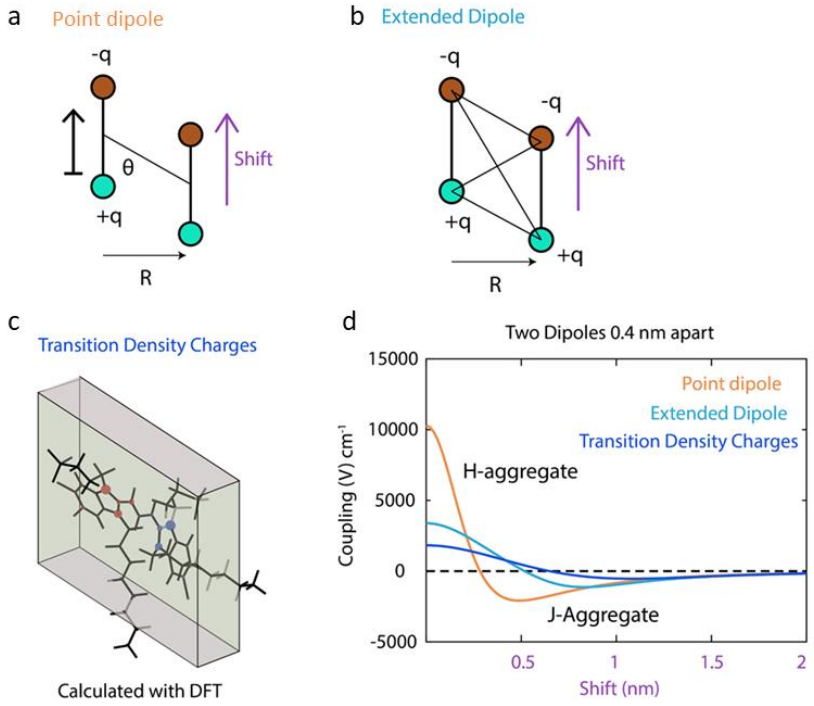

Figure 1.4. Slip dependence of coupling for point dipole, extended dipole, and transition density charges models

a-b. Schematic representations of two dipole couplings for a. point dipole model, b. extended dipole model, c. A representative transition density charges model, and d. Coupling curves for a dimer with all three models showing that the point dipole model really overestimates the coupling at smaller slip values. Calculation by Chern Chuang.

Kasha's cofacial and head-to-tail aggregates describe two limiting possibilities. In most systems, molecules can stack in any possible geometry between these two cases. We take two molecules next to each other and calculate their dipole-dipole coupling as we *slip* them relative to each other as shown in Figure 1.4. We obtain a continuous variation of the coupling with respect to slip. This shows that the ultimate excitonic properties will be highly sensitive to the supramolecular arrangement of the molecules with the aggregate. Further, the couplings also

depend on the choice of coupling model (only considering dipolar couplings). The simplistic point dipole model shows a steeper dependence on slip with overestimated positive couplings. Transition density charges form a more accurate description where couplings are calculated from partial charges assigned to each atom (obtained from quantum chemical calculations). In the transition density charge model, the magnitudes of both positive and negative couplings are smaller and the zero-crossing point is at a higher slip.

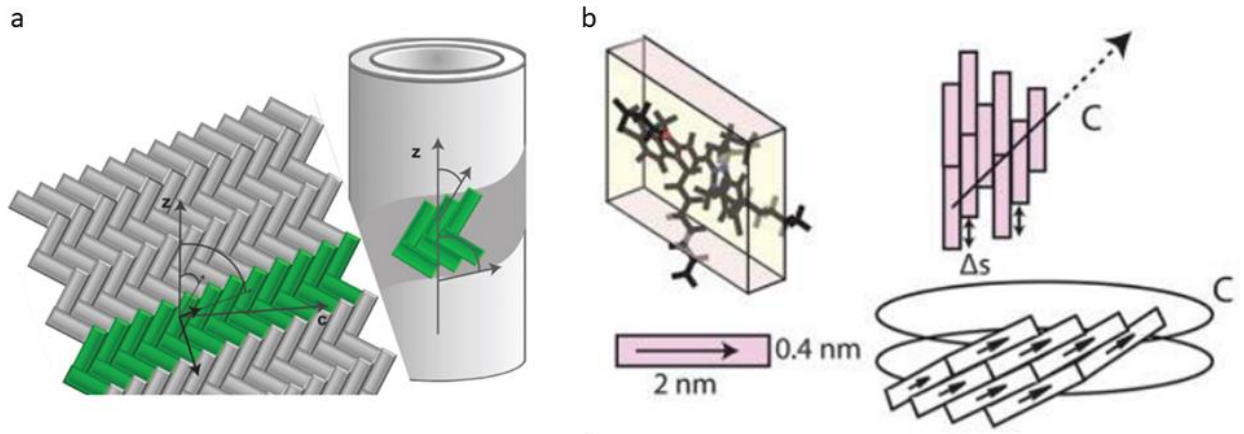

Figure 1.5. Schematics of herringbone arrangement and brick layer arrangement
a. A herringbone style tiled layer rolled into a cylindrical geometry (adopted from Eisele et al., 2012[77]), and b. Brick layer model showing the direction of the chiral vector (adopted from Doria et al., 2018[79]). Both the models have reproduced experimental spectra of a double-walled nanotube aggregate.

Here, we only consider arrangements with one molecule per unit cell, called as the brick layer arrangement.[31,76] However, situations with two or more molecules per unit cell are also possible leading to symmetry breaking (Figure 1.5). For example, the herringbone model has also been used to describe both 2D as well as tubular aggregates.[77,78] Nevertheless, the dependence of couplings on molecular arrangement shows the importance of supramolecular packing in these systems. Particularly, given well defined relationships between the supramolecular structure and

excitonic properties, we may use aggregation as a new avenue to tune and avail new photophysical behaviors that are not conventionally accessible.

1.7 Aggregate morphology

Another way one can manipulate the TDM couplings is via different topologies. Instead of TDMs interacting within a linear chain, they can be arranged in a 2-dimensional brick layer pattern as in case of sheet-like aggregates or the sheets can be rolled up with a specific chiral vector, forming tubular aggregates. Several experimental examples of 2D aggregates as well as tubular morphologies such as double-walled nanotubes and bundles exist in the literature. However, the effect of different morphologies on the excitonic band structure and the photophysical properties is not well explored.

1.8 Types of disorder in aggregates

In addition, other aspects of the aggregates also need to be considered. Exciton transport within these systems and ultimately their lineshapes, and excitonic energy transfer properties are highly dependent on the degree of various disorders.[80–83] Disorder may arise in these extended chromophore systems from structural and energetic fluctuations. Each aggregate may have a distribution of monomeric energies within a single sheet or tube, as well as, the distributions arising from an ensemble of multiple aggregates. Single aggregate disorder may arise from several structural factors such as folds or other defects in these periodic systems. All the above line broadening mechanisms fall under the umbrella of inhomogeneous (or static) disorder. Furthermore, since many of these systems are in solvated form at room temperature, exciton-phonon couplings (i.e. coupling of the excitons to vibrational modes) and solvent bath interactions also contribute to the disorder, this type of broadening mechanism falls under homogeneous (or

dynamic) disorder. All of these factors lead to fluctuations in the nanoscale TDM couplings, thereby affecting the excitonic properties. In some cases, exciton self-trapping models have been proposed to explain temperature dependent emission properties.[84,85]

This dissertation aims at manipulating the TDM couplings in supramolecular aggregates via chemical control of supramolecular packing within the aggregates and aggregate topologies. The overall goal of this work is to use aggregation as platform to explore new photophysical functionalities, for example, red shifted J-aggregates in SWIR.

1.9 Cyanine dyes

We focus on the aggregates of cyanine dyes. Cyanines are a large family of chromophores with the general structure shown in Figure 1.6a where two aromatic heterocycles are connected by a polymethine bridge. Cyanine dyes form a large structural data set with modifications on the length of the bridge allowing for spectral tunability and various substitutions to the heterocycles enabling control over their solubilities and sterics.[12] Common heterocycles in cyanine dyes are benzothiazole, benzimidazole and benzoindole. A crucial aspect of the structure is the positive charge on the heteroatom that is delocalized over the entire cyanine bridge, also known as the 'cyanine form.'[86] In dyes with longer chains, this charge tends to localize, forming the 'dipole form' or 'bis-dipole form' with the resulting absorption spectra showing a broadened flat lineshape (Figure 1.6b).[87] The cyanine form does not show bond length alternation (confirmed through their crystal structure), and is crucial for the ground and excited state wave function overlaps, enabling high oscillator strengths. In fact, cyanine dyes are known to span the broadest range of the spectrum

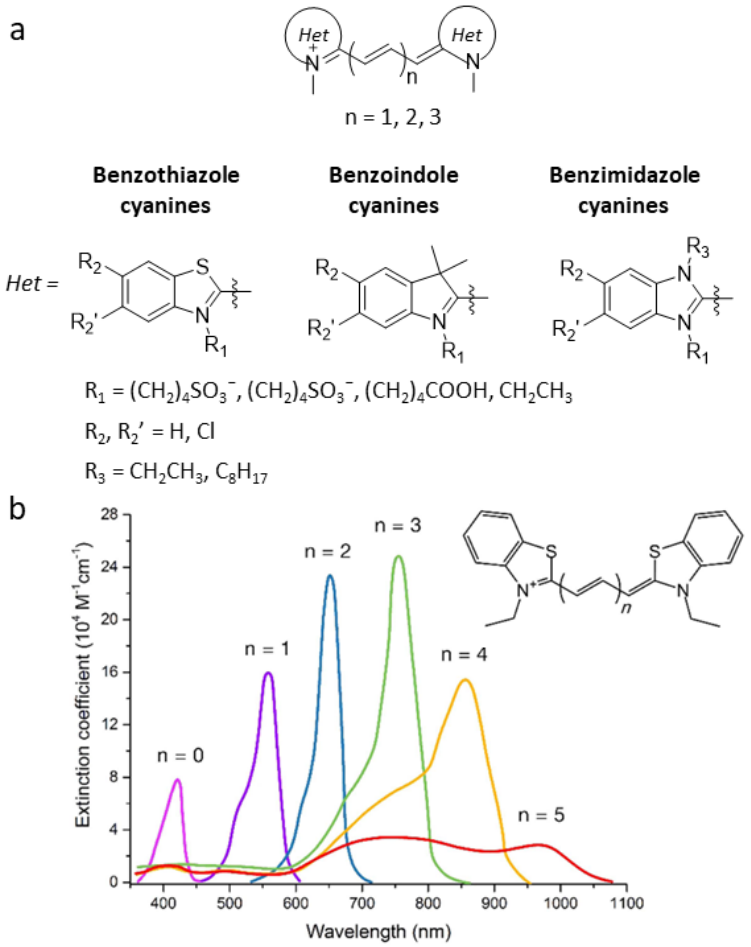

Figure 1.6. Cyanine dyes – general structure and absorption spectra

a. General structure of cyanine dyes with two aromatic heterocycles connected via a polymethine bridge; common heterocycles are also shown; b. Absorption spectra of a cyanine dye (structure in inset) as a function of increasing bridge length showing broadened peaks at higher lengths. Part b is adopted from Bricks et al., 2018[12].

with increasing bridge length.[12] As shown in Figure 1.6b, addition of just one double bond enables a shift of ~100 nm. Cyanine dyes are also known to readily aggregate into several different morphologies such as double-walled nanotubes, bundles and sheets.[17,88–92]

1.10 Relations to other materials

Besides molecular aggregates, several materials show excitonic properties in the aggregated state. However, there are some subtleties that need to be considered before making such comparisons. Therefore, it is useful to clarify where do the excitonic transitions in the molecular aggregates lie with respect to extended solids or other molecular systems.

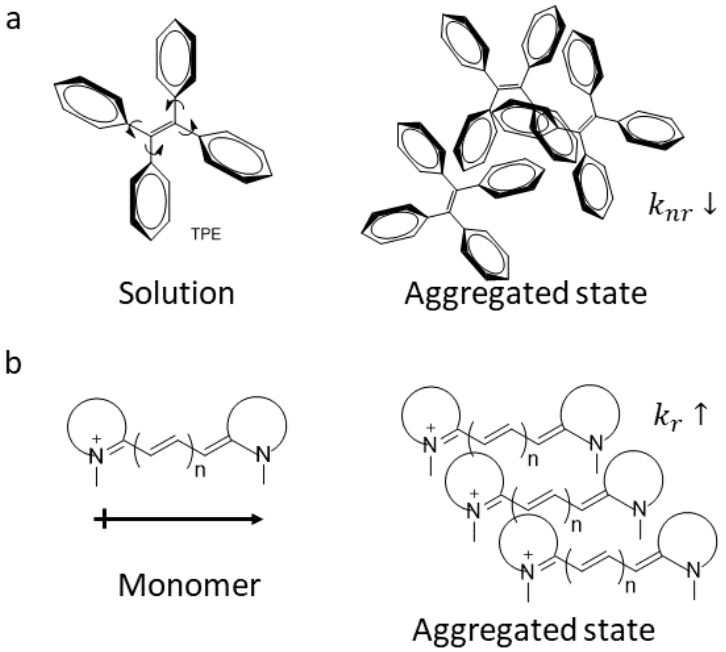

Figure 1.7 Comparison of aggregation-induced emission (AIE) with excitonically coupled aggregates

a. Schematic depicting the mechanism of AIE - restriction of intramolecular motions upon aggregation in tetraphenyl ethylene, b. excitonically coupled aggregates where ordered arrangements of chromophores enable transition dipole coupling.

Extended inorganic solids such as bulk semiconductors have strong electronic coupling but only in the nearest-neighbor range (tight-binding model) and the conduction and valence bands are formed through wavefunction overlap.[93] The excitons in these systems are usually weakly bound

due to higher dielectrics with binding energies in ~1-10 meV range and the disorder is very low. The delocalized excitons in bulk semiconductors can be confined, as in case of quantum dots and nanocrystals, which increases the binding energies to 10-100s of meV. A key point is that inter-nanocrystal couplings are still very weak.

Free molecules in solutions present the other extreme from bulk semiconductors, where the excitations are completely described by the molecular HOMO and LUMO overlaps. In molecular aggregates, the molecular excitons undergo dipole-dipole coupling, which follows $\propto R^{-3}$ dependence, and hence extends in the long range beyond just first or second nearest-neighbors. The exciton wavefunctions spread over multiple sites, forming a delocalized Frenkel excitons. Though, there is still a significant amount of disorder from vibronic couplings, solvation etc. Molecular aggregates, therefore present an intermediate regime that can bridge the bulk semiconductor and molecular properties. A similar exceptional case was recently reported in perovskite superlattices where the confined excitons within nanocrystals were coupled, resulting in collective emission phenomena similar to H- or J-aggregates.[94]

Another extensive research area where aggregation plays a role in photophysical properties is aggregation-induced emission (AIE).[95] A key distinction between AIE active materials and molecular aggregates is that the solid state emission in AIE comes from suppression of non-radiative decay rates and there is no long-range inter-chromophore TDM coupling. The core idea of AIE is based on blocking the non-radiative decay pathways by restriction of intramolecular rotations. Non-planar moieties such as tetraphenylethylene (Figure 1.7) do not allow the formation of close packed structures in the aggregated state and the steric hindrance suppresses intramolecular rotations. In contrast, π–π stacking plays a key role in forming the highly ordered

structures that enable long range TDM coupling in excitonic molecular aggregates. The long-range TDM coupling enhances the radiative rates (as opposed to suppressing non-radiative rates), which lead to the characteristic excitonic properties of aggregates. Therefore, AIE active molecules should not be classified as excitonic aggregates and vice versa.

Chapter 2

Extending Kasha's Model to Two-Dimensional Aggregates

Aggregation can be used as a platform to access new photophysical behaviors such as strong absorptions and emissions in SWIR. In this chapter, we discuss two examples of sheet-like aggregates with strong SWIR absorptions but low emissions. We use the Frenkel exciton model for 2D aggregates to find the cause of such photophysical behaviors, introducing the concept of I-aggregate, a new type of aggregate that shows mixed characteristics of H- and J-aggregates.

2.1 Significance of shortwave infrared materials

Near-infrared (NIR, 700 - 1000 nm) and shortwave infrared (SWIR, 1000 - 2000 nm) photoactive materials are highly sought out due to their superior performance in many applications, ranging from deep-tissue imaging,[96] to telecommunications,[97] and LIDAR.[66] Light in the NIR and SWIR transmits over longer distances in the atmosphere and shows less loss for fiber-optic communication due to decreased scatter and absorption in this spectral regime.[97] In biomedical contexts, significantly decreased auto-fluorescence from biomolecules in the SWIR promotes better signal-to-noise ratio in fluorescence imaging.[64,98,99]

However, there are few molecular species (such as carbon nanotubes, lanthanide complexes and flavylium polymethine dyes), which absorb efficiently beyond 1000 nm.[74,98] Approaches for designing strong absorbers and emitters in NIR and SWIR are primarily based on covalent modification of conjugated dyes and semiconductor nanocrystal materials.[47,74,100,101] These materials cannot necessarily offer high molar absorptivities and narrow linewidths, prerequisites for several technological applications such as nonlinear optics and photonics.[102,103] However, another approach to achieving strong SWIR absorption is through coupling of multiple molecular transition dipole moments (TDMs, μ) into extended excitonic states. The oscillator strength and radiative rate of a molecule are proportional to the square of the TDM ($\mu^2 = |\langle g|\Sigma_i q_i r_i|e\rangle|^2$, where g and e represent the ground and excited state wavefunctions, q_i and r_i are the charges and their positions).[104] In molecular aggregates, certain excitonic transitions are enhanced by a nonlinear increase in the oscillator strength due to long-range coherent coupling among TDMs.[1] Molecular aggregates therefore can show increased absorption over a narrow wavelength range, enhanced emission due to faster radiative rates, and long-range coherent energy transport.[1,12,79,105]

We define molecular aggregates as non-covalently bound molecular assemblies formed via entropic and Van-der-Waals driving forces.[1] Molecules within an aggregate undergo coherent TDM coupling, and electronic excitations extend over many molecules to form delocalized Frenkel excitons.[93] The net excitonic TDM depends on the phase relationship of individual TDMs, their coupling- both defined by the geometric arrangement of dipoles- and the energetic disorder among the chromophores.[1] Kasha developed a simple formalism describing how aggregation leads to absorption shifts for molecular dimers and linear chain aggregates as shown in Figure 2.1a.[19] When dipoles are aligned in a head-to-tail fashion, the optically active bright state (with non-zero TDM) is also the lowest energy exciton. As a result, these arrangements give rise to a red shift in the

absorption spectrum. On the other hand, cofacial dye organization renders the highest energy exciton as the only optically active state resulting in a blue shift in the absorption spectrum. The blue-shifted aggregates are called H-aggregates whereas the red-shifted aggregates are called J-aggregates.[1,21] One can shift between H- and J-aggregation by changing the slip (or angle) between each dye monomer, and many groups have employed this approach to generate H- or J-aggregated structures.[12,106] While the formalism for dimers and linear chains is well-known,[1,19,107] complications arise in the case of 2-dimensional (2D) or quasi-2D sheet and tubular aggregates.[108] Along one axis, the predominant coupling will be negative (J-like) while coupling along the other axis could be positive (H-like). This is depicted as a cartoon in Figure 2.1b, where the coupling of the central brick (white) with its neighbors depends on the distance and the slip from the central.

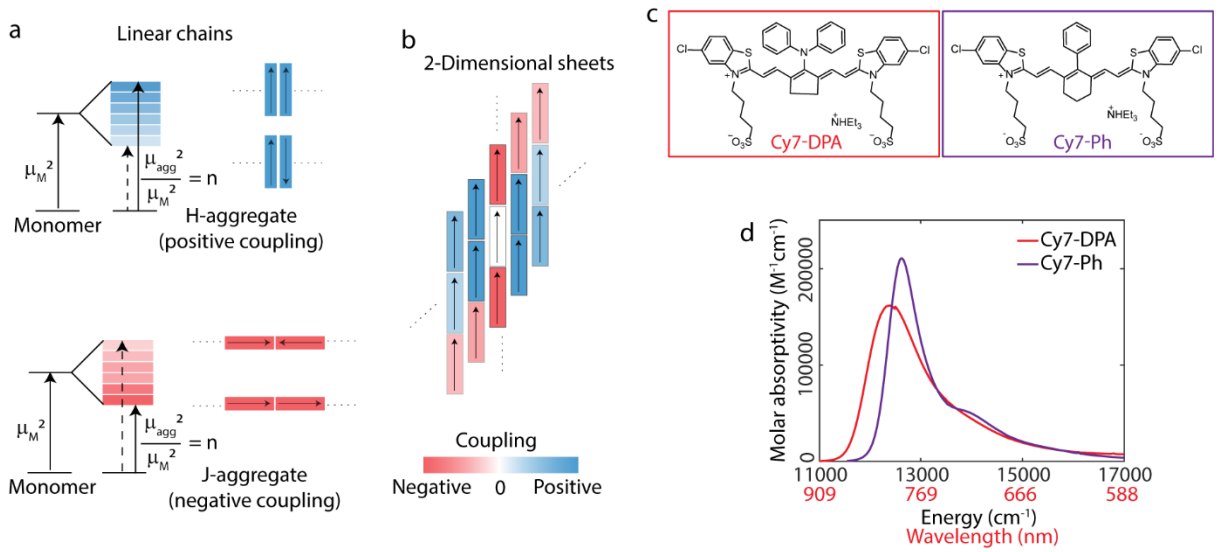

Figure 2.1. Excitonic couplings in 1D and 2D aggregates, structures and monomer spectra

a. Schematic depicting H- and J-aggregation for dimers and linear chain aggregates based on Kasha's model, n is number of monomers in the chain, μ_M and μ_{agg} denote transition dipole moments of monomer and aggregate respectively, b. A schematic depiction of coupling of a central brick (white) within a 2-dimensional aggregate with its neighbors, c. Molecular structures of the cyanine dyes investigated, d. Absorption spectra of the dyes in their monomeric form in methanol solutions.

The net coupling would be determined by bricks along all directions. Even though several experimental[39,90] and theoretical[30,109] examples of 2D aggregates are known, general principles to tune absorption through control over molecular stacking during self-assembly are limited. In this manuscript, we show how controlling 2D aggregation slip-stacking can be used as an approach for further red shifting the absorption, and that additional control is needed to create emissive aggregates.

Many H- and J-aggregates have been reported based on small molecule chromophores like cyanines,[12] perylene bisimides,[110,111] porphyrins[14,112] as well as for more extended structures like conjugated polymers,[26] and pigment-proteins.[1] Kasha's model and its variations[26,113] have been critical in describing the rich photophysics in such systems. We focus on cyanine dyes – a class of dyes which consist of a polymethine bridge connecting to two aromatic heterocycles. Cyanine dyes are particularly interesting because of their tendency to self-assemble into different topologies including dimers, single and double-walled nanotubes, bundles and sheets.[88,89,114] As a class, cyanine dyes exhibit large TDMs (as high as 10 D) and a high degree of structural and spectral tunability.[12,115] Recently, long-range exciton migration was shown in double-walled nanotubes of cyanine dyes in the visible region.[116,117] Owing to these properties, cyanine dyes are extensively employed for biological imaging, Förster resonance energy transfer (FRET), nonlinear optics and photoredox reactions.[46,58,64,66,118]

In this chapter, we exploit molecular aggregate structure and dimensionality to achieve new materials with high absorption cross sections above 1000 nm. Through control of solvation conditions, we observe the aggregation of two NIR thiacarbocyanines dyes (Figure 2.1c) into multiple morphologies (like sheets, dimers) with unique spectral shifts. Here we focus on their

most redshifted forms, which were found to be sheet-like structures with almost micron scale domains. These structures display strong ($\varepsilon \sim 10^5\ M^{-1}cm^{-1}$) SWIR absorption, though little to no direct emission. To connect the observed photophysics to structure, we construct an analytical model based on long-range TDM coupling and calculate the density of states (DOS) and other optical properties. Unique to the sheet morphology, we describe an 'I-aggregate' one which exhibits intermediate photophysics between J- and H-aggregates, a red shifting yet non-emissive structure. Temperature dependent absorption spectroscopy experimentally confirms the model, distinguishing the I- and J-aggregates. Finally, we relate our results to the dye structures and induced slip, in analogy to Kasha's rules to elucidate design principles for controlling the photophysics of 2D aggregates.

2.2 Using aggregation to red shift absorptions into shortwave infrared

We obtain dyes 3,3′-bis(4-sulfobutyl)-5,5′-dichloro-11-diphenylamino-10,12-ethylenethiatricarbocyanine, ammonium salt (Cy7-DPA) and 3,3′-bis(4-sulfobutyl)-5,5′-dichloro-11-phenyl-10,12-ethylenethiatricarbocyanine, ammonium salt (Cy7-Ph) from a commercial source. Previous work with similar cyanine dyes showed sheet-like aggregation in aqueous solutions, though detailed photophysical and structural insights were not provided.[114,119,120] Cy7-DPA and Cy7-Ph dyes, shown in Figure 2.1c, are structurally similar to each other apart from substitutions on their cyanine bridge which do not significantly alter their monomer absorption (Figure 2.1d). This makes them optimal candidates for comparing the effect of dye structure on aggregate formation and photophysics. Monomer absorption peaks of Cy7-DPA and Cy7-Ph lie in NIR at 807 nm (12,391 cm^{-1}) and 792 nm (12,626 cm^{-1}) respectively.

Adapting procedures from previous literature,[21,88] we explored the phase space of aggregation. Unlike previous aggregation routes, which use direct dissolution of dye into water or brine, pH modification and templating,[47,114,121,122] we pre-dissolve the dyes in methanol prior to mixing with water following the so-called "alcoholic route" to self-assembly.[77] This procedure allows for independent control over methanol-water ratios and dye concentration, and aggregates form relatively rapidly (~ 24 h). In Figures 2.2a-b, we show selected absorption spectra of aggregates where we fixed the dye concentration at 0.2 mM while varying the methanol-water ratios from 0-100% MeOH v/v (complete range shown Section 2.7, Figure 2.5). We observe sharp red-shifted J-like aggregate peaks in SWIR at lower methanol-water ratios (%MeOH) for both the dyes. The J-like peak of Cy7-DPA lies in SWIR at ~1050 nm (9524 cm^{-1}) while that of Cy7-Ph lies at ~1000 nm (10,000 cm^{-1}). As we increase the %MeOH, the J-like peak decreases and the monomer peak increases for both the dyes (Figure 2.5). At 50% MeOH, we observe an H-aggregate peak at 698 nm (14,327 cm^{-1}) for Cy7-Ph whereas Cy7-DPA shows a second J-like peak (J2) at ~1000 nm (10,000 cm^{-1}) under the same conditions. We hypothesize that the diphenylamine (DPA) group in Cy7-DPA frustrates cofacial packing and as a result, we never observe an H-aggregate peak in Cy7-DPA.

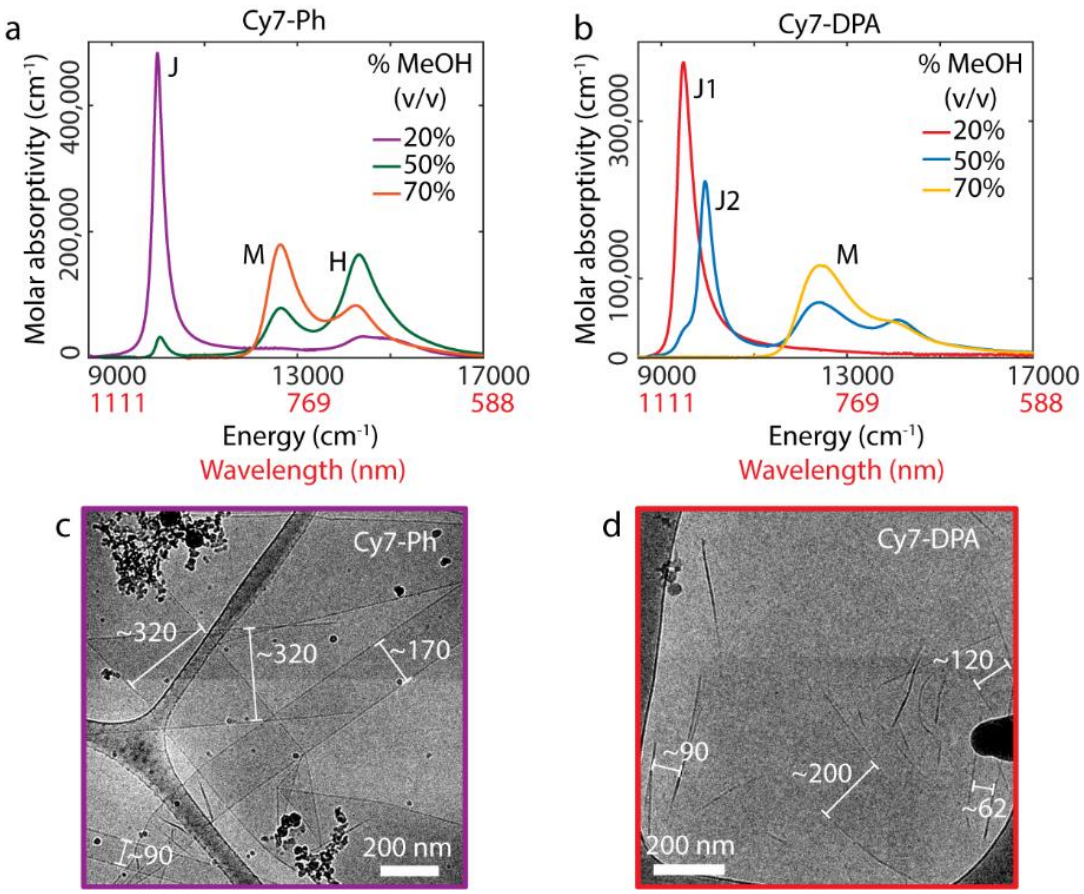

Figure 2.2 Aggregates of Cy7-Ph and Cy7-DPA

Top: Selected absorption spectra of a. Cy7-Ph and b. Cy7-DPA aggregates prepared by mixing methanol solutions of the dyes with deionized water with 20, 50 and 70% methanol (v/v). Final dye concentration was kept constant (0.2 mM) for all samples. 20% samples show a sharp redshifted peak in SWIR. Bottom: Cryo-electron micrographs of the most redshifted aggregates of c. Cy7-Ph and d. Cy7-DPA showing 2D sheet-like morphology. Numbers indicate sheet widths in nanometers.

We perform cryo-electron microscopy (cryoEM) on the most red-shifted samples. CryoEM of the 10% MeOH samples reveals sheet-like morphology with large planar domains extending over hundreds of nanometers indicating the presence of long-range order in the J-aggregates (Figure 2.2c-d). Similar sheet-like morphology and absorption lineshapes were observed for Cy5 and Cy7 thiacarbocyanine dye aggregates.[89,114] For a more global verification of domain sizes, we

performed dynamic light scattering (DLS). Estimates of domain sizes obtained from DLS agree well with cryoEM data with the smallest average across multiple trials being ~ 700 nm for Cy7-DPA and ~ 900 nm for Cy7-Ph (Figure 2.6). We were unable to isolate the J2 morphology under tested conditions. However, because of its characteristic peak shape,[114] we hypothesize that the J2 peak on Cy7-DPA also arises from a sheet morphology with slightly different dye packing. The shoulder on J2 is from some conversion to J1. From a concentration dependence study (Section 2.7 and Figure 2.7), we assign the H-peak of Cy7-Ph to a dimer.[123]

2.3 Frenkel exciton model for 2D aggregates

The presence of large domains and narrow linewidths suggests that the aggregates have long-range delocalization of their transition dipole moments. We model the aggregate photophysics following the Frenkel exciton model with extended dipole treatment developed by Kuhn and co-workers.[25,29] First, following convention,[124] we consider a monomer as a brick with an internal dipole representative of the TDM generated by a single excitation (Figure 2.3a). We then tile the bricks with a single variable parameter, the slip (s), which represents the displacement along the long axis and construct the sheet (Figure 2.3a). Basing on the standard Frenkel exciton Hamiltonian,[25]

$$H_s = \sum_{\boldsymbol{n}\neq\boldsymbol{m}} J(\boldsymbol{n},\boldsymbol{m})|\boldsymbol{n}\rangle\langle\boldsymbol{m}| + \sum_{\boldsymbol{n}} \epsilon_{\boldsymbol{n}}|\boldsymbol{n}\rangle\langle\boldsymbol{n}| \tag{2.1}$$

where $|\boldsymbol{n}\rangle$ represents the state where the $\boldsymbol{n}^{\text{th}}$ molecule is in the excited state while all others in the ground state, $J(\boldsymbol{n},\boldsymbol{m})$ the excitonic coupling between the two molecules, and $\epsilon_{\boldsymbol{n}}$ is the individual site energy. Boundary effects are resolved by imposing periodic boundary conditions, $J(\boldsymbol{n},\boldsymbol{m}) = J(\boldsymbol{n}-\boldsymbol{m})$. We then diagonalize the Hamiltonian, $H_s = \sum_k \epsilon_k|k\rangle\langle k|$, where $|k\rangle$ is the

k^{th} eigenstate with energy ϵ_k. For planar aggregates with one transition per unit cell, we obtain only a single state with finite oscillator strength $\mu_k = \mu_0 \left|\sum_{\boldsymbol{n}} \langle k|n\rangle\right|$, when all transition dipoles are in-phase (no nodes along either direction). This is the state that can absorb or emit light and is referred to as the *bright state*. All other excitonic states contain at least one node, and thus are optically dark. We further calculate the density of states (DOS), $D(E) = \sum_k \delta(E - \epsilon_k)$, as well as the energy of the bright state as a function of slip (see section 2.7 and Figures 2.8-2.9) for the 2D aggregates.

The results from this model are summarized in Figure 2.3b, where we set $\epsilon_{\boldsymbol{n}} = 0$ for clarity. We observe, for 0 nm slip, an H-aggregate with the bright state blue shifted from the monomer. For higher slip values such as 0.7 nm, we observe a typical J-aggregate with a lower band-edge bright state. Interestingly, for intermediate slip values like 0.4 nm, the bright state is still red-shifted from the monomer, but notably, *not at the band-edge*. We associate this case to an 'I-aggregate', or intermediate aggregate as it displays a red-shifted bright state like J-aggregates but has excitonic states below the bright state, similar to H-aggregates. In other words, I-aggregates have a bright state which lies in the middle of the DOS but red-shifted from the monomer. I- and J-aggregates cannot be distinguished simply from their absorption spectra. We use their temperature dependent linewidth to determine where the bright state sits in the density of states.

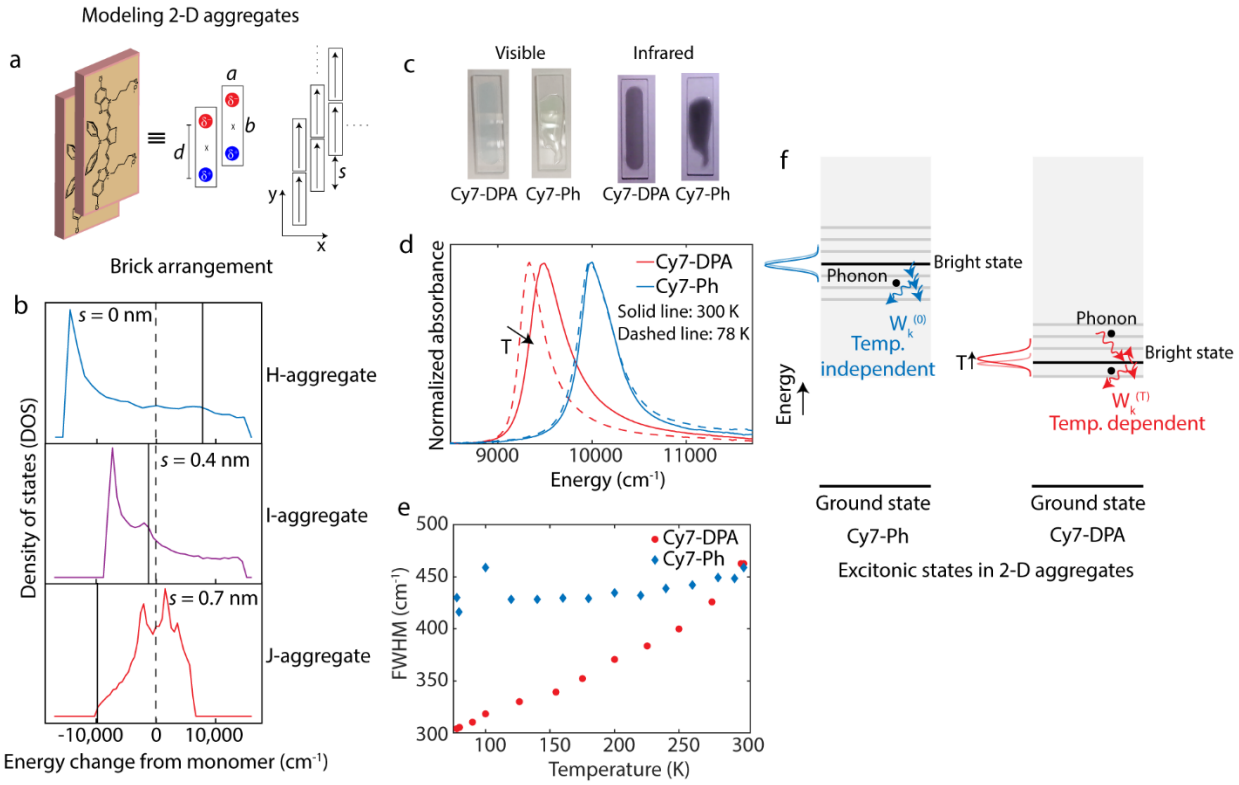

Figure 2.3. Frenkel exciton model for 2D aggregates with extended dipole treatment, temperature dependence of Cy7-Ph and Cy7-DPA

a. Schematic depiction of the brick arrangement model; b. Results from the analytical model showing monomer energy (dashed line) and relative position of the bright-state (solid line) within the density of states for 0, 0.4 and 0.7 nm slips; c. Pictures of sugar matrix stabilized aggregates as seen through a typical silicon camera with an IR filter (left) and with the IR filter removed and an 850 nm longpass filter added to remove stray light (right); d. Absorption spectra of sugar matrix stabilized aggregates- Cy7-DPA (red) and Cy7-Ph (blue) at 300 K (solid lines) and 78 K (dashed lines); e. Full-width at half-maximum (FWHM) of the absorption peak as a function of temperature for Cy7-DPA (red circles) and Cy7-Ph (blue diamonds); f. Schematic describing the processes that contribute to the lineshape of Cy7-Ph and Cy7-DPA.

We perform temperature dependent absorption spectroscopy on matrix stabilized Cy7-DPA and Cy7-Ph aggregates (20% MeOH). We prepare the stabilized aggregates using a previously reported sugar matrix stabilization procedure (pictures shown in Figure 2.3c).[117,125] Comparison of solution and sugar matrix stabilized aggregates (Figure 2.12a) strongly suggests that the

aggregate morphology remains intact in sugar matrix. Upon cooling down from room temperature to 78 K, we find that the full-width at half-maximum (FWHM) of Cy7-DPA peak narrows from 463 cm^{-1} to 303 cm^{-1} (34 %) and red shifts by 150 cm^{-1} as shown in Figures 2.3d-e. On the other hand, absorption of Cy7-Ph barely changes upon cooling. The peak position of Cy7-DPA is similarly sensitive to temperature as it red-shifts upon cooling while that of Cy7-Ph barely changes (Figure 2.12b).

The effect of temperature on absorption lineshape is described by the origin of fluctuations that dephase the ground-excited state coherence. The absorption spectrum is the Fourier transform of the transition dipole autocorrelation function,[107]

$$A(t) = \langle a(t) \rangle \approx \langle e^{-i\epsilon_{\mathrm{b}} t - W_{\mathrm{b}} t} \rangle \tag{2.2}$$

where ϵ_{b} is the energy gap between ground and excited state and W_{b} represents how the system's interaction with the bath leads to energetic fluctuations that dephase the phase relationship between ground and excited state wavefunctions. The brackets represent averaging over inhomogeneous disorder, or fluctuations in the environmental degrees of freedom slower than the lifetime of the exciton. Using the Redfield framework for exciton dynamics, and imposing the secular approximation and Markovian bath, we express W_{b} for each exciton as follows:[126–128]

$$W_k = \sum_{l \neq k} \frac{O_{kl}}{e^{(\epsilon_l - \epsilon_k)/k_{\mathrm{B}} T} - 1} D_b(\epsilon_l - \epsilon_k) \tag{2.3}$$

where $O_{kl} = \sum_n |\langle k|n\rangle\langle n|l\rangle|^2$ is the wavefunction overlap between the excitonic states, k_{B} is the Boltzmann constant, and $D_b(E) = -D_b(-E)$ is the antisymmetrized bath spectral density. For homogeneous, translational invariant systems the secular approximation is by construct exact.[124] On the other hand, Markovian approximation is justified for fast dissipating environment. While

this is not necessarily true for the systems under consideration, as exemplified by the existence of vibronic progression observed in both monomer spectra (Figure 2.1d), the line width and its temperature dependence are well captured by the Markovian contribution.[25] While the inhomogeneous contribution to the linewidth is mostly temperature independent, one can further breakdown the homogeneous linewidth (or dephasing rate) W_k into (i) stimulated absorption/emission of phonons and (ii) spontaneous emission of phonons and relaxation to band-edge.

$$W_k = \sum_{l \neq k} \frac{O_{kl}}{e^{|\epsilon_l - \epsilon_k|/k_B T} - 1} D_b(|\epsilon_l - \epsilon_k|) + \sum_{\epsilon_l < \epsilon_k} O_{kl} \cdot D_b(\epsilon_k - \epsilon_l) = W_k^{(T)} + W_k^{(0)} \tag{2.4}$$

Here, $W_k^{(T)}$ represents the stimulated absorption/emission portion, and thus depends on the thermal occupation of phonons (making it temperature dependent) whereas the $W_k^{(0)}$ relies on the available DOS below the bright state and is temperature independent.[112] In Cy7-Ph aggregates, we observe minimal change with temperature implying that the second term (relaxation to band-edge through spontaneous emission of phonons) is more dominant in the lineshape function. This implies sufficient DOS below the bright state, matching the description of an I-aggregate (Figure 2.3b). On the other hand, we observe a significant narrowing upon cooling in Cy7-DPA which suggests that the first term dominates the lineshape function. Therefore, Cy7-DPA must have a bright state that is thermally accessible from the band-edge. We explain this in Figure 2.3f where the left side shows spontaneous emission of a phonon and the subsequent relaxation to the lower

energy state. This process is governed by the term $W_k^{(0)}$ of equation (2.4) which is temperature independent. Right side of Figure 2.3f shows stimulated emission of phonons, governed by $W_k^{(T)}$ which depends on the thermal occupation of phonons. As a result, the spectrum shown on the left (blue) doesn't change with temperature while the one on right (red) broadens with increasing temperature. Simply put, when the bright state is near the band-edge, it's lineshape will be temperature dependent. As it moves away from the band-edge, the lineshape is dominated by temperature independent relaxation within the density of states. Despite both Cy7-Ph and Cy7-DPA appearing to "J-aggregate" from their absorption spectra, the temperature dependence strongly suggests that the bright state is not at the band-edge.

2.4 Design principles for 2D aggregates

To correlate the structural parameters (slip) and spectroscopic observables, we calculate the DOS and bright state for generalized 1D and 2D aggregates as a function of slip (Figure 2.4a). We use a set of general parameters shown in Table 2.1, which represent the average of calculations used to determine the extended dipole parameters for Cy7-DPA and Cy7-Ph section 2.7). We express the coupling in terms of the variable J, defined as the coupling of a nearest neighbor head-to-tail dimer (J = -2000 cm^{-1}) calculated using extended dipole model (eq. (2.10)), and the slip in terms of the length of the brick (b). The maximum and minimum eigenvalues define the upper and lower band-edge of the DOS and the region between the two extremes represents the exciton bandwidth. As seen from Figure 2.4a, 1D aggregates follow Kasha's framework, always displaying (upper or lower) band-edge bright states irrespective of the slip. In 2D aggregates we observe regions H-, I- and J- aggregation (color-coded blue, purple and red respectively in Figure 2.4a) based on the position of the bright state within the DOS. The point where the bright state intersects the zero coupling line corresponds to a previously reported 'null aggregate' meaning

that there is no excitonic shift even though the exciton bandwidth is large.[129,130] Furthermore, 2D aggregates display increased possible spectral shifts due to stronger coupling. This unique band structure is a direct consequence of the 2D topology (Figure 2.13) and stems novel photophysical properties of 2D aggregates.

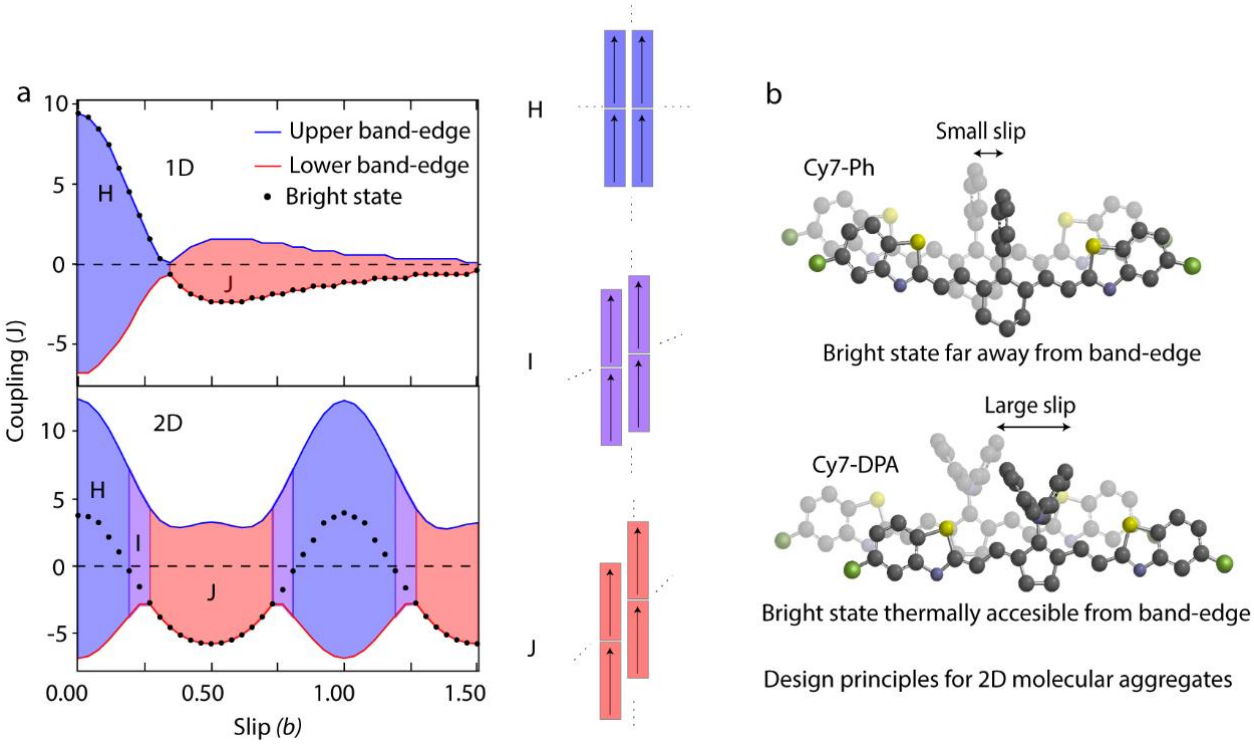

Figure 2.4. Slip dependence of the band structure for 1D and 2D aggregates, schematic of design principles for 2D aggregate

a. Bright state (black dots), upper (blue) and lower (red) band-edge of the excitonic band as a function of slip for 1D (top) and 2D (bottom) aggregates with non-nearest neighbor coupling. J is coupling for a head-to-tail dimer and b is the length of the brick. B. Schematic depiction of molecular design principles for 2D aggregates (alkyl chains have been omitted for simplicity). Packing with higher slip results in a bright state closer to the band-edge.

Table 2.1. List of parameters used in the Frenkel exciton model

$\boldsymbol{a}$ and $\boldsymbol{b}$ are the short and long axes of the brick respectively, $\boldsymbol{\mu}$ is the transition dipole moment and $\boldsymbol{d}$ is the charge distance for the extended dipole.

	$\boldsymbol{a}$ (Å)	$\boldsymbol{b}$ (Å)	μ ($\boldsymbol{D}$)	$\boldsymbol{d}$ (Å)
Cy7-DPA	7.3	19	4.2	9
Cy7-Ph	8.8	22	4.0	3.5
Generalized	8.1	21	4.1	6.3

Similar behavior plays an important role in conjugated polymer photophysics (HJ aggregates) wherein, changing the relative strength of intra-/interchain coupling gives a mid-band bright state.[7,129] While polymer networks involve covalent coupling along the polymer backbone and dipole-dipole coupling between the polymer chains, their absorption spectra have strong analogies to the Van-der-Waals aggregates described here. It is worth mentioning that these HJ aggregates have mid-band bright states that are not necessarily red shifted from the monomer whereas I-aggregates have mid-band bright states red shifted from the monomer. Furthermore, epitaxially grown 2D crystals of a perylene based dye also resulted in a similar observation where limited aggregate size with non-unity aspect ratios gave dark band-edge J-aggregates.[39] In this case, even with a dark band-edge, the next higher energy state was bright. Due to the extended nature of these 2D I-aggregates, the bright state position in the density of states is a nearly continuous function of the slip as seen from Figure 2.4a, and is thus tunable using chemical modification. Size control of self-assembled aggregates is challenging in solution. However, many SWIR applications demand solution aggregates for processability and biological compatibility. Our approach enables chemical control of the slip while also being more versatile.

Another recent theoretical investigation of 2D aggregates based on a simple dipole model demonstrates that temperature dependent peak shifts in absorption can be related back to structural

parameters like slip, however, they observe I-aggregate like behavior at higher slips.[131] Temperature dependent behavior of the bright state is dominated by the short-range interactions which depend strongly on the type of Hamiltonian used. Cy7-Ph shows little change in peak position while Cy7-DPA blue-shifts with increasing temperature, consistent with having different slip parameters (Figure 2.12b). Using our classification scheme, we estimate that the slip for the Cy7-Ph is ~ 4-5 Å and that for Cy7-DPA is between 7-10 Å. In general, the steric hindrance due to the DPA group will prohibit slips that are less than 7 Å (which correlates to 0.36 times its brick length), consistent with our observation that Cy7-DPA has a bright state closer to the band-edge than Cy7-Ph (Figure 2.4b). It is difficult to quantitatively compare our model to the experiment owing to the complexities arising from modeling the structural nature of disorder and variance in the system dielectric.[132–134] The differences induced by the substituent on the proximity of the bricks may affect the actual coupling values but they won't affect the overall behavior of H-, I- and J- aggregation significantly.

Using an approximate slip parameter of Cy7-Ph we introduce diagonal disorder to fit the absorption FWHM and estimate the number of sites that participate in a given exciton. Focusing on Cy7-Ph which has a narrower range of likely slip parameters, we calculate the linewidth for a range of disorder values and compare to our experimental spectra. From this, we estimate that the diagonal disorder is ~200 cm^{-1}, and the inverse participation value is ~8 (Figure 2.14). Despite relatively strong disorder, the high degree of coupling in a 2D aggregate enables long-range delocalization lengths even at room temperature. This strongly implies that a band picture is appropriate in describing the relevant photophysics (Figure 2.13).

2.5 Conclusions

We conclude by suggesting that in direct analogy to 1D aggregates described by Kasha's model, 2D brick-like aggregates can be tuned through control of the slip parameter. In general, in 2D aggregates, a slip value less than 0.18 times the brick length forms an H-aggregate while a slip value greater than 0.26 times the brick length produces a J-aggregate. Interestingly, the remaining intermediate values result in I-aggregation which shows characteristics of both J- and H-structures. The observed spectroscopic behavior of Cy7-Ph and Cy7-DPA is thus directly correlated to dye structures.

Our results demonstrate the significance of aggregate morphology and packing as a new avenue for tuning excitonic properties. In general, 2D aggregates with strong SWIR absorption can be made by simply tuning the solvation environment of NIR dyes. However, for 2D aggregates, the position of the bright state depends on the slip and is not restricted to the band-edge unlike linear or dimer aggregate systems allowing for emergent photophysics. Using temperature dependence, we confirm that Cy7-Ph forms an I-aggregate with dark states below the bright state. Cy7-DPA also forms an I-aggregate but has a bright state closer to the band-edge because of higher slip induced by the bulkier DPA group. This may explain why both the aggregates were not emissive. Nevertheless, 2D aggregates follow a generalized classification scheme which provides a roadmap to designing custom chromophore assemblies with desired properties. For example, the central position on the cyanine bridge may be further modified with bulkier groups to induce greater slips between chromophores to achieve band-edge J-aggregates.

We can exploit the 2D topology to access unique excitonic properties and employ them for NIR and SWIR antennas. Wang *et al*. demonstrated enhanced FRET efficiency between a quantum

dot pair when mediated by a SWIR absorbing J-aggregate.[46] This occurs despite the apparent low quantum yield of the aggregate suggesting I-aggregate mediated transport. I-aggregates present the possibility of energy transfer via dark states that can be accessed via near-field coupling similar to LH2 complex in photosynthetic bacteria.[135] Recently, a theoretical study showed dark states in 2D aggregates can be accessed via near-field coupling.[136] Anantharaman *et al*. reported platelets of another Cy3 dye which show very small narrowing with decreasing temperature, suggesting that the platelets might be I-aggregates.[121] The interesting aspect of I-aggregates– a red-shifted bright state far away from the band-edge– provides opportunities for NIR/SWIR absorption and charge injection into another semiconductor in photovoltaics enabling a complete utilization of the solar spectrum[26,137,138] as well as for exploring fast energy transfer from I-aggregates to enhance the emission of NIR/SWIR materials.[139] Recent studies have shown deep-tissue imaging of mice vasculature using flavylium polymethine dyes with monomeric SWIR emission.[74] Chemical modification of such dyes following the principles outlined here could enable J-aggregation, pushing them deeper into the SWIR with high molar absorptivity needed for low dosage amounts. Furthermore, these materials open the possibilities for exciton-polariton coupling at telecom relevant wavelengths for antennas and other nanoscale optical devices.[51]

2.6 Experimental methods

Materials: Cy7-DPA and Cy7-Ph were obtained from FEW chemicals GmbH (catalog no. S0837 and S2433). Spectroscopic grade methanol, sucrose and D-(+)-trehalose were obtained from ThermoFisher Scientific. All materials were used as obtained, without any further purification. Deionized water (18 MΩ) was used for making all samples.

Sample preparation: Cuvettes and sample vials were pre-soaked in deionized water for hydrophilization. Dyes were pre-dissolved in methanol to make different concentrations of monomer solution. The monomer solution was then added to deionized water in a specific volume/volume ratio to prepare the aggregate solution. All solutions were stored in foil covered and parafilm sealed vials for 24 h before taking any measurements. For scanning the whole % MeOH range (10-100%) while keeping the dye concentration constant, the starting concentration of monomer solution was adjusted accordingly for each sample. For concentration dependence of the H-aggregate, % MeOH was kept constant at 70% white the final concentration was varied (0.05-0.5 mM). Samples for temperature dependence were prepared by sugar-matrix stabilization method previously reported.[117] Dye aggregates were first prepared in water-methanol solutions as mentioned above and stored for 24 hrs to let the aggregates assemble. A saturated sugar solution was made by dissolving a 50:50 sucrose:trehalose (wt./wt.) mixture in distilled water. To a 100 μL aggregate solution, 100 μL of the saturated sugar solution was added slowly and gently mixed. This solution was drop-cast onto a 0.2 mm quartz cuvette and kept under vacuum in dark for 24 hrs. CryoEM samples were prepared on mesh 200 lacey formvar/carbon copper grids obtained from Ted Pella Inc. The grids were plasma cleaned under a H_2/O_2 gas flow using Solarus Gatan Plasma cleaner for hydrophilization. Vitrobot Mark IV was used for plunge freezing the samples. About 3.5 μL of the aggregate solution was dropped onto the grid, excess solution was removed by blotting for 3.0 s with standard blotting paper from Ted Pella and immediately dropped into liquid ethane maintained close to its freezing point using liquid nitrogen. The frozen grids were stored in liquid nitrogen.

Measurements: All spectra were taken in a 0.2 mm path length quartz cuvette obtained from Starna Cells Inc. All room temperature absorption spectra were taken on a JASCO V-770 UV/Vis/NIR

spectrometer. Temperature dependent absorption measurements were performed using a Shimadzu UV/Vis/NIR spectrometer inside a liquid nitrogen cooled Janis ST-100 cryostat. Lakeshore 330 Autotuning Temperature Controller was used to control the temperature. CryoEM images were recorded on a FEI TF20 electron microscope equipped with a field emission gun at 200 kV. CryoEM grids were loaded on to a Gatan 626 cryo-transfer sample holder, then inserted into the microscope and images were taken, all under liquid nitrogen. Images were recorded on a CCD camera with 4k x 4k resolution. Image defocus was used to enhance contrast. DLS experiments were performed on a Coulter Beckman Dynamic Light Scattering Analyzer in 1 cm path length cuvettes.

2.7 Supporting information

This section covers additional details about the results discussed in this chapter – aggregate spectra over complete % MeOH, dynamic light scattering of the 2D aggregates, concentration dependence to obtain the aggregation number of H-aggregate, a beginner student level description of the modeling methodology used in this paper, sugar matrix stabilization, excitonic states for 1D and 2d aggregates in k-space and estimation of exciton delocalization lengths.

Aggregation of Cy7-DPA and Cy7-Ph in methanol-water mixtures

We form a monomer stock solution by dissolving the dyes in methanol. We then mix the monomer solution with deionized water in varying volume/volume fractions. We keep the final dye concentration constant modifying the concentration of stock solution accordingly. Fig. 2.5 show the variation of the aggregate and monomer peaks (2.2a-b) for the whole range of %MeOH.

We obtain an average transition dipole moment (TDM,μ) from the absorption spectra for both the dyes using equations 1a and 1b:

$$f = 4.3 \times 10^{-9} \int \varepsilon \, d\bar{\nu} \qquad \text{(1a)}, \quad \langle \mu \rangle^2 = \frac{3he^2}{8\pi^2 m\bar{\nu}} f \qquad (2.5)$$

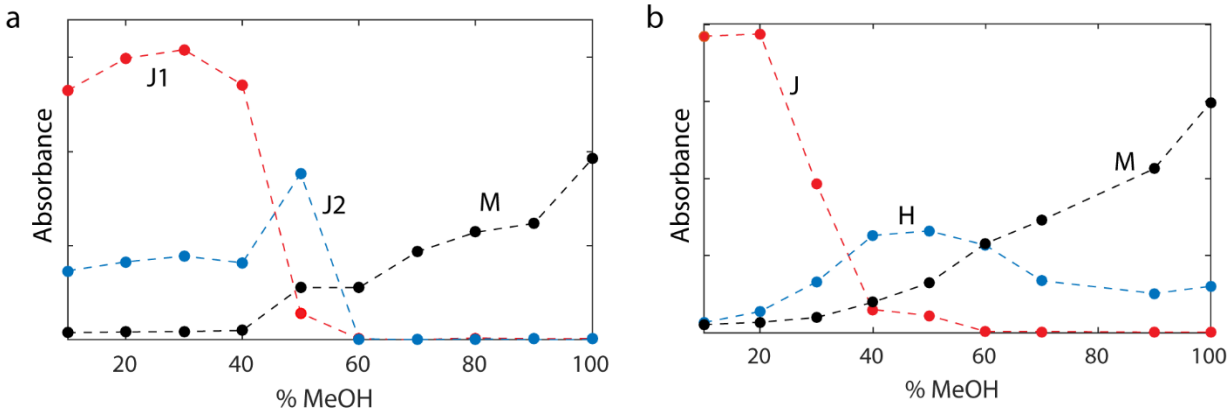

Figure 2.5. Aggregate and monomer peaks across full %MeOH range

Peak values for each aggregate and monomer peak (from Fig. 2.2a-b) as a function of %MeOH (0-100%) for a. Cy7-DPA and b. Cy7-Ph.

where f is the oscillator strength, ε is the molar absorptivity, $\bar{\nu}$ is the peak wavenumber, m and e are the mass and charge of an electron and h is Planck's constant.[104,140] The average TDMs were 4.2 $\pm$ 0.9 D and 4.0 $\pm$ 0.5 D for Cy7-DPA and Cy7-Ph respectively.

Dynamic Light Scattering (DLS)

Cryo-electron microscopy reveals sheet-like morphologies for Cy7-DPA and Cy7-Ph aggregates with widths varying from ~ 100-300 nm and lengths up to micron scale. Sheets of Cy7-Ph appear to be longer than C7-Ph. For a bulk estimate of aggregate sizes, we performed dynamic light scattering (DLS) on the J-aggregates of Cy7-DPA and Cy7-Ph. We approximate particle sizes from the intensity distribution following the treatment done by Lotya et al.[141] The particle size estimates are shown in Figure 2.6 and agree well with the aggregate extent shown in cryoEM images.

Concentration dependence of H-aggregate

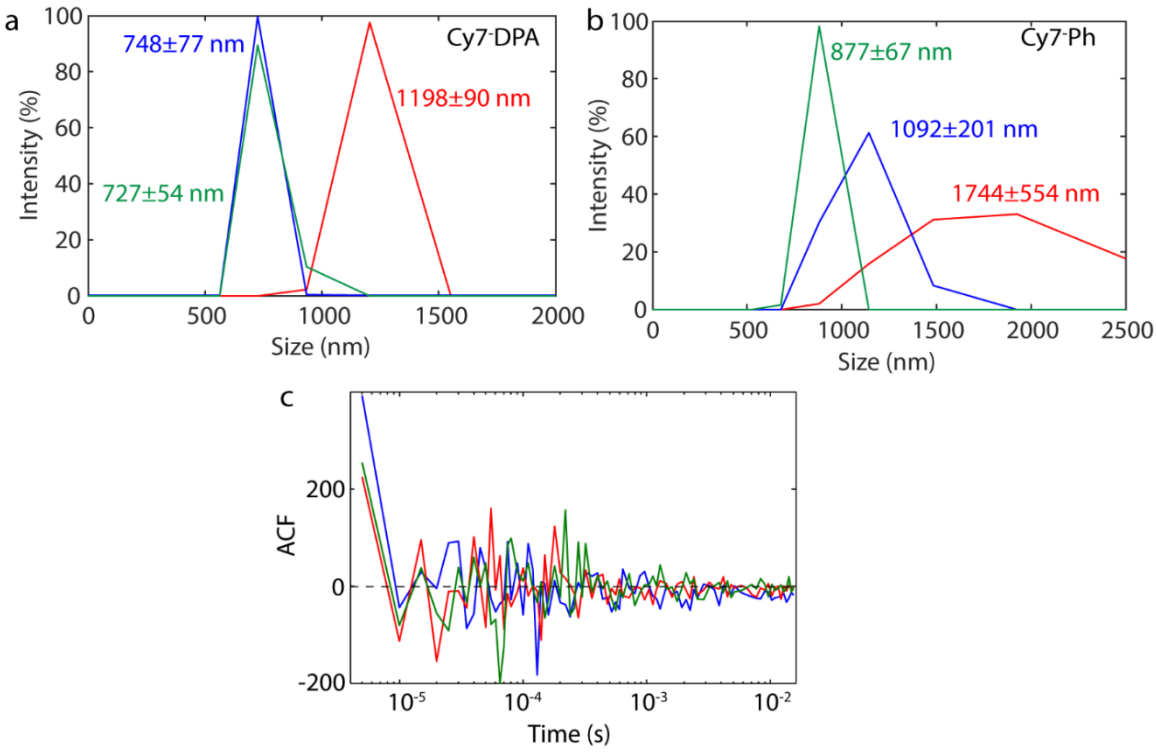

Figure 2.6. Dynamic light scattering of Cy7-Ph and Cy7-DPA

DLS intensity distributions for a. Cy7-DPA and b. Cy7-Ph, 20% MeOH aggregate samples. (c) Auto-correlation function (ACF) of the solvent mixture (20% MeOH) showing no contribution coming from the mixture. Red, green and blue curves represent

To assign the H-aggregate peak in Cy7-Ph (Figure 2.2a), we observed concentration dependence of the 70% MeOH sample.[123] In this case, the %MeOH was kept constant while the total concentration of the dye was changed from 0.05-0.5 mM. The relative changes in the peak absorbances for monomer and H-aggregate peaks were used to obtain the number of monomers in the H-aggregate (dimer v/s extended aggregate) using the following set of equations:

$$nM \rightleftharpoons H \qquad (2.6a)$$

$$K = \frac{C_H}{(C_M)^n} \qquad (2.6b)$$

Taking log and rearranging,

$$\log(C_H) = \log(K) + \mathrm{n} * \log(C_M) \qquad (2.6c)$$

where M and H denote the monomer and H-aggregate respectively. K is the equilibrium constant and C denotes the concentration of the species. C_M can be obtained from the absorption co-efficient of the monomer, $C_M = Abs_M/(\varepsilon_M \cdot l)$. The absorption co-efficient for the monomer was found to be 3.82 x 10^5 $M^{-1}cm^{-1}$. Although the absorption co-efficient of the H-aggregate cannot be accurately determined, we can use the absorbance of the H-aggregate (Abs_H) as a proxy. Since $Abs_H \propto C_H$, the proportionality constant would simply change the intercept of eqn. (2.7c). Using this approximation, we obtain eqn. (2.7d):

$$\log(Abs_H) - \log((\varepsilon_H \cdot l)) = \log(K) + \mathrm{n} * \log(C_M) \qquad (2.7d)$$

$$\log(Abs_H) = \log(K') + \mathrm{n} * \log(C_M) \qquad (2.7e)$$

where $K' = K/(\varepsilon_H \cdot l)$ is a constant. This equation is only valid for the slope. To obtain the equilibrium constant accurately, we will need to determine the concentration of the H-aggregated species.[123] Figure 2.7 shows a plot of $\log(Abs_H)$ v/s $\log(C_M)$, the linear fit gives $n =$

1.5 (0.7,2.3). This means that the H-aggregate peak at 698 nm (14326 cm^{-1}) can be assigned to H-dimer.

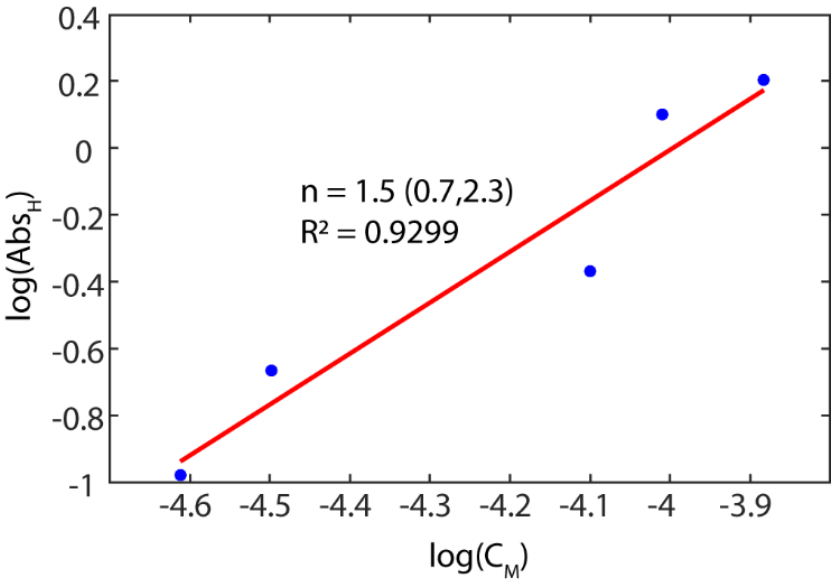

Figure 2.7. Extracting H-aggregate aggregation number from concentration dependence
Plot of $\log(Abs_H)$ against $\log(C_M)$ for H-aggregate samples (70% MeOH) with varying final concentration (0.05, 0.1, 0.2,0.5 and 0.5 mM). Straight line denotes a linear fit to equation (2.7e).

Extended dipole model

We adapt the Frenkel exciton theory for modeling the aggregates.[25,29] We start with an extended dipole model where we treat a molecule as rectangular brick with side lengths represented by a (short side) and b (long side) as shown in Figure 2.8. Along the long axis, we place partial charges of equal and opposite charge, equidistant from the center. From this charge separation, we calculate the magnitude of the transition dipole moment (TDM) on a single brick generated with one excitation. We build a sheet of similar bricks separated by the parameters a and b, where the nearest bricks are 'slipped' with respect to each other by a slip parameter s. Each brick is callable with a specific label or index. We use monolayer sheet in our model as the it's unlikely to affect the overall photophysics as suggested by previous literature.[77]

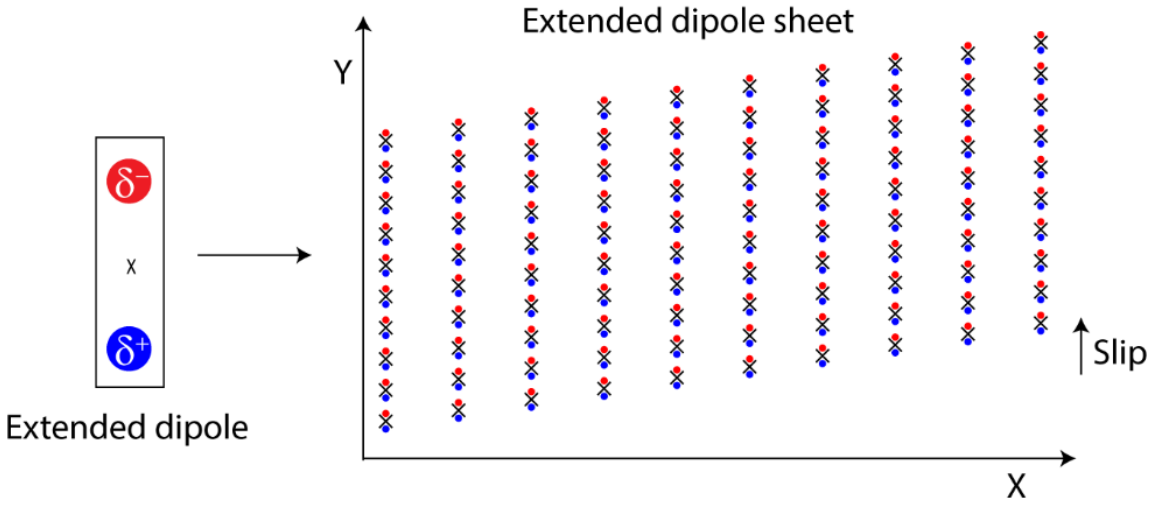

Figure 2.8. Schematic of extended dipole 2D aggregate

Schematic depiction (not to scale) of a magnified extended dipole brick (left) and a 2D aggregate sheet constructed from slipped arrangement of the bricks (right).

Frenkel Exciton Hamiltonian and Density of States (DOS)

Next, we construct the Frenkel exciton Hamiltonian from the electrostatic interaction between the TDMs. Represented in the site basis, the Hamiltonian is a matrix of dimensions $n \times n$, where n is the total number of bricks. Diagonal elements represent individual site energies and off-diagonal elements represent coupling energies obtained from equation 3:

$$J_{ext,n,m} \sim \frac{\mu^2}{d}\left(\frac{1}{r_{m+n+}} - \frac{1}{r_{m+n-}} - \frac{1}{r_{m-n+}} + \frac{1}{r_{m-n-}}\right) \tag{2.8}$$

where μ is the TDM per site, d is the charge distance per site and $r_{m\pm n\pm}$ is the distance between m^{th} and n^{th} charge.

As an example, we represent a coupling matrix for a 6x6 brick lattice (Figure 2.9). As expected, nearest-neighbor coupling is the largest contribution. We go on to add inhomogeneous site

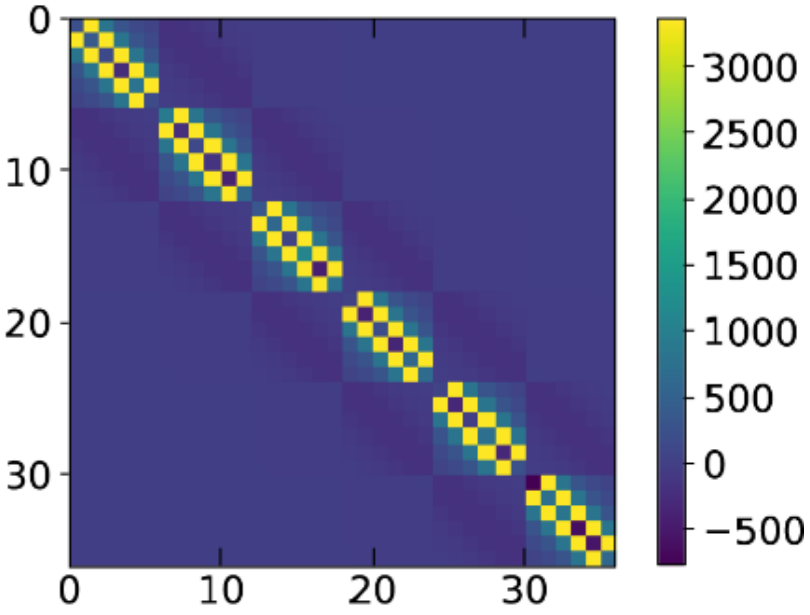

Figure 2.9. Example coupling matrix for a 6x6 aggregate.

disorder. With an open variance parameter, we draw from a normal distribution centered around the monomer energy. A variance of zero results in all sites with identical energy (same chemical

environments). A nonzero variance shifts each monomer by an individually chosen amount as shown by varying diagonal elements. To eliminate edge effects, we add periodic boundary conditions (PBC) that couple the initial aggregate to repeated *images* of the aggregate along both major axes. In the limit of large site numbers, edge effects become less significant. In our modeling (shown later in section 6) we find the delocalization length is limited to 8 sites. Introducing the PBC and, therefore, eliminating the edge effects can be justified.

Bright state energy and DOS

Diagonalizing the $n \times n$ coupling Hamiltonian produces n exciton energies corresponding to n exciton states (Figure 2.10). These eigenvectors are stationary exciton states, which can be written as a linear superposition of the states in the site basis. We then go on to obtain the density of states (DOS) by histogramming all the eigenvalues (energies) obtained from the Hamiltonian (Figure 2.3b). The optically active state (bright state) requires a net non-zero TDM as per Fermi's Golden Rule.[140] The net TDM per exciton was calculated as the sum of delocalization coefficients c_l (from eigenvectors) squared,

$$\mu_k = \left|\sum_{l=1}^{n} c_{k,l}\right|^2 \tag{2.9}$$

Summing before squaring accounts for the phase relationship between TDMs of each site. We obtain the absorption spectra by histogramming eigenvalues weighed by with their respective net TDM.

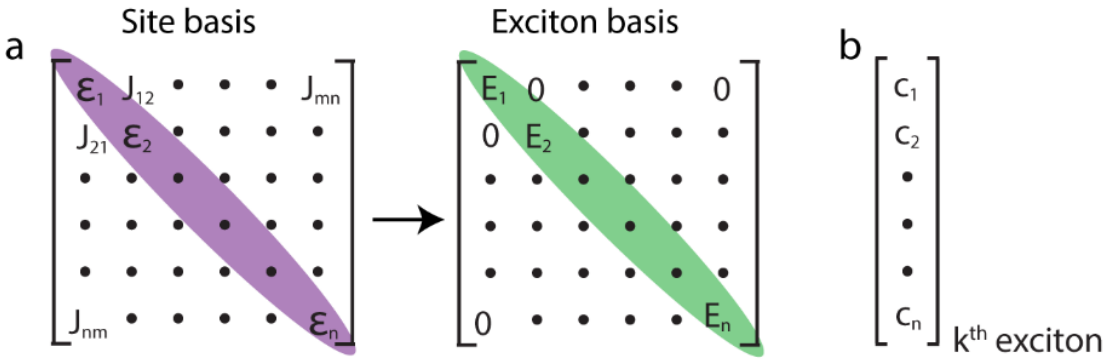

Figure 2.10. Depiction of Frenkel exciton Hamiltonian

a. Coupling matrix in site basis and its diagonalization to the exciton basis, b. Example eigenvector for k^{th} exciton where the coefficients correspond to the extent of delocalization over each site.

Approximating extended dipole model parameters for Cy7-DPA and Cy7-Ph

To model Cy7-DPA and Cy7-Ph, we obtain the transition charge densities of both dyes using a semi-empirical method in the software ZINDO/S.[142] The dyes were considered without the sulfonyl chains and with halogen groups replaced with methyl groups for simplicity. For an isolated monomer in vacuum, we optimize a ground state configuration using molecular modeling on Spartan and use it as an initial condition for ZINDO. We obtain many excited state transitions along with their net TDM, atomic coordinates of the excited state and the transition charges per atom. We select the transition with highest TDM as it represents the highest transition probability. Since the coupling calculation for many-dye systems is too computationally expensive with all charges considered, we fit extended dipole parameters for a dimer system to the dimer coupling calculated from transition charges. To start, we construct a dimer using the calculated transition charges obtained from ZINDO and compute coupling as a function of slip using the following eq.:

$$J_{dimer} \sim \sum_{i=1}^{n} \sum_{j=1}^{n} \frac{q_i q_j}{r_{ij}} = \sum_{i=1}^{n} \sum_{j=1}^{n} \frac{q_i q_j}{\sqrt{(x_i - x_i)^2 + (y_i - y_i + s)^2}} \quad (2.10)$$

where the numerator is the product of charges (one from each dye) and the denominator is the distance between these charges, n is the total number of transition charges per dye, and s is the slip. The total TDM per dye was calculated using the transition charge densities and distances relative to an arbitrary origin atom following eq.:

$$\mu = \sum_{i=1}^{n} q_i r_{i,0} \quad (2.11)$$

We scale this TDM to match experimental values obtained from the absorption spectra shown in Figure 2.5. We construct an extended dipole dimer with the scaled TDM and brick dimensions extracted from the atomic coordinates and an open charge distance parameter. We calculate the coupling for this dimer as a function of slip using eqn. (2.10). We vary the parameter d (charge

distance) until the two curves match to obtain a reasonable charge distance (Figure 2.11). The agreement is not the best for the entire range of slip values, but it fits well for smaller slip values which is where we expect our systems to be.

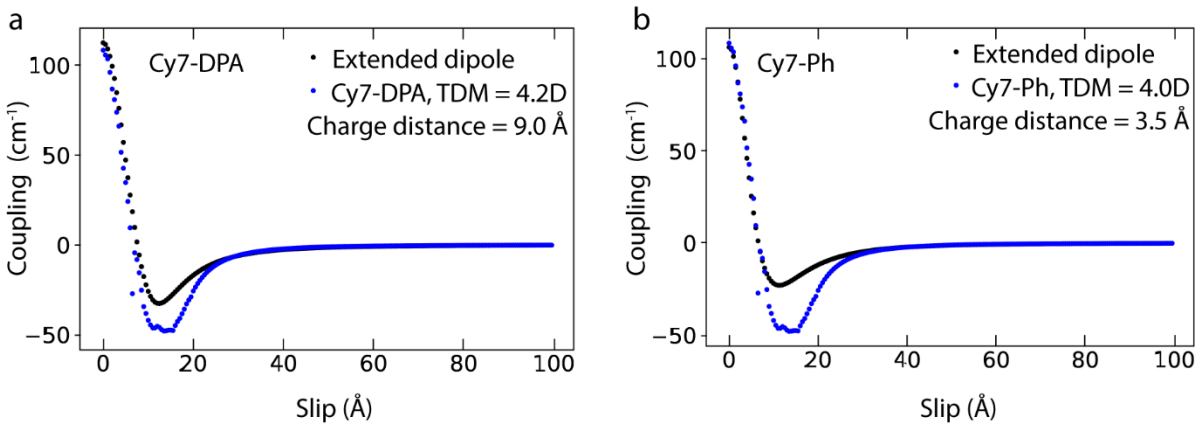

Figure 2.11. Fitting out the extended dipole parameters from transition charge density coupling calculations of dimers

a. Cy7-DPA and b. Cy7-Ph

We average the parameters of both dyes and use them to calculate the coupling matrices for 20x20 sheets at various slips. The complex dielectric environment in the aggregates gives rise to large long range coupling among monomer units. We approximate the dielectric environment by the scaling the coupling matrix by a factor of 70.54. This scaling factor is an approximation of the dielectric constant (weighted sum of dielectric constants of methanol and water). A more accurate description of the dielectric environment is outside the scope of this paper.

Sugar matrix stabilization and temperature dependence

We prepare the stabilized aggregates using a previously reported sugar matrix stabilization procedure.[117] Matrix stabilization allows the aggregates to maintain their morphology while keeping the samples optically transparent at low temperatures. Figure 2.12a shows the absorption spectra of solution and sugar matrix stabilized aggregates. Sugar matrix stabilization does not

affect the absorption of Cy7-DPA at all. It does, however introduce some disorder in Cy7-Ph as seen from the broadened absorption. Nevertheless, the aggregates morphology is still unaffected as the peak doesn't shift. Figure 2.12b shows the peak position as a function of temperature. We

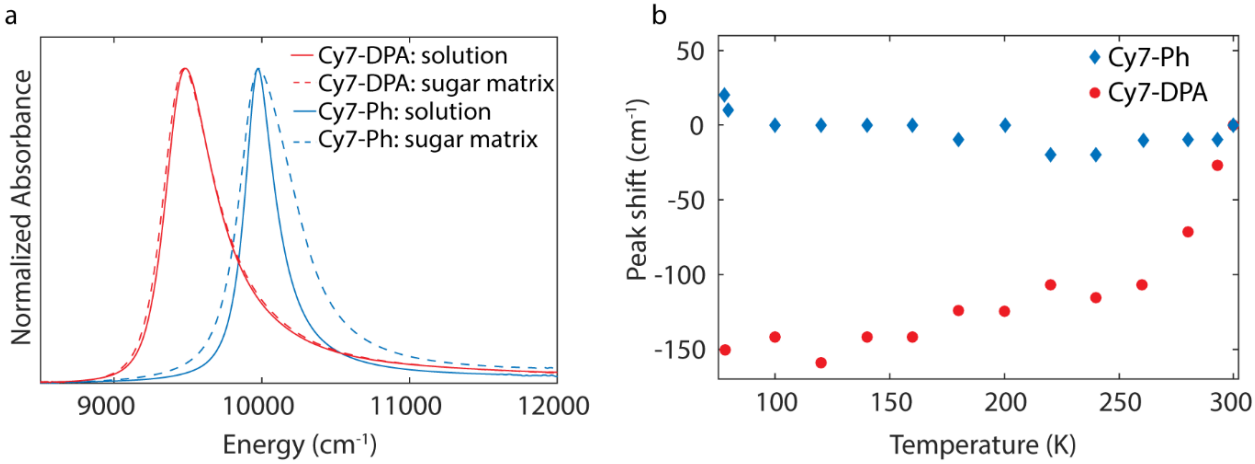

Figure 2.12. Solution and sugar matrix spectra comparison, peak shifts with temperature a. Absorption spectra of Cy7-DPA (red) and Cy7-Ph (blue) aggregates in solution (solid line) and sugar matrix (dashed lines); b. Peak shift as a function of temperature for Cy7-DPA (red circles) and Cy7-Ph (blue diamonds) with respect to the peak position at 300 K. Negative (positive) values indicate red (blue) shift.

observe a large red-shift for Cy7-DPA upon cooling, Cy7-Ph shows a slight blue-shift.

Effect of dimensionality on band structure

In Figure 2.13, we plot the eigenvalues of the Hamiltonian against the number of nodes in that eigenstate as a function of slip (each pair of sequential out-of-phase TDMs was considered a node). Disorder was not included in these calculations, nor were non-dipole-dipole forms of coupling (e.g. quadrupole or charge-transfer) and which can change the band-structure. The bright state always has zero nodes (k_x, k_y = 0). Here, we have assumed a finite size of the aggregate and the dielectric scaling factor (described in section 3.4). While the finite size of the aggregates will cause some redistribution of the oscillator strength around the bright state,[35,143] we observe the

phenomenon of I-aggregation in the 2D aggregate. In the 1D case shown in Figure 2.13a, the bright state is always on either side of the band-edge (highest or lowest eigenvalue) for slips. Contrastingly, in the 2D cases shown in Figure 2.13c-d, the bright state still maintains its zero node identity but it is not restricted to the band-edge depending on the slip value. This means that the dark states in I-aggregates may potentially couple to other transitions via near-field coupling.

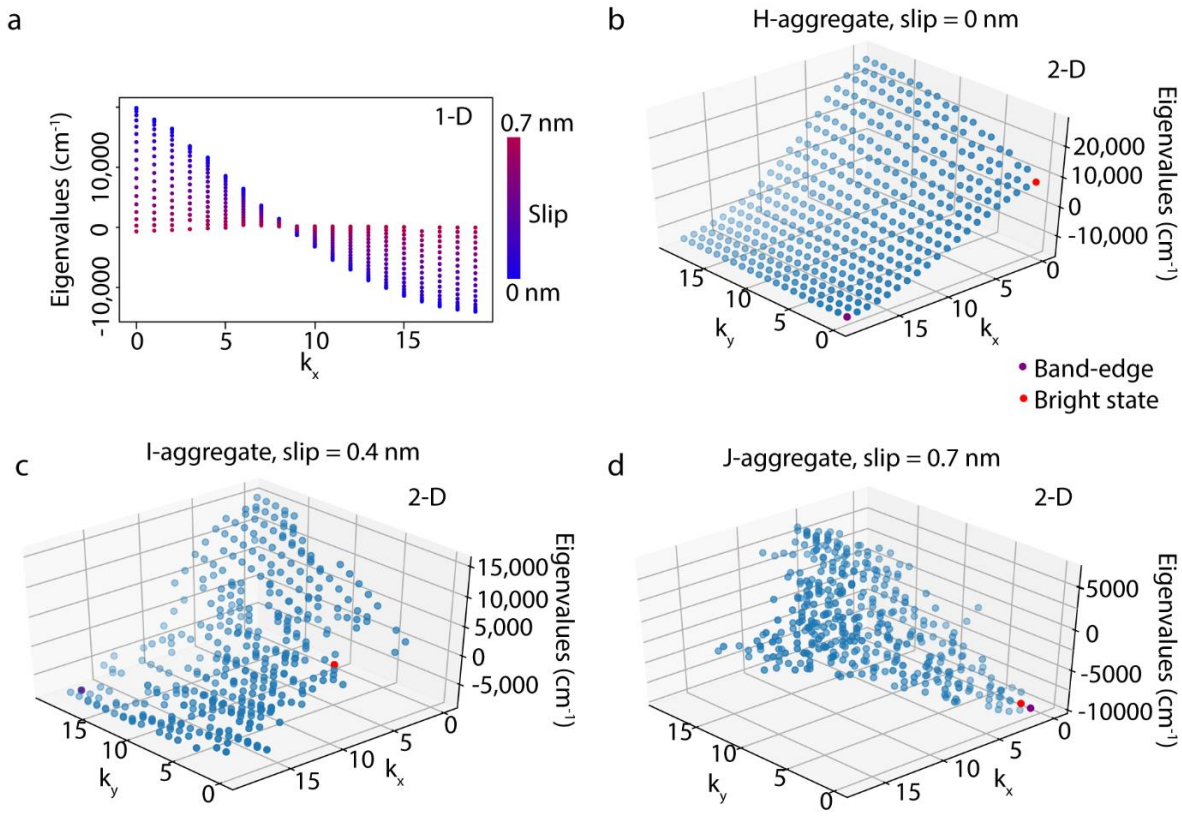

Figure 2.13. Representations of excitonic states in k-space

Eigenvalues of the aggregate Hamiltonian (with no disorder) as a function of number of nodes (k_x, k_y) for a. 1-D aggregate with increasing slip (blue = 0 nm, red=0.7 nm); b, c and d. 2-D aggregate with 0 nm, 0.4 nm and 0.7 nm slips respectively.

Estimating the extent of exciton delocalization

The number of sites an exciton is delocalized over can be calculated as the inverse participation ratio (I), which is the inverse sum of the scaling coefficients raised to the power of four (eq. 2.12a). We average I over many realizations of the Hamiltonian with varying disorder to estimate the extent of exciton delocalization. In Fig. S10, we show the inverse participation ratio I and linewidth W of the absorption spectra for a 20x28 aggregate with increasing site disorder. I is calculated and averaged over disorder realizations via

$$I_k = \sum_{l=1}^{n} \frac{1}{|c_{k,l}|^4} \tag{2.12a}$$

$$\mu_k = \left|\sum_{l=1}^{n} c_{k,l}\right|^2 \tag{2.12b}$$

$$I_{agg} = \frac{1}{n}\sum_{k=1}^{n} \mu_k * I_k \tag{2.12c}$$

$$\langle I_{agg} \rangle = \frac{1}{N}\sum_{l=1}^{N} I_{agg} \tag{2.12d}$$

The linewidth is calculated by assuming that the absorption spectra can be decomposed into individual eigenstates, each with a Lorentzian profile with width determined by the dephasing rate W_k as in Eq.(3.3):

$$A(\omega) = \sum_{k=1}^{n} \mu_k^2 \cdot \frac{W_k/2}{(\omega-\epsilon_k)^2+(W_k/2)^2} \tag{2.13}$$

We determine slip = 4.0 Å to be the best fit for the Cy7-Ph I-aggregate basing on the temperature-dependent absorption spectra. And the bath spectral density is fitted from the monomer absorption lineshape to an Ohmic bath with exponential cut-off.

$$D_b(E) = \pi\lambda \cdot \frac{\omega}{\omega_c} e^{-\omega/\omega_c} \tag{2.14}$$

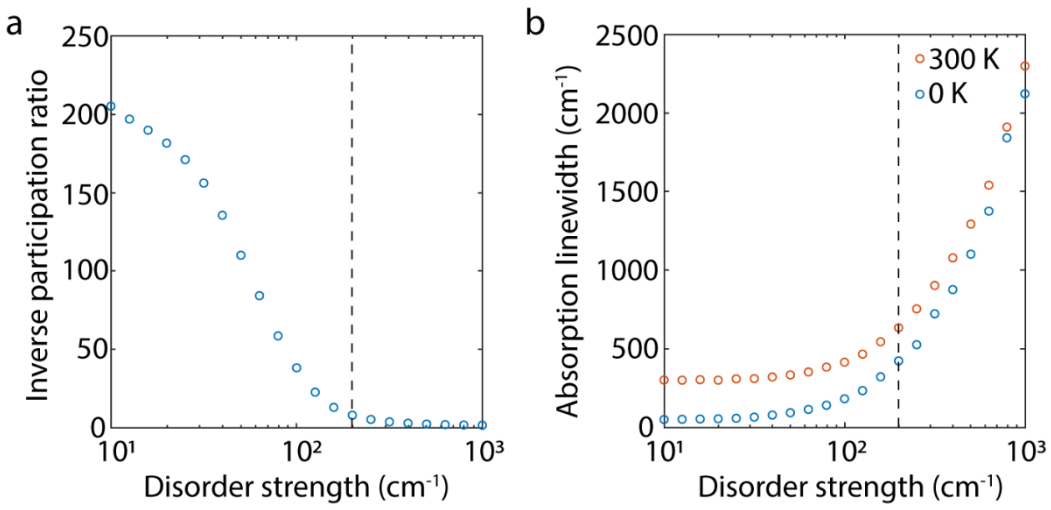

Figure 2.14. Estimating the extent of exciton delocalization

a. Inverse participation ratio (number of sites the exciton is delocalized over) and b. Linewidths for a 20x28 aggregate as a function of site disorder. Dotted lines indicate experimental linewidth.

where $\lambda = 600$ cm^{-1} and $\omega_c = 1000$ cm^{-1}.

As expected, I decreases and linewidth increases with increasing disorder. This set of parameters slightly underestimates the contribution from the temperature-independent homogeneous linewidth ($W_k^{(0)}$). We attribute the deviation to the inaccuracy of the extended dipole model for the short-range interactions among the dyes. We estimate that the excitons are delocalized over ~8 sites at room temperature.

Chapter 3

Thermodynamic Control of Molecular Aggregate Self-Assembly

In the previous chapter, we showed that aggregation provides a platform to tune the photophysical properties. However, a prerequisite for such tunability is the control of the aggregate self-assembly itself. In this chapter, we demonstrate thermodynamic control over the self-assembly of cyanine dyes into H- or J-aggregated morphologies and provide insights for stabilizing the extended 2D morphologies with red shifted absorptions.

3.1 Literature survey of aggregation routes

Excitonic molecular aggregates are non-covalently assembled arrays of chromophores wherein monomeric transition dipole moments (TDMs) couple to form extended Frenkel excitons upon excitation. These aggregates exhibit emergent photophysical properties, such as extreme changes in their absorption, emission and lifetimes which are tunable through aggregate topology, molecular arrangement and energetic disorder.[19,80,144] Large excitonic shifts afforded by long range TDM coupling make the aggregates extremely tunable across the broad spectral range from

visible (400-700 nm) through near and shortwave infrared (NIR: 700-1000 nm and SWIR: 1000-2000 nm respectively).[12,145] Therefore, cyanine aggregates have extensive applications ranging from model systems for photosynthetic energy transfer, NIR/SWIR imaging, non-linear optics and plexitonics.[88,146–148]

Table 3.1. Literature survey of aggregation strategies

Common aggregation strategies for benzothiazole cyanine dyes, examples of dyes from literature aggregated using the corresponding strategy. General structures of the dyes are shown in Chart 1. To simplify the diversity in structures, we group the dyes according to the length of cyanine bridge.

Aggregate preparation strategy	**Examples of common benzothiazole dyes aggregated**
Direct dissolution (in water, salt solution etc.)	Cy1,[23] Cy3,[53,123], THIATS,[149] Cy5,[114] Cy7[89]
Langmuir-Blodgett films	Cy1[150,151]
Adsorption on a surface	Cy1,[152] Cy3[41,153], THIATS[154]
Thin films	THIATS,[155,156] Cy3,[157,158] Cy7[46]
Crystallization on interface	Cy3[159]
DNA or polymer templating	Cy1,[160] Cy3,[161] Cy5,[161,162] Cy7[161]
Independent control of solvation conditions	Cy7[145] (Previous work)
	Cy3, Cy5, Cy7 (*This work*)

Understanding how these structures are stabilized and thereby controlling aggregate formation is a prerequisite to realizing potential technological and therapeutic applications. While many studies have elucidated the excitonic features of 2D and tubular cyanine aggregates and related it to their supramolecular structure,[25,77,163] little work has been done in understanding how these structures are stabilized. In Table 3.1, we summarize the diverse array of literature protocols used to prepare J-aggregates with the characteristic narrow red shifted absorption for various benzothiazole cyanine dyes (Figure 3.1). While this diversity is rationalized with each procedure carrying its advantages or disadvantages, it provides little rationale to approach the self-assembly of new chromophore aggregates. Here, we show that a general and straightforward approach based on independent control of solvation conditions allows us to directly tune the thermodynamics of self-

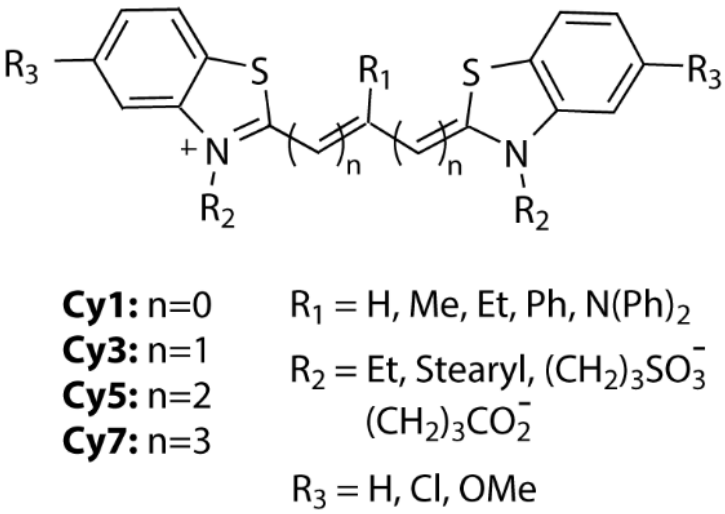

Figure 3.1. General structure of benzothiazole cyanine dyes

Sturctures of benzothiazole cyanine dyes aggregated using startegies listed in Table 3.1. Examples of common substituents are also listed.

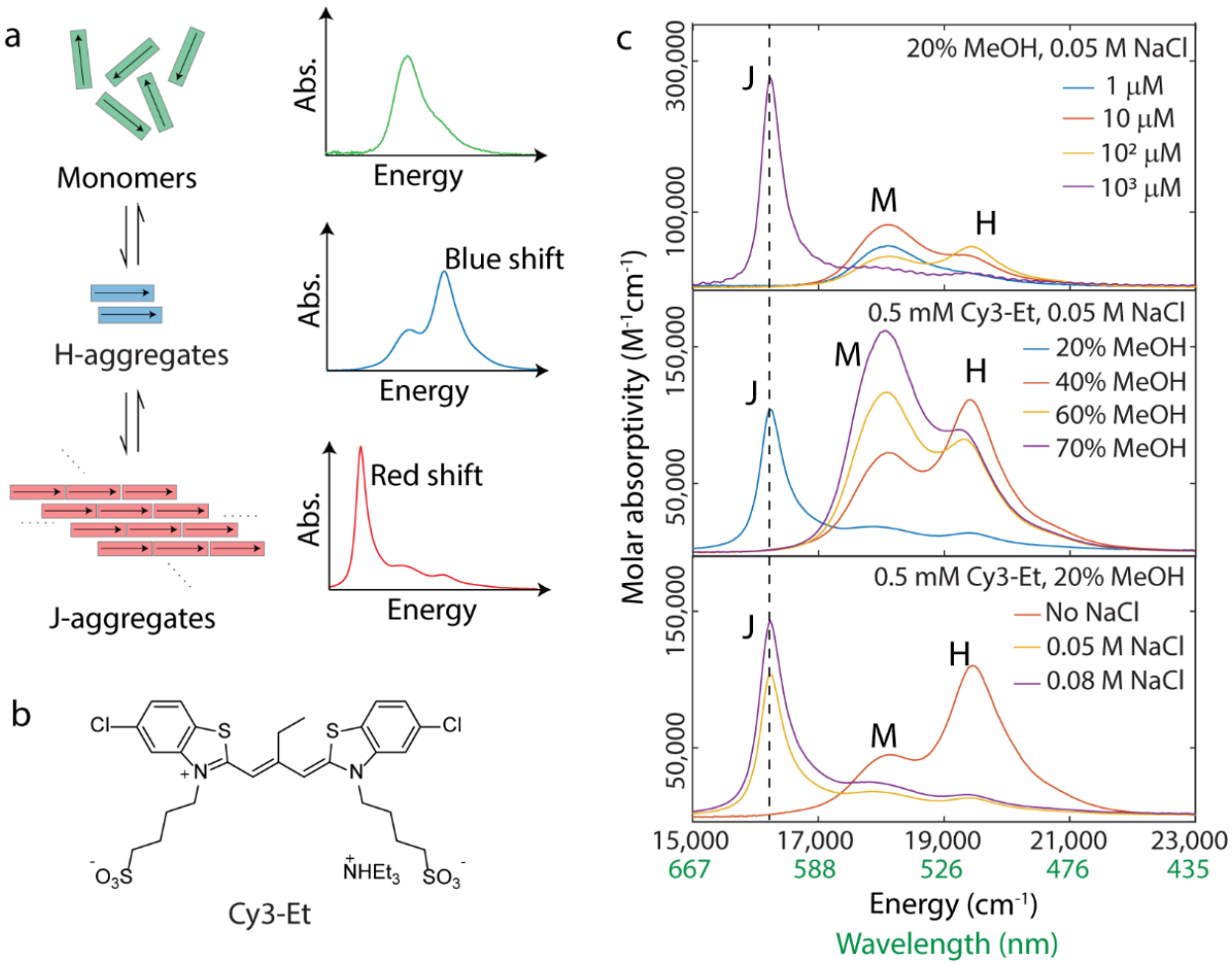

Figure 3.2. Schematic of aggregate equilibrium and independent control of solvation

a. Schematic showing the transformation of monomers to H-aggregates (dimers) to J-aggregates (extended monolayer sheets) and characteristic lineshapes of absorption spectra of the corresponding species in solution; b. Structure of the dye Cy3-Et; c. Absorption spectra taken ~ 24 hours after sample preparation where a predissolved monomer solution in methanol was injected into aqueous solution with or without NaCl while varying (top) dye concentration, (middle) v/v methanol:water ratio, and (bottom) salt concentration. In each case, rest of the two factors were kept constant.

assembly of cyanine aggregates in solution. A simple thermodynamic model allows us to construct a phase diagram for aggregation of cyanine dyes. Thermodynamic control of self-assembly allows us to selectively stabilize an aggregate morphology under flexible conditions (such as extremely

high or low dye concentrations), unlike previous methods which work under specific conditions. This makes the aggregates amenable towards a broader scope of experimental techniques, such as diffusion ordered spectroscopy (DOSY), and applications in devices.

3.2 Independent control of solvation

We focus on benzothiazole cyanine dyes that show a simple three component equilibrium between monomers, H-aggregates and J-aggregates which can be easily distinguished using their characteristic absorptions (Figure 3.2a). We use Cy3-Et (Figure 3.2b) as a model system, that is structurally close to the commonly studied THIATS.[155] Several strategies have been used to aggregate THIATS and similar dyes, summarized in the Table 3.1, including direct dissolution in water,[89] adsorption on silver halides,[41] and spin coating.[155] Here, we stabilize Cy3-Et aggregates under a variety of conditions by independent control of different solvation conditions. While salt addition and solvent/non-solvent mixtures are extensively used, our systematic implementation avails tunable range of conditions to stabilize a particular structure. We make a monomer solution in methanol and disperse it into water (with or without NaCl), a more generalized modification of the well-known 'alcoholic route'.[164] We use these parameters to access the aggregation phase space, and plot the resulting absorption spectra in Figure 3.2c.

We vary *(i)* final dye concentration (top panel); *(ii)* solvent/non-solvent ratio (middle panel); and *(iii)* ionic strength by adding salt (bottom panel) keeping the other two factors constant. Unsurprisingly, we find that higher dye concentrations favor H-aggregation followed by J-aggregation. In addition, high % MeOH (~ 70%) and low dye concentrations always favor monomeric state. As we decrease the % MeOH or increase the salt concentration, we observe gradual transformation of monomers to H-aggregate and finally to J-aggregate. Our results are

consistent with the hypothesis that ionic strength induced dielectric screening and hydrophobic interactions (lower % MeOH) stabilize extended aggregates.[165] Moreover, this far simpler and easily generalizable approach yields the similar narrow red shifted absorption lineshapes for J-aggregates, as seen in previous methods (Table 3.1), indicating that we are able to access the similar J-aggregate microstructures that lead to this characteristic lineshape with higher degree of control.

Characterization of H- and J-aggregate structures: The use of different solvation conditions to stabilize a desired H- or J-state allows us to develop preparations that are amenable to characterization tools requiring high concentrations of a single species. For example, smaller aggregate species like dimers and oligomers are too small for characterization tools such as cryo-electron microscopy (cryoEM) or atomic force microscopy (AFM). Multidimensional NMR methods such as diffusion ordered spectroscopy (DOSY) typically require very high concentrations where fully aggregated species tend to be more dominant than smaller aggregates. Using the methods outlined above, we were able to perform DOSY on H-aggregates, stabilizing the H-aggregate at a concentration of 1 mM by retaining a low volume fraction of deuterated methanol (10:90 MeOD:D_2O, no NaCl). In Figure 3.3a, all the peaks corresponding to the aggregate emerge at a single diffusion constant 1.32 x 10^{-10} m^2/s while faster diffusing species such as counter ions and solvent show up at higher diffusion constants. A comparison with the DOSY spectrum of the monomer, in Figure 3.6, shows the H-aggregate is about twice the size of the monomer (Table 3.2). We thus conclude that the H-aggregate is a dimer consistent with previous concentration dependent absorption studies.[123,166] For the redshifted J-aggregates, we perform CryoEM and AFM. CryoEM demonstrates extended rectilinear sheets with average dimensions of 500-1000 nm by several microns. AFM height analysis (Figure 3.3c) confirms

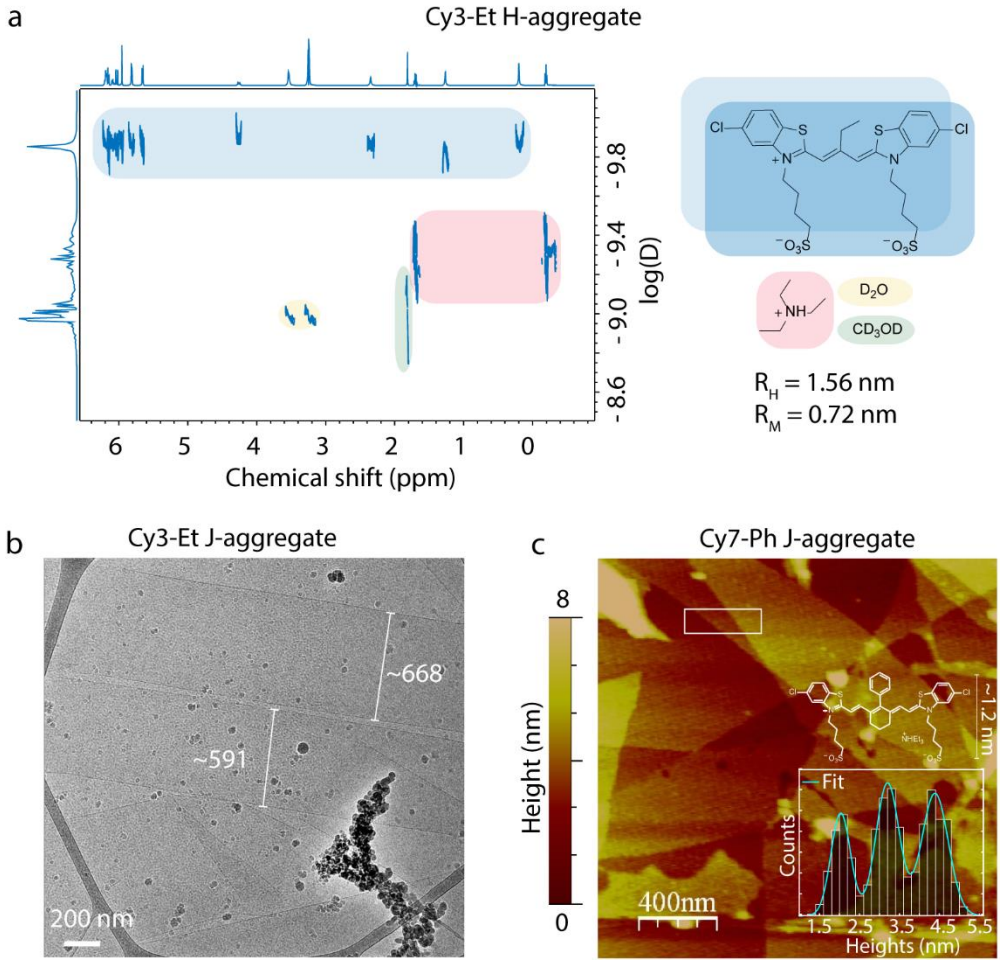

Figure 3.3. Characterizations of H-aggregated oligomers and extended J-aggregates.

a. 1H diffusion ordered spectroscopy (DOSY) of Cy3-Et H-aggregates at 1 mM concentration prepared in 90% D2O and 10% MeOD. Comparing hydrodynamic radius with monomer suggests a dimer morphology; b. Cryo-electron microscopy image of vitrified Cy3-Et J-aggregate depicting sheet-like morphology. Numbers indicate sheet widths in nanometers; c. Atomic force microscopy image of Cy7-Ph J-aggregates with a histogram of the heights (bottom inset) enclosed in the white rectangle. The histogram is fit to a sum of three gaussians (cyan line) with R^2 = 0.9695. Height of a single layer obtained from the histogram matches the height of a single molecule (top inset) indicating monolayer sheets.

monolayer structures with molecular plane perpendicular to the plane of the sheet (section 3.7). We do not observe any conversion to nanotubes over a week for Cy7-Ph J-aggregates (Figure 3.8).

H-aggregates occasionally show a slow conversion to J-aggregates over long times which may be due to solvent evaporation. As this conversion is very slow, we treat it as a quasi-equilibrium state.

3.3 Thermodynamics of aggregation: three-component equilibrium model

We construct a thermodynamic model that describes the energetic landscape governing self-assembly of dimerized H-aggregates and sheet-like J-aggregates. Based on the observations in Figure 3.2c, we consider two general equilibria as follows.

$$n_1 M \rightleftharpoons H \tag{3.1}$$

$$n_2 H \rightleftharpoons J \tag{3.2}$$

M, H, and J denote the monomer, H-aggregate and J-aggregate species respectively. n_1 denotes the number of monomers in an H-aggregate and $n_1 \cdot n_2$ is the total number of monomers in the J-aggregate. We use the subscripts 1 and 2 for the equilibrium constants (K_{eq}) and standard Gibbs free energies (ΔG°) of equilibria (3.1) and (3.2) respectively. The respective equilibrium constants can be written as

$$K_1 = \frac{C_H}{C_M^{n_1}}; K_2 = \frac{C_J}{C_H^{n_2}} \tag{3.3, 3.4}$$

The total concentration, C_{tot} is defined as

$$C_{tot} = C_M + n_1 \cdot C_H + n_1 \cdot n_2 \cdot C_J \tag{3.5}$$

where C_M, C_H and C_J denote the concentrations of monomer, H-aggregate and J-aggregate respectively. Upon substitution and rearrangement (complete derivation in Section 3.7), we arrive at the characteristic polynomial of C_M with respect to total concentration, equilibrium constants and aggregate size.

$$n_1 \cdot n_2 \cdot K_2 \cdot K_1^{n_2} \cdot C_M^{n_1 \cdot n_2} + n_1 \cdot K_1 \cdot C_M^{n_1} + C_M - C_{tot} = 0 \qquad (3.6)$$

This high order polynomial will always have exactly one real positive root (proof in Section 3.7), which allows us to use standard root finding methods to find C_M for a given set of parameters. Mole fractions of each species (χ_M, χ_H and χ_J) can be calculated for any combination of ΔG° using equations (3-5). *Thus, we can uniquely define the equilibrium composition of the solution for any combination of standard Gibbs free energies.* This characteristic polynomial is independent of the choice of pathway (Section 3.7).

In Figure 3.4a-c, we map the ternary equilibrium composition as we change the standard Gibbs free energies of H-dimerization on the x-axis and extended 2D J-aggregate formation on the y-axis. We note that these Gibbs free energies are not truly independent as our experimental parameters may affect both. We set $n_1 = 2$ based on our DOSY results (Figure 3.3a) and $n_2 = 10$ representing total aggregation number of 20 in extended J-aggregates. While this number greatly underestimates the number of J-aggregated monomers, it captures the sharp onset of J-aggregation

as a function of concentration. Each point on these maps represents a different equilibrium condition for a fixed

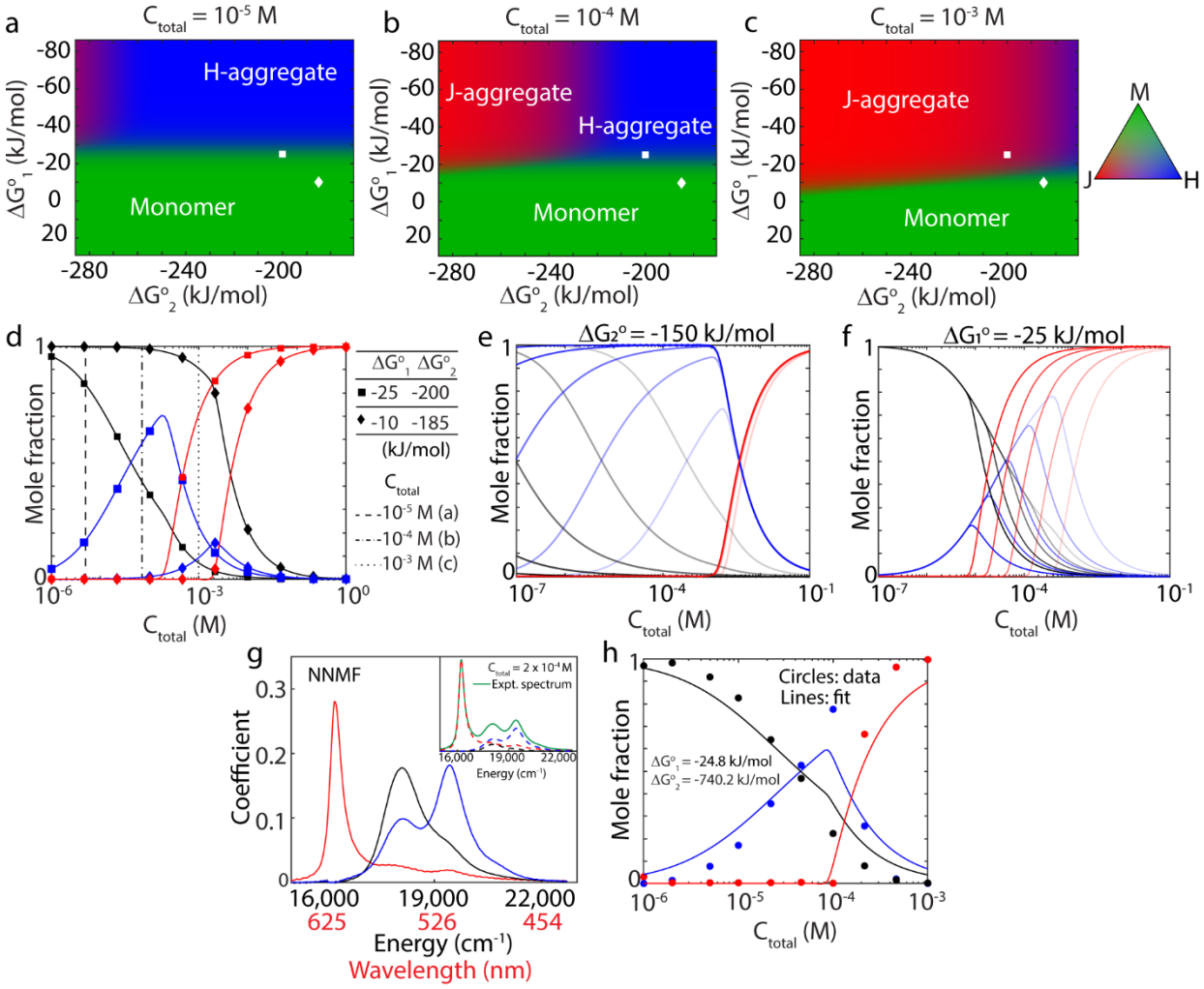

Figure 3.4. Results from the three component equilibrium model, non-negative matrix factorization (NNMF), and fitting model to the experimental data

Prediction of equilibrium composition using the three component model. a-c. Maps showing the variation of equilibrium composition as a function of standard Gibbs free energies of monomer to H-aggregate equilibrium (ΔG_1°) and H-aggregate to J-aggregate (ΔG_2°) for different total dye concentrations (C_{total}), $n_1 = 2$, $n_2 = 10$, a. $C_{total} = 10^{-5}\,M$; b. $C_{total} = 10^{-4}\,M$; and c. $C_{total} = 10^{-3}\,M$. The color of each pixel denotes the composition shown in the ternary plot on

the right with RGB value corresponding to mole fractions of J-aggregate, monomer and H-aggregate respectively; d-f. Evolution of mole fractions of monomer (black), H-aggregate (blue) and J-aggregate (red) with total dye concentration for - d. two points on the ΔG^o maps denoted by square ($\Delta G_1^\circ = -25$, $\Delta G_2^\circ = -200$ kJ/mol) and diamond ($\Delta G_1^\circ = -10$, $\Delta G_2^\circ = -185$ kJ/mol), three vertical lines correspond to the C_{total} values in a-c; e. varying ΔG_1° from -60 kJ/mol (darkest) to -20 kJ/mol (lightest) and $\Delta G_2^\circ = -150$ kJ/mol; f. varying ΔG_2° from -300 kJ/mol (darkest) to -180 kJ/mol (lightest) and $\Delta G_1^\circ = -25$ kJ/mol; g. Basis vectors obtained from non-negative matrix factorization (NNMF) of experimental concentration dependence data (Figure 3.10); (Inset) example of an experimental spectrum (green) with the decomposition into three NNMF vectors (dashed lines) corresponding to monomer (black), H-aggregate (blue), and J-aggregate (red); h. Experimental mole fractions obtained from NNMF (circles) and the fitted mole fraction curves from the three component model (lines).

concentration. Given a set of experimental ΔG^o's for any system, our model predicts the equilibrium composition at any concentration (Figures 3.4a-c). Changing solvation conditions such as % MeOH or salt concentration which directly affect ΔG_1° and ΔG_2°, spans this phase space, as might adding substituents to the chromophore. Direct transition from H-aggregate to J-aggregate involves a change in ΔG_2° (corresponding to extended aggregate formation). This suggests that increasing the ionic strength at low % MeOH (Figure 3.2c) mostly changes ΔG_2°. At highly negative ΔG_2°, we observe a direct transition from monomer to J-aggregate upon reducing ΔG_1°.

We pick two fixed points on the maps in Figures 3.4a-c corresponding to $\Delta G_1^\circ = -25$, $\Delta G_2^\circ = -200$ kJ/mol (square), and $\Delta G_1^\circ = -10$, $\Delta G_2^\circ = -185$ kJ/mol (diamond) and plot them with other total chromophore concentrations in Figure 3.4d. In all the cases, J-aggregates require a certain threshold concentration where we observe a sharp increase or 'turn-on' in the J-aggregate mole fraction. This non-sigmoidal nature of J-aggregate mole fraction curves is indicative of a cooperative mechanism and enables the formation of large aggregates.[165] Figure 3.9 shows mole

fractions as a function of n_2 which depicts the delayed and sharper turn-on in J-aggregation as a function of aggregate size. As increasing ionic strength transitions from H- to J-aggregate, we hypothesize that it primarily affects ΔG_2° due to additional charge screening. Figures 3.4e-f demonstrate that ΔG_1^o does not affect the J-aggregate onset but ΔG_2^o changes are coincident with a sharp decrease in monomer and H-aggregate.

This sharp turn-on in J-aggregate is a clear indication of cooperative self-assembly akin to a phase transition or reaching a critical micelle concentration.[167,168] We attribute the cooperativity to the 2-dimensional nature of sheet-like aggregates -- the number of potential molecular contacts increases linearly with the aggregate size.[167] Unlike traditional 1D aggregates, cooperative assembly can be achieved without invoking a change in chemical potential for every additional monomer.[165] Due to additional contacts in 2D aggregates, we require more charge screening as evident from our experiment (Figure 3.2c) where 2D aggregates are stabilized by adding salt. Our results suggest that many systems can be aggregated into 2D brick-layer sheets simply by stabilizing ΔG_2° relative to ΔG_1°, for example, through control of solvent to non-solvent ratio or by adding salt.

In order to show quantitative agreement between our model and experiment, we perform a concentration dependence of Cy3-Et at 20% MeOH and 0.05 M NaCl (Figure 3.10). Since there are three overlapping spectra, we decompose our observed spectra into J, H, and M spectra via non-negative matrix factorization (NNMF, Section 3.7).[169] We obtain three basis vectors (Figure 3.4g, example decomposition shown in inset), which are consistent with experimental spectra of the monomer, and published spectra for dimer H-aggregates and J-aggregates.[123] We plot the mole fractions obtained from NNMF for this concentration series in Figure 3.4h (circles), capturing the

sharp increase in the J-aggregate at 10^{-4} M. Finally, we fit the mole fraction data for all three components simultaneously to arrive at Gibbs free energies of $\Delta G_1^\circ = -24.8, \Delta G_2^\circ = -740.2$ kJ/mol (Section 3.7). This ΔG_1° value is very close to previously reported dimerization energy for THIATS.[123] The highly negative ΔG_2°, indicating the strong favorability of extended 2D aggregate formation, is ascribed to the increased number of interactions in 2D aggregates.[168]

3.4 Library of 2D aggregates from visible through shortwave infrared

We demonstrate that principles for self-assembly used here are truly generalizable and are also extendable to other families of cyanine dyes such as benzimidazole cyanines. Figure 3.5 shows a list of cyanine dyes that form 2D sheet-like aggregates with tunable absorption from visible through SWIR. In all these cases, the aggregation behavior followed similar trends where lower % MeOH (20 - 30%) gave the extended J-aggregated sheets, the optimal salt and dye concentrations differ slightly among individual dyes. With the exceptions of TDBC and Cy7-DPA, we also observe similar H-aggregate peak at 50% MeOH. Particularly, larger dye molecules like Cy7-DPA and Cy7-Ph aggregate readily without any need for salt where as Cy3-Et and Cy5-Ph need slightly higher dye concentrations with added salt, suggesting that higher surface areas lead to stronger van der Waals interactions. A particular example of the well-known benzimidazole cyanine dye, TDBC is shown in Figure 3.5a. TDBC is also known to form sheet aggregates that have garnered interest in excitonic energy transfer and plexitonics.[148] We show the principles outlined above can also be used to tune the self-assembly of TDBC into sheet like J-aggregates (Figure 3.11). TDBC and Cy7-DPA do not go through an H-aggregate state likely due the ethyl

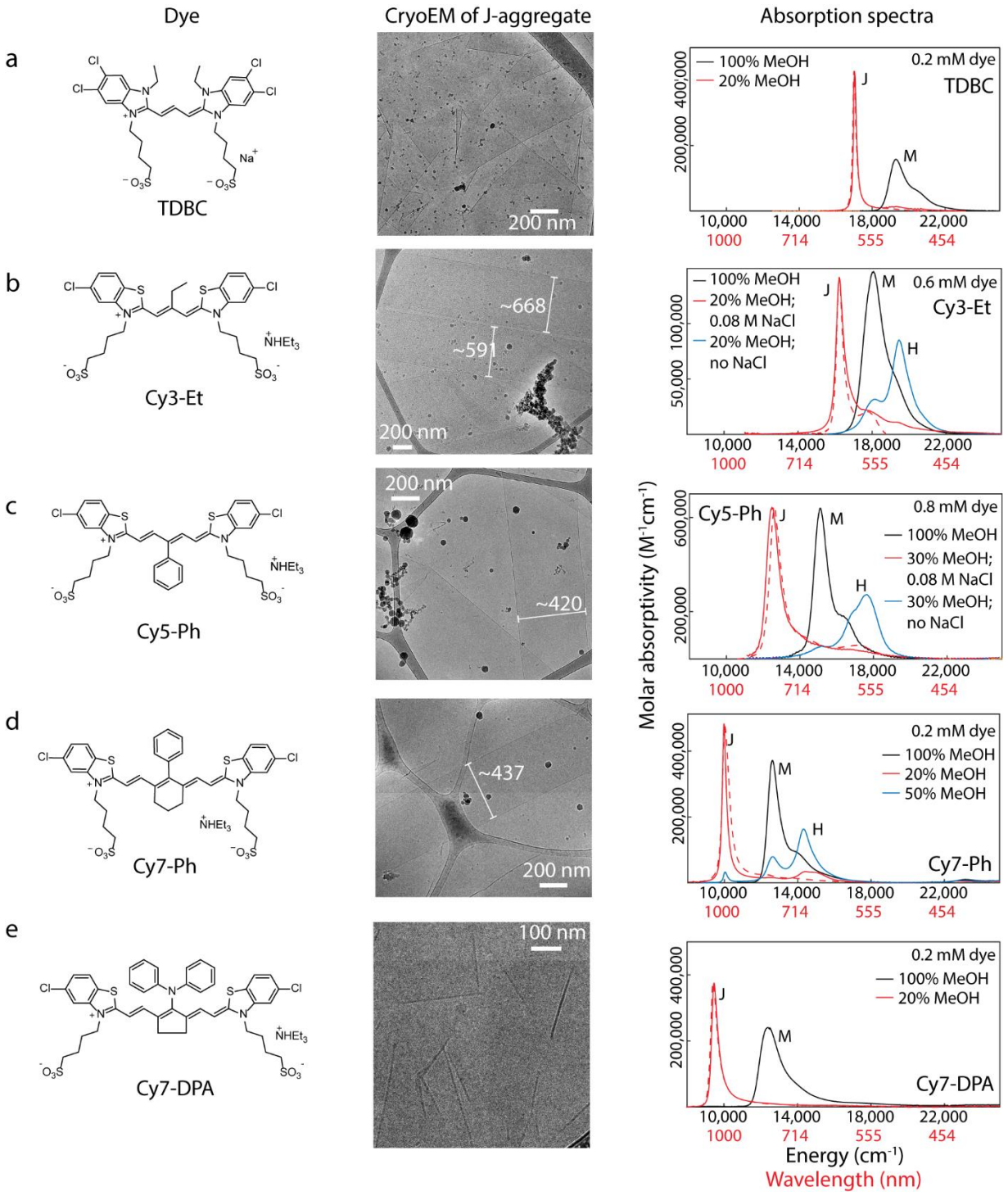

Figure 3.5. 2D aggregates with absorption tunability from visible through shortwave infrared

(left) dye structures; (center) cryo-electron microscopy image of the 2D sheet aggregates and (right) absorption spectra of monomer (black), H-aggregates (blue), red shifted 2D aggregates (red,

solid line), and sugar matrix stabilized 2D aggregates (red, dashed line). Numbers on cryoEM images indicate sheet widths in nanometers. Absorption spectra of sugar matrix samples are arbitrarily scaled to compare the lineshapes with solution spectra.

groups (in case of TDBC) and the bulky diphenylamine group (in case of Cy7-DPA) that might sterically hinder cofacial stacking. Furthermore, we show that all the 2D aggregates in Figure 3.5 can be stabilized in a sugar matrix (dashed lines) which is known to protect the aggregates against photo and air damage,[117] preserving the characteristic excitonic features while facilitating cryogenic and high excitation flux spectroscopies on the aggregates.

3.5 Conclusions

We conclude that aggregation strategy based on independently controlling the solvent to non-solvent ratio, salt or dye concentration provides a general and tunable avenue for selectively stabilizing an aggregate morphology for the broad class of cyanine dyes. Our approach avails a broad range of aggregation conditions to stabilize a desired morphology, which in turn, controls the excitonic properties. In addition, tunability over a vast aggregation space enables new structural characterization techniques such as DOSY and broadens the application space. For example, aggregating at lower concentrations through lower non-solvent ratio can be used to control the optical density of aggregate antennas in thin films.

We explain the conserved aggregation trends on the basis of a simple three component equilibrium model and gain insights into the thermodynamics of the self-assembly process. Our results show that ionic strength mainly effects ΔG_2°, enabling direct transition from dimer H-aggregates to extended J-aggregates at the same dye concentration and solvent composition, likely by stabilizing larger charged structures. Solvent to non-solvent ratio, on the other hand, likely

affects both ΔG_1° and ΔG_2° as it can induce both H- and J-aggregation depending on the available dye concentration. NNMF untangles the constituent spectra and shows we can achieve excellent agreement between model and experiment. Finally, we show that solvation control can be extended to several sheet forming cyanine dyes thus enabling a tunable library with absorptions ranging from visible through SWIR.

Kinetics and thermodynamics of aggregation of chromophores is a topic of extensive research, mostly focused on 1D π-stacking structures of porphyrins and perylene bisimides.[165,170,171] However, extended 2D aggregates have unique features not reproduced in linear aggregates. The number of pair-wise interactions between an aggregate and a monomer is proportional to the aggregate size in the 2D case, whereas it is a constant for linear aggregates. In analogy to bilayer formation in surfactants, one observes a near phase transition above a set concentration of dye in 2D aggregates.[168] In linear aggregates with pairwise interactions, phase transitions are rigorously forbidden.[168] Despite the rich excitonic properties and diverse applications of cyanine dye aggregates, application of the thermodynamic self-assembly principles to the broad class of cyanine dyes aggregates is unprecedented. Overall, 2D aggregation provides a unique platform for even more stable structures at lower concentrations while retaining the excitonic features of J-aggregates and the broad class of cyanine dyes is an excellent avenue for this. The simple and broadly applicable principles for aggregation presented here provide the first step toward realizing many potential applications of molecular aggregates.

3.6 Experimental section

Materials: All dyes were obtained from FEW chemicals GmbH (catalogue # S0046, S2278, S2284, S2433 and S0837 for TDBC, Cy3-Et, Cy5-Ph, Cy7-Ph and Cy7-DPA respectively).

Sodium chloride, sucrose, D-(+)-trehalose and methanol were obtained from ThermoFisher Scientific. Milli-Q water (18 MΩ) was used for making all aggregate samples. All materials were used as obtained, without any further purification.

Preparation and absorption of aggregate solutions: Appropriate amounts of the dyes were weighed and dissolved in methanol to make monomer stock solutions, then diluted in methanol to make a series of monomer solutions of appropriate concentrations. Each diluted monomer solution was injected into water or aqueous NaCl with a specified mixing ratio. The concentration of the diluted monomer solution was decided such that the final concentration after water/ aq. NaCl injection is held constant. The calculations for this process were streamlined in a MATLAB code (available upon request). Glass vials used to store the samples were pre-soaked in Milli-Q water and aggregate solutions were allowed to equilibrate in dark for 24 h prior to measurement. Absorption measurements were taken on Agilent Cary 60 spectrometer for visible/NIR samples. SWIR absorption spectra were taken on JASCO V-770 UV/Vis/NIR spectrometer. Starna Cells quartz cuvettes of path lengths 0.01 mm, 0.2 mm or 1 mm were used depending on the dye concentration.

Cryo-electron microscopy (CryoEM): Samples were prepared on mesh 200 lacey formvar/carbon copper grids obtained from Ted Pella Inc. The grids were plasma-cleaned under a H_2/O_2 gas flow using a Solarus Gatan Plasma cleaner for hydrophilization. Vitrobot Mark IV was used for plunge-freezing the samples. 5 μL of the aggregate solution was dropped onto the grid, and excess solution was removed by blotting for 3.0 s with standard blotting paper from Ted Pella and immediately dropped into liquid ethane. The frozen grids were stored in liquid nitrogen. Grids were loaded on to a liquid nitrogen cooled Gatan 626 cryo-transfer sample holder, then inserted

into the microscope. CryoEM images were recorded on a FEI TF20 electron microscope equipped with a field-emission gun at 200 keV and CCD camera.

Atomic force microscopy (AFM): Films for AFM were prepared according to a previously reported drop-flow technique with some modifications.[164] Aggregate solutions (2-3 drops) were dropped on a freshly cleaved mica substrate (1 cm diameter) kept at a small incline. Mica substrates were obtained from ThermoFisher Scientific. The solutions were allowed to slowly air dry on the bench while covered with a box to shield from room light and air currents. AFM measurements were done on Veeco Bioscope II AFM with tapping mode Al coated AFM tips obtained from NanoAndMore USA Corp. with 42 N/m force constant and a resonant frequency of ~320 kHz.

Diffusion ordered spectroscopy (DOSY) NMR: NMR spectra were taken at room temperature on a Bruker Avance 500 MHz spectrometer with a 5 mm broadband probe and processed using TopSpin 4.07. After finding sufficient values for gradient pulse length (p30, δ) and diffusion time (d20, Δ) to yield spectra with 95 and 5% of original signal, 32 spectra were taken on a linear ramp and processed through TopSpin for diffusion constants.

Sugar matrix stabilization: Prepared solutions of 2D aggregates after the 24 h equilibration step were mixed with a saturated sugar solution made by dissolving a 50:50 sucrose/trehalose (w/w) in distilled water. 100 μL aggregate solution was taken in a vial pre-soaked in Milli-Q water. To this, 100 μL of the sugar solution was added drop-wise and gently mixed. The sugar-aggregate mixture was dropped onto a 0.2 mm quartz cuvette from Starna Cells Inc. and kept under vacuum in dark for 24 h for drying.

3.7 Supporting information

This section covers the following additional information:

Comparison of monomer – H-aggregate DOSY spectra and calculation of hydrodynamic radii, wide view AFM of Cy7-Ph, description of AFM height analysis, aggregate spectra over long time, derivation of the characteristic polynomial, effect of aggregation number of the mole fractions, detailed explanation of NNMF, details of the fitting the model to experimental mole fractions, concentration and % MeOH screens for TDBC aggregates.

Diffusion ordered spectroscopy (DOSY)

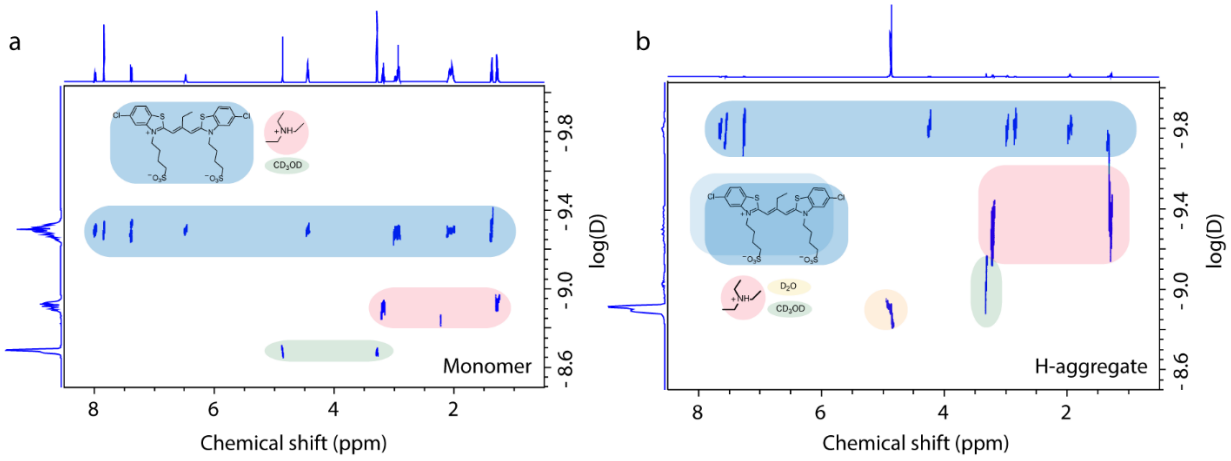

Figure 3.6. Comparison of DOSY spectra of monomer and H-aggregate of Cy3-Et
a. Cy3-Et monomer (5 mM) in CD_3OD and b. Cy3-Et H-aggregate (1 mM) in 10% CD_3OD/D_2O (v/v).

Figure 3.6 shows the DOSY spectrum of Cy3-Et monomer. Similar to the H-aggregates DOSY (also shown in Figure 3.6b on same scale as the monomer for comparison), all the protons from the dye molecules show up at a unique diffusion constant. We use Stokes-Einstein relationship to estimate the size from the diffusion constant. For viscosity of solvent the mixture, a weighted

average of the known viscosities for D_2O and CD_3OD was used. The hydrodynamic radii and other calculation parameters, given in Table 3.2, show that the H-aggregate is roughly twice the size of the monomer.

Table 3.2. Diffusion ordered spectroscopy (DOSY) data of Cy3-Et

Diffusion coefficients obtained from DOSY and parameters used to calculate the hydrodynamic radii of Cy3-Et monomers and H-aggregates from Stokes-Einstein relation.

Sample	**Diffusion Coefficient (m^2s^{-1})**	**Solvent**	**Viscosity ($kgm^{-1}s^{-1}$)**	**Hydrodynamic Radius (nm)**
H-aggregate (1 mM)	1.32×10^{-10}	10% CD_3OD/D_2O	1.05×10^{-3}	1.56
Monomer (5 mM)	4.96×10^{-10}	100% CD_3OD	6.0×10^{-4}	0.72

Atomic Force Microscopy of J-aggregate

We use AFM analysis to probe the height of 2D sheets and their layer structure. As Cy3-Et J-aggregate solutions require added salt, complicating height analysis, Cy7-Ph J-aggregates (prepared without salt at 20% MeOH, 0.2 mM dye as described in our prior work) were analyzed.[145] AFM images of Cy7-Ph (Figure 3.3c) are fit to the difference in heights between adjacent layers.[164,172] We plot a histogram of the heights of a selected region (Figure 3.3c bottom inset) and fit to a sum of 3 Gaussians, $y = \Sigma_{i=1}^{3} a_i \cdot e^{-\left(\frac{x-b_i}{c_i}\right)^2}$ where a_i, and b_i respectively are the amplitudes, center positions of the Gaussians and c_i are related to width. The height of a single sheet was calculated from the difference in the center positions of adjacent peaks ($b_{i+1} - b_i$), and

is 1.18 ± 0.01 nm, which matches the height of a Cy7-Ph molecule ~1.2 nm (Figure 3.3c, top inset). Thus, we conclude that the sheets are monolayers with the molecular plane perpendicular to the plane of the sheets. Since we do not observe significant differences in spectral lineshapes or

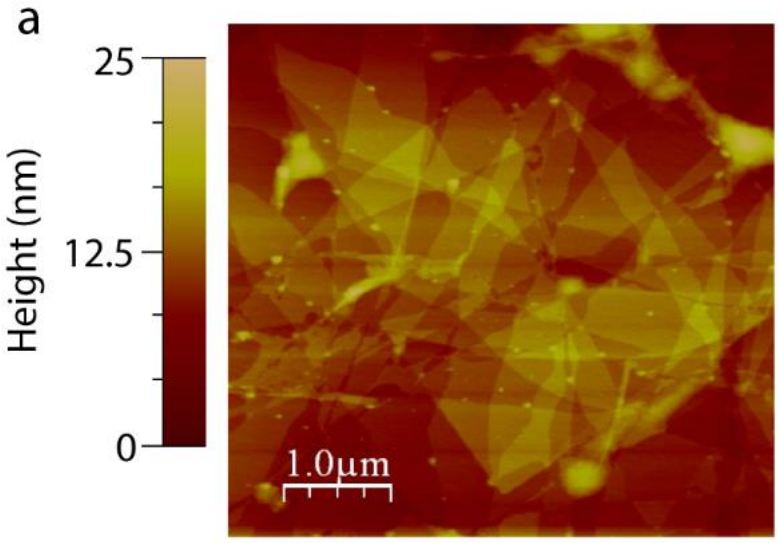

Figure 3.7. Wide view AFM image of Cy7-Ph 2D aggregate

AFM image of a drop casted film of Cy7-Ph on freshly cleaved mica with a wider view showing sheet morphology. Height analysis confirms the sheets are monolayers.

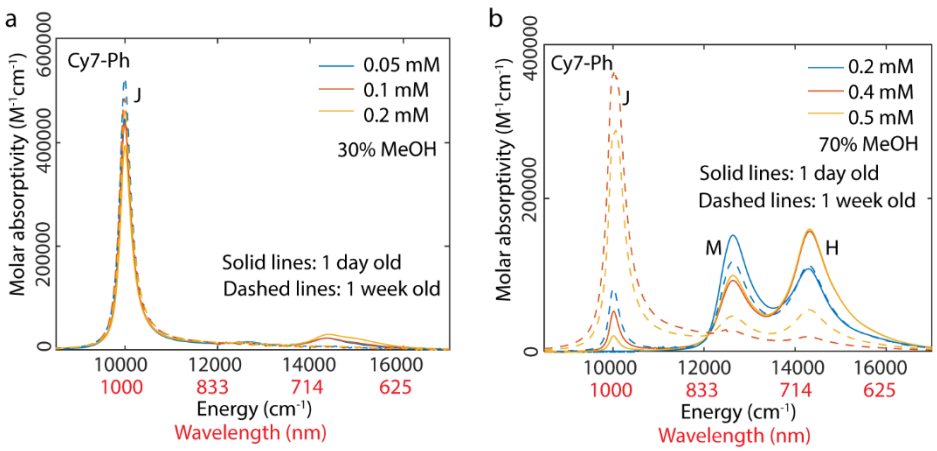

Figure 3.8. Aggregate spectra over long time

Absorption spectra of Cy7-Ph aggregates; a. 30% MeOH, b. 70% MeOH at different concentrations taken 24 h after sample preparation (solid lines) and after 1 week of sample preparation (dashed lines).

electron microscope images for different dyes studied here, we hypothesize that this aggregate morphology applies to all J-aggregates studied.

Characteristic Polynomial Derivation

We model the equilibrium between the monomer, H-aggregate and J-aggregate using the following equations:

$$n_1 M \rightleftharpoons H \qquad (3.7)$$

$$n_2 H \rightleftharpoons J \qquad (3.8)$$

where M, H, and J denote the monomer, H-aggregate and J-aggregate respectively. n_1 denotes the number of monomers in an H-aggregate and $n_1 \cdot n_2$ is the total number of monomers in the J-aggregate. Initially, the monomers assemble into an H-aggregate, which is a dimer. When the total

number of monomers reach a certain limit, they assemble into a large J-aggregate, which is a 2D sheet in all the cases discussed here. This assumption is justified by our experimental observations where we see an H-aggregate peak rising initially, which then goes down with a sudden increase in the J-aggregate peak. The equilibrium constant is related to standard Gibbs free energy by $\Delta G^o = -RTln(K)$, where R, T and K are the universal gas constant, standard temperature and equilibrium constant respectively.

Let K_1 and K_2 denote the equilibrium constants for equations (3.7) and (3.8) respectively. Therefore,

$$K_1 = \frac{C_H}{C_M^{n_1}} \tag{3.9}$$

$$K_2 = \frac{C_J}{C_H^{n_2}} \tag{3.10}$$

$$C_H = K_1 \cdot C_M^{n_1} \tag{3.11}$$

Substituting eq. (3.9) into eq. (3.10) and rearranging eq. (3.10),

$$C_J = K_2 \cdot \left(K_1 \cdot C_M^{n_1}\right)^{n_2} = K_1^{n_2} \cdot K_2 \cdot C_M^{n_1 \cdot n_2} \tag{3.12}$$

Further, if C_{tot} is the total dye concentration in the solution,

$$C_{tot} = C_M + n_1 \cdot C_H + n_1 \cdot n_2 \cdot C_J \tag{3.13}$$

Substituting eq. (3.9) for C_H and eq. (3.12) for C_J into eq. (3.12),

$$n_1 \cdot n_2 \cdot K_2 \cdot K_1^{n_2} \cdot C_M^{n_1 \cdot n_2} + n_1 \cdot K_1 \cdot C_M^{n_1} + C_M - C_{tot} = 0 \qquad (3.14)$$

or

$$n_1 \cdot n_2 \cdot e^{-\Delta G_2^o/RT} \cdot e^{-n_2 \cdot \Delta G_1^o/RT} \cdot C_M^{n_1 \cdot n_2} + n_1 \cdot e^{-\Delta G_1^o/RT} \cdot C_M^{n_1} + C_M - C_{tot} = 0$$

Eq. (3.14) can be solved analytically for C_M for a known value of C_{tot}. C_H and C_J were obtained using eq. (3.9) and eq. (2.12) respectively. We get the mole fractions (χ) of each component using following equations.

$$\chi_M = C_M / C_{tot} \qquad (3.15a)$$

$$\chi_H = (n_1 \cdot C_H) / C_{tot} \qquad (3.15b)$$

$$\chi_J = \left(n_1 \cdot n_2 \cdot C_J\right) / C_{tot} \qquad (3.15c)$$

All mole fraction curves are calculated by solving the above polynomial, (3.14) using standard root finding functions in MATLAB (code available upon request) for a set of parameters $n_1, n_2, \Delta G_1^o$ and ΔG_2^o while varying C_{tot}. The aggregation map shown in Figure 3.4a-c is calculated by fixing n_1, n_2, C_{tot} while varying ΔG_1^o and ΔG_2^o. The obtained mole fractions χ_M, χ_H, χ_J were used as RGB values for each pixel on the maps in Figures 3.4a-c with red, green and blue corresponding to J-aggregate, monomer and H-aggregate respectively.

Number of real positive roots of the polynomial:

For $n_1 = 2$, (3.14) can be simplified to a general form $ax^m + bx^2 + x - c = 0$ where m is a large even number and $a, b, c > 0$. It can be proven that any general equation of this form will only have one real positive root.[i]

Let us denote the polynomial as $P(x) = ax^m + bx^2 + x - c$. Therefore, $P(0) = -c$ and $\lim_{x\to\infty} P(x) = \infty$. Using intermediate value theorem, $P(x)$ will have *at least one real positive root*. Further, $P'(x) = max^{m-1} + 2bx + 1$ which is always positive for all $x \geq 0$ as long as $a, b, c > 0$ which is true in this case (equilibrium constants and aggregation numbers are always positive). In other words, $P(x)$ is a monotonically increasing function for all $x > 0$. Using Rolle's theorem, $P(x)$ can have *at most one real positive root*. Therefore, $P(x)$ has *exactly one real positive root*.

Dependence on choice of pathway

This model does not depend on the choice of pathway. We obtain the same characteristic polynomial if we write the equilibrium equations as monomers adding on to H-aggregates instead of H-dimers exclusively reacting to form J-aggregates, as shown below.

$$H + (n_1 \cdot n_2 - n_1)M \rightleftharpoons J \qquad (3.16)$$

Here, we model the equilibrium as monomers adding on to the H-aggregate as opposed to H-aggregates combining to form a J-aggregates in eq. (3.7) and (3.8). The stoichiometric coefficient

[i] N. S. (https://math.stackexchange.com/users/9176/n-s), Is there an analytical way to find the number of real positive roots of polynomials of the form ax^m + bx^2 + x − c = 0?, URL (version: 2019-12-20): https://math.stackexchange.com/q/3483221.

$n_1 \cdot n_2 - n_1$ is necessary to balance the equation. Let K_2' denote the equilibrium constant for eq. (3.16).

$$K_2' = \frac{C_J}{C_H \cdot C_M^{n_1 \cdot n_2 - n_1}} \qquad (3.17)$$

Substituting C_H from eq. (3.11) and rearranging,

$$C_J = K_2' \cdot K_1 \cdot C_M^{n_1 \cdot n_2} \qquad (3.18)$$

In order to relate the K_2' with K_2, we multiply eq. (3.7) by $n_2 - 1$ and add to eq. (3.8), resulting in eq. (3.16).

$$(n_2 - 1) \cdot n_1 \cdot M \rightleftharpoons (n_2 - 1)H; \qquad K_1^{n_2 - 1}$$

$$+ \quad n_2 H \rightleftharpoons J; \qquad K_2$$

$$H + (n_1 \cdot n_2 - n_1)M \rightleftharpoons J; \qquad K_1^{n_2 - 1} \cdot K_2$$

Therefore, we get $K_2' = K_1^{n_2 - 1} \cdot K_2$. Substituting this in eq. (3.18), we obtain a relationship that is same as eq. (3.12),

$$C_J = K_1^{n_2} \cdot K_2 \cdot C_M^{n_1 \cdot n_2} \qquad (3.19)$$

Thus, substituting eq. (3.9) and (3.18) for C_H and C_J respectively, in eq. (3.13), we obtain the same characteristic polynomial as eq. (3.14).

$$n_1 \cdot n_2 \cdot K_2 \cdot K_1^{n_2} \cdot C_M^{n_1 \cdot n_2} + n_1 \cdot K_1 \cdot C_M^{n_1} + C_M - C_{tot} = 0 \qquad (3.20)$$

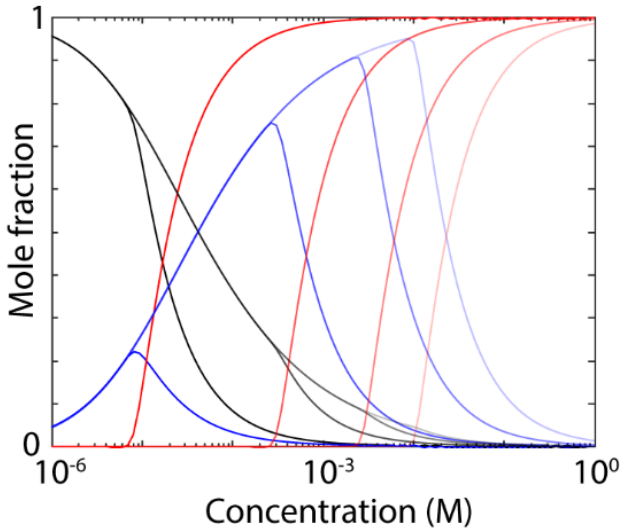

Figure 3.9 Dependence of mole fractions on aggregation numbers

Mole fractions of the monomer (black), H-aggregates (blue) and J-aggregates (red) as a function of total dye concentration for ΔG_1^o = -25 kJ/mol and ΔG_2^o = -300 kJ/mol ; n_1 = 2 and n_2 = 10, 15, 20 and 25 (darkest to lightest respectively).

Effect of aggregation number

Given the extended nature of J-aggregates, realistic n_2 values to be used in the model should be very large (> 10^2). However, finding roots of high order polynomials with existing algorithms is subject to error. To assess the approximation of the effect of increasing aggregation number in (3.14), we plot mole fraction in Figure 3.9 for higher n_2 values. With increasing n_2 we observe a delayed onset or sharp 'turn-on' of J-aggregation concurrent with a sharp decrease in monomer and H-aggregate.

Non-negative matrix factorization

We obtain the mole fraction from experimental data using non-negative matrix factorization (NNMF). In NNMF, a large matrix **V** is factorized into two matrices **W** and **H** where all elements of the matrices are non-negative numbers. We construct a matrix of the spectra shown in Figure 3.10 with each row representing a spectrum at a different dye concentration, $\mathbf{V}_{\mathrm{m\ x\ n}}$ where m and n are the number of samples and number of elements in one spectrum respectively. Using the standard NNMF package from MATLAB, we factorize this matrix into a weights matrix $\mathbf{W}_{\mathrm{m\ x\ 3}}$ and a spectra matrix $\mathbf{H}_{\mathrm{3\ x\ n}}$ where each row represents the spectrum of a pure component. We narrow down the NNMF algorithm by using starting points for known spectra of monomers and J-aggregates. While pure monomer spectrum is easily isolated, we chose a spectrum at high dye and salt concentration at low % MeOH for the J-aggregate since these conditions yield mostly J-aggregated species.

$$\boldsymbol{V}_{m\times n} = \boldsymbol{W}_{m\times 3} * \boldsymbol{H}_{3\times n} \qquad (3.21)$$

The factors $\boldsymbol{W}$ and $\boldsymbol{H}$ are chosen such as to minimize the root mean square residual (F) of the product with original matrix where $F = \sqrt{\frac{\sum_{n,m}|\boldsymbol{V}-\boldsymbol{W}*\boldsymbol{H}|^2}{n*m}}$. The matrix $\boldsymbol{H}$ is plotted in Figure3.4g. The three vectors obtained from NNMF represent the spectra of each component i.e. monomer, H-aggregate and J-aggregate. We normalize the weights matrix $\boldsymbol{W}$ along each row to get experimental mole fractions (circles on Figure 3.4h) $W_{ij} = \frac{w_{ij}}{\sum_j w_{ij}}$. We interpolate this function and obtain the crossing point where the normalized weights corresponding to the monomer and H-aggregate are equal. Later on, we will use eq. (3.24) to obtain the experimental value of ΔG_1^o from the monomer H-aggregate crossing concentration.

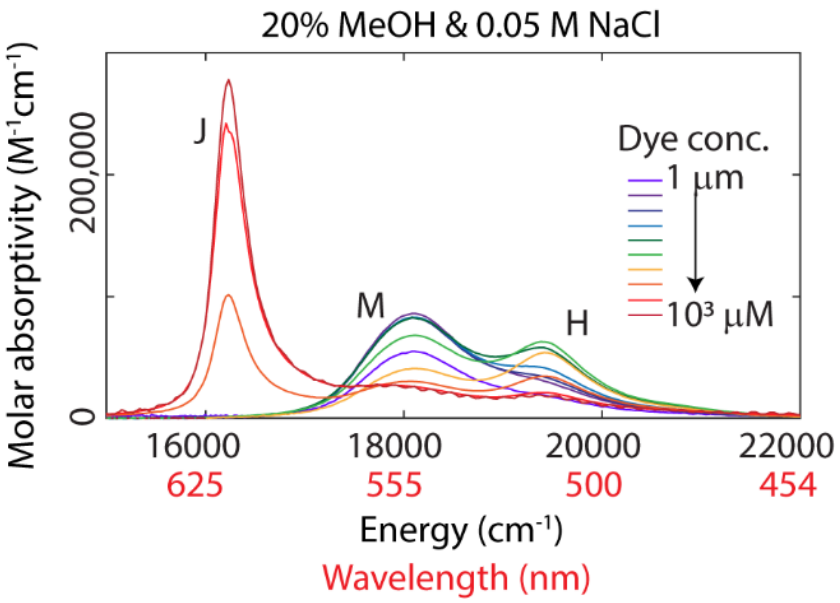

Figure 3.10. Concentration dependent spectra of Cy3-Et

Experimental concentration dependence spectra of Cy3-Et in 20% MeOH and 0.05 M salt. This dataset was used to perform NNMF.

Obtaining experimental Gibbs free energies

Derivation of analytical expression for ΔG_1^o *:* To decrease the fitting space, we derive a simple analytical expression for ΔG_1^o using the monomer to H-aggregate crossing point. We apply the condition $\chi_M = \chi_H$ or $C_M = n_1 \cdot C_H$ on eq. (8). For $n_1 = 2$, combining this condition with equation (3.9) gives $C_M = {}^1/_{(2 \cdot K_1)}$. Substituting this in eq. (3.14), we get

$$\frac{n_2 \cdot K_2}{2^{(2n_2-1)}} \cdot \left(\frac{1}{K_1}\right)^{n_2} + \frac{1}{K_1} - C'_{tot} = 0 \qquad \text{or} \qquad (3.22)$$

$$\frac{n_2 \cdot e^{-\Delta G_2^o/RT}}{2^{(2n_2-1)}} \cdot e^{\frac{n_2 \cdot \Delta G_1^o}{RT}} + e^{\frac{\Delta G_1^o}{RT}} - C'_{tot} = 0$$

where C'_{tot} is the dye concentration where monomer and H-aggregate mole fractions are same and $\frac{1}{K_1} = e^{\Delta G_1^o/RT}$. For $\Delta G_1^o < 0$,taking the limit $n_2 \to \infty$, eq. (3.21) can be reduced to

$$\frac{1}{K_1} = C_{tot} \text{ or } e^{\Delta G_1^o/RT} = C'_{tot} \tag{3.23}$$

$$\text{Therefore, } \Delta G_1^o = RT \ln(C'_{tot}) \tag{3.24}$$

Interpolating the experimental mole fractions obtained from NNMF in Figure 3.4h, we obtain $C'_{tot} = 40.8\ \mu M$ which results in $\Delta G_1^\circ = -25.0$ kJ/mol.

Fitting model to experimental data: We define a custom function using the polynomial in (3.14) with n_1, n_2 as fixed parameters and $\Delta G_1^o, \Delta G_2^o$ free parameters. We use the analytically obtained value of ΔG_1^o as a starting point in the fitting. Narrowing down the possible range of ΔG_2^o value, on the other hand, was more complicated due to its strong dependence on n_2. Therefore, we fix the aggregation numbers in our model to $n_1 = 2$ and $n_2 = 30$ (limited by our computational capacity) while fitting the data in Figure 3.4h. We get an estimate of ΔG_2^o by visual inspection of the mole fraction curves and then use this estimate as a starting point in the least squares curve fitting. We then fit our three component model to this data, finding good agreement for n_1 = 2 and n_2 = 30 (greater values of $n_2$are numerically unstable) and optimize the values of $\Delta G_1^\circ = -24.8$ kJ/mol, $\Delta G_2^\circ = -740.2$ kJ/mol using least-squares curve fitting (lines in Figure 3.4h).

Applying design principles to TDBC

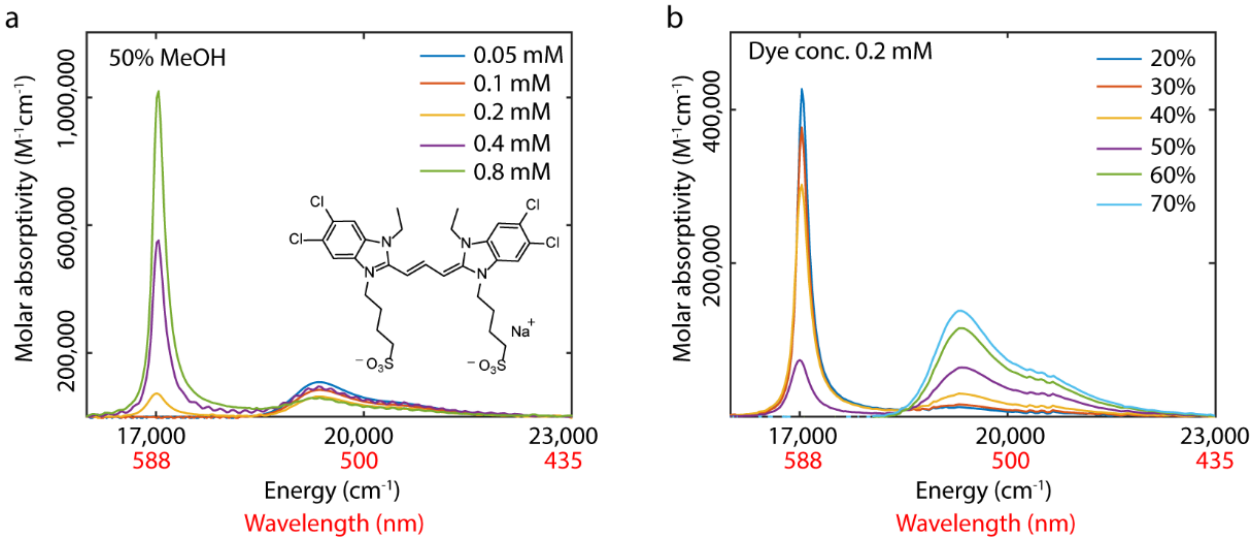

Figure 3.11. Screening aggregation conditions for TDBC

Absorption spectra of TDBC dye aggregates formed by independently tuning a. dye concentration in MeOH:water mixtures with 50% MeOH v/v; (inset) structure of TDBC dye; b. 20% - 70% MeOH in methanol-water mixtures with fixed dye concentration of 0.2 mM.

Chapter 4

Tuning the Excitonic Band Structure of Two-Dimensional Aggregates

In the previous chapter, we prepared a library of 2D aggregates with absorptions ranging from visible through SWIR wavelengths. Different building blocks for each aggregate within this library result in subtle differences in the nanoscale molecular packing (slips and brick lengths). In this chapter, we discuss how these differences affect the excitonic band structure and utilize such molecular packing parameters to modulate the excitonic band structure from mid-band I-aggregates to band-edge J-aggregates.

4.1 Importance of excitonic band structure

Excitonically coupled molecular aggregates are materials derived from chromophores whose optoelectronic behavior changes upon aggregation due to collective interactions of monomer transition dipole moments. Such aggregates are represented in many natural and synthetic materials, including conjugated polymers, supramolecular chromophore assemblies and photosynthetic complexes.[1,12] Extended aggregates of chromophores have found applications in many areas - picosecond energy transfer,[12,47,154] polaritonics or plexitonics,[51,148,173,174] various optoelectronic devices such as luminescent solar concentrators, OLEDs,[61,62] and shortwave infrared technologies (SWIR, 1000-2000 nm).[66,69,175] In extended aggregate systems, the huge enhancements of transition dipole moments lead to excitonic superradiance wherein a large number of in-phase TDMs lead to collective emission phenomena. Superradiance can be useful in

modulating exciton transport and telecommunication related applications.[66,79] Excitonic band structure plays a key role in all of these applications as quantum yields, energy/charge transfer rates and other photophysical properties are directly dependent on it. Structure-property relationships for the excitonic band structures will therefore allow for supramolecular tunability of such properties, enabling rational design of molecular aggregates.

In the 1950s, Kasha developed a framework to relate the excitonic shifts in the optical spectra of molecular aggregates to the underlying structure. Within this framework, when the transition dipoles are arranged head-to-tail, the excitonic state with all dipoles oscillating in-phase (or $k = 0$) is lowered in energy compared to the monomer. This leads to a red shift in the optical transitions. 1D excitonic systems with such head-to-tail arrangements are called J-aggregates.[19] This $k = 0$ state is the 'bright state' as it has the highest transition probability based on Fermi's golden rule.[1] Conversely, co-facial arrangement leads to blue shifted transitions as the bright state is higher in energy than the monomer, known as H-aggregates. All other arrangements result in Davydov splitting with two dipoles per unit cell, producing two excitonic peaks for any single set of electronic transitions.[149,176,177] J-aggregates are typically characterized by enhanced quantum yields from their respective monomers, high radiative rates and narrow linewitdths.[12,32] H-aggregates, on the other hand, usually have low quantum yields as non-radiative relaxation to the dark band edge excitonic state dominates the excited state decay.[12]

4.2 Deviations from Kasha's model

Kasha's model arises from considering only dimers and 1-dimensional chains as well as nearest neighbor dipolar interactions. These limitations lead to the model's failure in describing systems with permanent dipole moments,[27] charge transfer or quadrupolar excitonic coupling,[113] or higher

dimensional aggregates, e.g. sheet-like and tubular aggregates.[39,145,178] Examples of non-Kasha behavior have also been observed in polydiacetylene, poly(3-hexylthiophene) and other conjugated polymers, referred to as segregated "HJ" aggregates, wherein interchain and intrachain couplings have opposite signs.[7,179,180] In some cases, different forms of couplings can cancel out, resulting in a null aggregate with no excitonic shift in optical spectra in spite of a significant excitonic bandwidth.[129,130] More recently, HJ aggregates with dominant H-like (or J-like) coupling called as Hj (or hJ) aggregates were also reported for perylene diimides.[181]

Using the Frenkel exciton model with only long-range dipole-dipole couplings,[25] we have previously shown the presence of 'I-aggregates' in 2D lattices.[145] We define I-aggregates with an excitonic band where the bright state is red shifted from the monomer but still has dark states below it, drawing characteristics from both H- and J-aggregates. We showed that such behaviors depend upon the relative slip between adjacent monomer in the 2D lattices. I-aggregates have red shifted aggregate to monomer absorption (J-like) and yet low quantum yields (H-like).[145] J-aggregates, on the other hand, should have a band edge bright state and therefore, enhanced quantum yields with respect to the monomers. J-aggregates can also show excitonic superradiance because of the enhanced quantum yields and reduced lifetimes. Superradiance cannot be defined for I-aggregates or H-aggregates as there is no emission from the non-band edge excitonic states to begin with.

4.3 Need for a classification system for 2D aggregates

Since I- and J-aggregates both show aggregate to monomer red shifts, a more comprehensive classification system for 2D aggregates is needed. Here, we demonstrate the distinct possibilities of excitonic band structures in 2D aggregates and their experimental signatures. Pathways for

chemically tuning the excitonic band structures are necessary to access a breadth of photophysical properties in molecular aggregates as well as to optimize material properties for specific applications. For example, chemically tuning the band structures from a non-band edge I-aggregate to band edge J-aggregate will enable aggregates with high quantum yields, a prerequisite for several applications.[58,182]

We start with a detailed discussion of the theoretical basis for excitonic band structures of 2D aggregates provided by Chaung et al.[163] The positive or negative contributions of short and long range couplings lead to critical differences in the band structures which has distinct spectroscopic signatures in emission and temperature dependent properties. Based on this, we provide a classification system for 2D aggregates based on aggregate to monomer shifts, temperature dependent peak shifts and broadening, as well as quantum yield enhancements. We measure quantum yields, lifetimes, superradiance, temperature dependent peak shifts and full-width at half maximum (FWHM) changes across a set of 2D aggregates of six closely related cyanine dyes. We go on to show that such differences in the band structures and ultimately, the photophysical properties, can be manipulated with the supramolecular packing of the chromophores within the extended 2D structures. Specifically, the relative slip between adjacent monomers as well as length of the monomer determine the relative contributions of short and long range couplings, which in turn, lead to the distinct excitonic band structures of H-, I- and J-aggregates. Our findings lead to an internally consistent description of the distinct photophysical behaviors – enhanced or suppressed quantum yields relative to their monomers, differences in superradiance and red or blue shifts with temperature. Stochastic Hamiltonian modelling relates the aggregate geometries and disorders to the underlying band structures, providing a pathway for supramolecular tuning of the observed the photophysical properties. Our findings can be utilized to rationally design molecular

excitonic systems with tunable photophysical properties, enabling optimization of material properties for specific applications.

4.4 Significance of short and long range couplings

We calculate the excitonic density of states (DOS) and the bright state energy using the Frenkel exciton Hamiltonian with brick layer model. This approach is explained in detail in Chapter 2. Within this model, we treat each monomer as a brick ,with a given dipole moment (μ), length (L), width (w), and tile them in a 2D brick layer lattice with different slips (s).[25,29,145] The eigenvalues of this Hamiltonian provide the excitonic DOS and Fermi's golden rule gives the bright state. In Figure 4.1a, we plot the bright state, upper and lower band edge of the DOS for a 2D brick layer aggregate with vaarying slip values. As we increase the slip, the band structure goes from H-aggregate (bright state blue shifted from monomer), to I-aggregate (bright state red shifted but away from the band edge) and finally to J-aggregate (bright state at the lower band edge).

Prior theory by Chuang et al. explains the origin of H-, I- and J-aggregate behaviors on the basis of the types of short and long range couplings in 2D aggregates.[163] The possibilities of short and long range coupling for a 2D aggregate with in-plane TDMs are explained in Figure 4.1b. Long-range interactions in extended 2D systems with in-plane TDMs always contribute a net negative coupling ($J_{LR} < 0$). Short range interactions can either be positive or negative depending on the relative slip, orientation and the coupling model. In cases where the short-range couplings are positive and higher in magnitude than the long range couplings, we obtain a 2D H-aggregate situation. All slip values in the blue region of Figure 4.1a show this behavior. In Figure 4.1c, we show a representative example of the excitonic DOS for a slip value denoted by 'i' on Figure 4.1a. Since there are always some negative contributions in the 2D case, the bright state is not at the

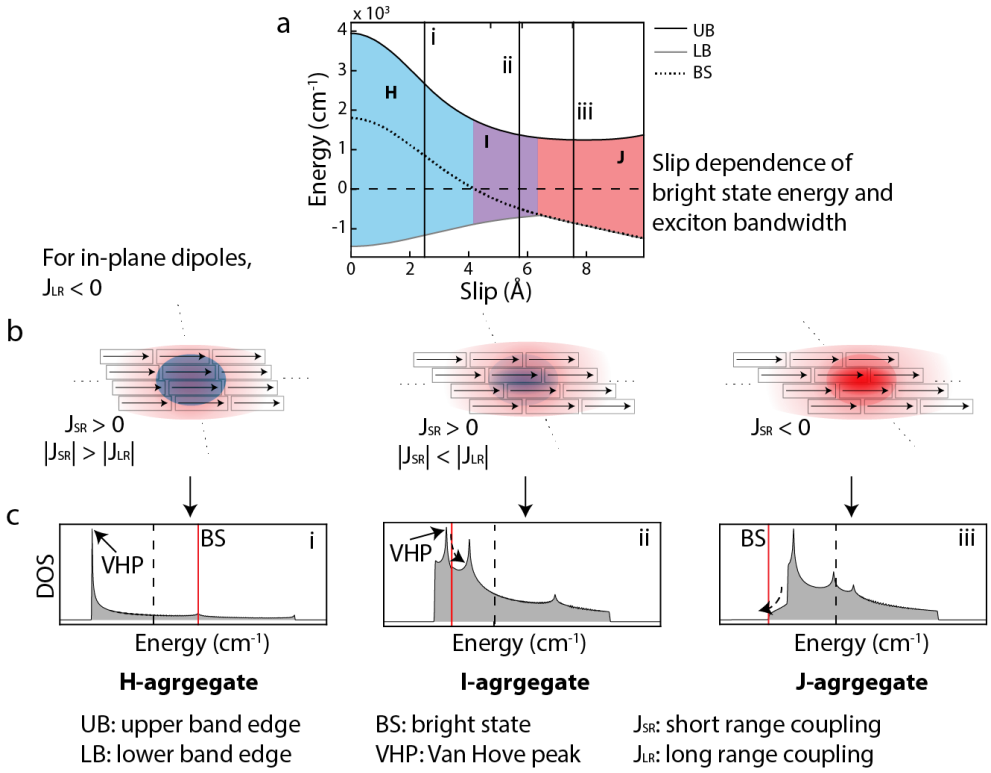

Figure 4.1 Role of short and long range coupling for H-, I-, and J-aggregation.

a. Bandwidth of the excitonic DOS and position of the bright state (dotted line) as a function of slip in 2-dimensional (2D) aggregates, dashed line indicates monomer energy. Blue region: bright state higher in energy than monomer (H-aggregate), purple region: bright state lower in energy than monomer but away from the lower band edge (I-aggregate), and red region: bright state lower in energy than the monomer and at the band edge (J-aggregate), b. schematic showing possibilities of short and long range couplings for 2D aggregates with in-plane dipoles leading to H-, I- and J-aggregates, c. representative excitonic DOS for slips corresponding to the vertical lines i, ii and iii on part a showing H-, I- and J-aggregate band structures respectively. Solid red line indicated bright state energy and dashed line indicates monomer energy. Curved dashed arrows indicate the direction of temperature dependent shifts.

upper band edge.[163] When the short-range coupling is positive, but smaller than the long-range coupling, the bright state is redshifted from the monomer but still has lower energy dark states below, making it an I-aggregate. The overall coupling, in this case, is negative resulting in red shifted aggregate to monomer absorptions. This is denoted by purple shaded region on Figure 4.1a

and a representative DOS is shown in Figure 4.1c corresponding to the slip denoted by 'ii'. For a 2D J-aggregate, both the short and long range couplings are negative, making the bright state also the lowest energy state in the excitonic DOS, similar to Kasha's model. This scenario is shown in red shaded region on Figure 4.1a and a representative DOS in Figure 4.1c (denoted by 'iii').

As shown in Figure 4.1c, the excitonic DOS has several sharp peaks, called as Van Hove Peaks (VHPs). VHPs arise from extremums in the dispersion relations where the dispersion curve is flat i.e. $\frac{dE}{dk} = 0$ (in the 2D case, the extremums are saddle points in the dispersion curves). Effectively, a VHP consists of a large number of states concentrated in a close energy range. In other 2D materials (e.g. graphene), this is known to cause superconductivity, topological insulators and other unusual phenomena.[183–185] In case of the molecular aggregates, position of the bright state relative to the VHPs can be useful in distinguishing I-aggregates from J-aggregates and ultimately, explaining a lot of the photophysical properties such as quantum yields and linewidths.

Chuang et al. also developed a theory providing relationships between the position of bright state relative to the VHP and temperature dependent peak shifts.[163] For bright states lower in energy than the VHP, the local slope of the DOS is positive meaning that there are more dark states on the higher energy side of the bright state than on the lower energy side. Therefore, there is an asymmetric distribution of the dark states near the bright state which pushes the bright state away towards lower energy, resulting in a red shift with increasing temperature. Thus, Chuang et al. prove that the positive slope near the bright state results in a red shift with increasing temperature (indicated by dashed arrows on Figure 4.1c). Conversely, for bright states higher in energy than the VHP, the local slope of the DOS is negative with relatively higher number of states below the bright state and thus, we observe a temperature dependent blue shift.

4.5 Classification scheme for 2D aggregates

Such distinct possibilities in 2D aggregates suggest that excitonic peak shifts alone are not diagnostic of the band structure, coupling strength, and emissivity. To probe higher dimensional aggregate structures, one must go beyond aggregate to monomer absorption peak shifts and narrowing. Expanding on previous theories,[145,163] we present a classification system encompassing such diverse excitonic behaviors in 2D aggregates based on peak shifts and peak broadening with temperature as well as room temperature quantum yields. Following paragraph and Figure 4.2 summarize our classification system:

For 2D systems, a blue shifted absorption from aggregate to monomer indicates H-aggregation. Whereas, for aggregates with red shifted absorptions from their monomers, both I- and J-aggregation is possible. The position of the bright state with respect to the VHPs contributes to the temperature dependent properties. For band-edge J-aggregates, the local slope of the DOS is always positive. Therefore, band-edge J-aggregates must show red shifts with increasing temperature, whereas I-aggregates can show red, blue or no shifts with temperature depending on the local slope (positive, negative or zero respectively) of the DOS near the bright state. As a result, a blue or not shifting aggregate peak with temperature can be a conclusive evidence for an I-aggregate. Temperature dependent red shift along with enhanced quantum yield at room temperature can be a conclusive evidence for J-aggregates.

Changes in quantum yields with temperature can also be related to I- or J-aggregation behavior based on thermal occupation of the bright state. In band-edge J-aggregates, one expects a decreasing quantum yield upon heating as the occupation number of the lowest energy bright state will decrease with temperature. For non-band edge I-aggregates, higher temperatures enable

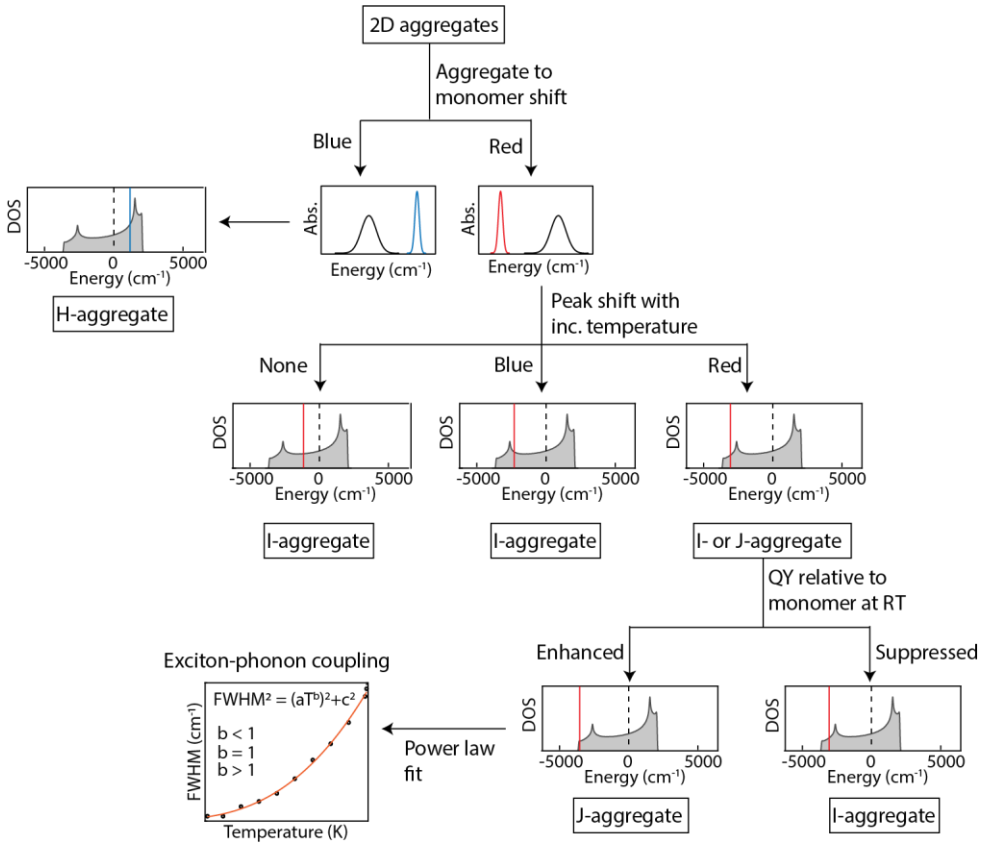

Figure 4.2 Flowchart summarizing the classification scheme for 2-dimensional excitonic aggregates.

The classification is based on aggregate to monomer shifts, temperature dependent shifts and quantum yield enhancement from the monomers. Dashed vertical lines indicate monomer energy and solid red or blue lines indicate the bright state.

occupation of higher energy states leading to increasing quantum yield upon heating. For band-edge J-aggregates, temperature dependent power laws can inform on exciton-phonon coupling processes that lead to thermal broadening (discussed in detail later). Further, the amount of thermal broadening can also be used as a relative measure of the total distance of the bright state from the band edge (also discussed in detail later).[145] Overall, these properties form a complete description of the distinct behaviors possible in 2D excitonic systems, where each experimental observable

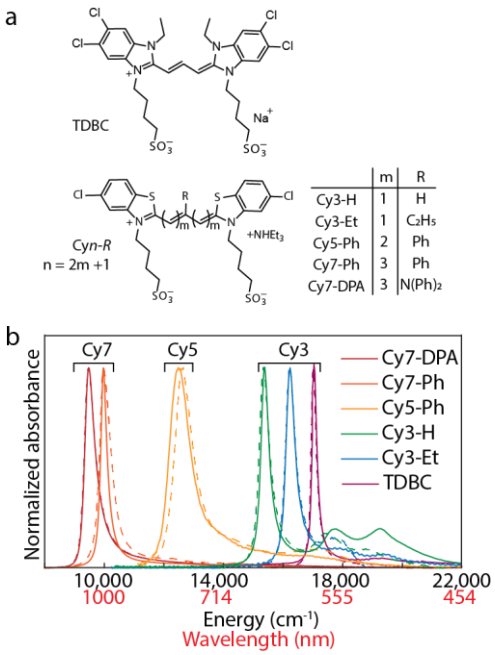

Figure 4.3 Comparitive set of six 2D aggregates - dye structures and aggregate absorption spectra

a. Structure of the six dyes explored in this work – benzimidazole cyanine dye TDBC and benzothiazole cyanine with varyingcentral position subsitutions and bridge lengths, b. Absorption spectra of all the aggregates in solutions (solid lines) and dried sugar matrix (dashed lines). All aggregate solutions are in water-methanol or aq. NaCl-methanol mixtures.

(quantum yields, temperature dependent shifts and broadening, power laws) can be related to a specific aspect of the excitonic band structure.

4.6 Differences in emissive properties of six 2D aggregates

We demonstrate examples of the distinct excitonic band structures across 2D aggregates of six dyes with different polymethine bridge lengths (Cy3, Cy5 and Cy7; Cy = cyanine) and substitutions on the central position, shown in Figure 4.3a. In our earlier work, thermodynamic control of the aggregate self-assembly enabled selective stabilization of each aggregate morphology via an interplay of concentration, solvent:non-solvent ratio, and dielectric screening.

Using this approach, we were able to stabilize the 2D sheet-like morphology of all the dyes studied here (Figure 4.6).[186] We also include the well-known dye 3,3‘-bis(4-sulfobutyl)-5,5‘,6,6‘-tetrachloro-1,1‘-diethylbenzimidacarbocyanine, sodium salt (TDBC), commonly used in photonic applications.[187,188] All 2D aggregates are prepared by injecting a methanol solution of the dye in water or aqueous NaCl (see experimental section for exact conditions), followed by equilibration in dark for 24 h. By changing the dye lengths as well substitutions on the central position of the cyanine bridge (Figure 4.3a), we afford extended 2D aggregates with different brick lengths and slips. Prior models have related these parameters to the subtle variations in excitonic band structure.[163,178] As shown in Figure 4.3b, the absorptions of these 2D aggregates range from 587 nm (TDBC) to 1050 nm (Cy7-DPA). The narrow lineshape with a high energy tail observed across all aggregates is characteristic of extended 2D aggregate structures, and is also seen in other 2D aggregates of perylene bisimides.[35]

We measure the emissive properties of all the aggregates at room temperature (RT). We highlight TDBC as an archetypal example in Figure 4.4 owing to the narrowest absorption linewidth (Figure 4.3b) and highest quantum yield of TDBC aggregate (discussed later in Table 4.1). As seen from the solution absorption and emission spectra in Figure 4.4a, TDBC aggregate (red) has narrowed absorption and emission compared to the monomer (blue), and very small Stokes shift (2 nm) in the aggregate form.[12] Figure 4.4a inset shows the time-correlated single photon counting (TCSPC) histograms for both the monomer and aggregate of TDBC. Absolute quantum yields and lifetimes in RT solutions for all the monomers and aggregates across the library are shown in Table 4.1 (see Figure 4.7 and Table 4.3 for all absorption, emission spectra and lifetimes breakdown of the aggregates). We calculate the radiative rates for all the aggregates

and monomers from lifetimes and quantum yield of each sample. We define excitonic superradiance (η_{SR}) as:

$$\eta_{SR} = \frac{\mu_{agg}^2}{\mu_{mon}^2} \tag{4.1}$$

where μ_{agg} and μ_{mon} are the transition dipole moments of aggregate and monomer respectively. Other definitions of superradiance exist in literature,[38,39] superradiance factor as high as 62 has been reported for thiacarbocyanine J-aggregates using previous metrics. However, these do not account for the effects of the energy gap law.[43] We use eq. (4.1) which includes the effects of drastic changes in energy gaps of aggregate to monomer using the following equation:

$$\mu^2 = \frac{\Phi 3\pi\varepsilon_o \hbar^4 c^3}{\tau n {E_g}^3} \tag{4.2}$$

where Φ, τ, n and E_g denote the quantum yield, lifetime, refractive index and energy gap respectively. We approximate the energy gap as the mean of absorption and emission peak energies.

We observe that all the Cy3 dye aggregates have significantly enhanced quantum yields at RT as compared to their respective monomers, with TDBC showing the highest $\Phi_{agg} = 49 \pm 3$ % (17 times higher than the monomer). On the other hand, the quantum yield of the Cy5-Ph aggregate was found to be suppressed from the monomer. Both the Cy7 dyes had very low quantum yields that were below our detectable limit (< 0.01 %). All the Cy3 dye aggregates were also superradiant indicating enhanced transition dipole moments in the aggregates. TDBC and Cy3-Et aggregates were superradiant in spite of having higher aggregate lifetime than monomer. This can be explained by the relatively higher enhancement factors for the quantum yields of TDBC and Cy3-Et aggregates. Moreover, the radiative rates are known to show an inverse relationship with the

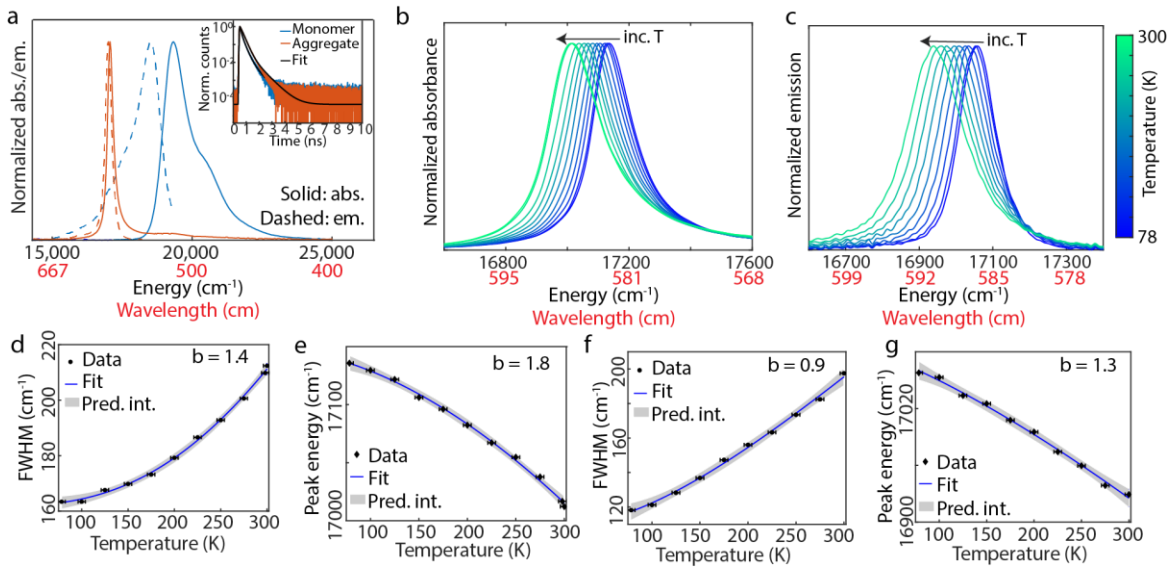

Figure 4.4 Complete spectroscopic characterization of TDBC aggregate – absorption, emission, lifetimes, emperature dependent absorption and emission

a. Normalized absorption (solid lines) and emission (dashed lines) spectra for TDBC monomer (blue), and TDBC aggregate (red). Inset: Time correlated single photon counting data for TDBC monomer (blue), and TDBC aggregate (red) with biexponential fits in black, b-g. temperature dependent spectroscopy data for TDBC aggregate in sugar matrix from 78 K to 300 K with estimated error of ±2 K, b. normalized absorption spectra, c. normalized emission spectra, d. absorption full-width at half-maximum (FWHM), e. absorption peak energy, f. emission FWHM, g. emission peak energy. Fits are from eqs. (3) and (4) for FWHM and peak energies respectively.

energy gap.[43] The measured lifetimes do not include this factor, which is accounted for later in eq. (2). In case of TDBC, aggregate lifetime is 1.8 times higher than that of the monomer (without accounting for the lower energy gap effects) but the quantum yield is about 17 times higher. Cy5-Ph aggregate had a suppressed transition dipole moment from its monomer, mainly attributed to the two orders of magnitude lower quantum yield than the monomer. A notable point is that according to the traditional H- and J-aggregate classification based on aggregate to monomer

shifts, all these aggregates would be J-aggregates despite the significant differences in their emissive properties (Figure 4.7).

Table 4.1 Emission and superradiance parameters for all 2D aggregates in solutions at room temperature.

Lifetimes (τ), quantum yields (ϕ), and transiton dipole moments (μ) for all monomers (subscript *mon*) and aggregates (subscript *agg*) along with superradiance rates (η_{SR}) calculated using eq. (4.1) and eq. (4.2) are shown. Errors on quantum yields are standard deviations across 3 samples.

Dye	τ_{mon} **(ps)**	τ_{agg} **(ps)**	Φ_{mon} **(%)**	Φ_{agg} **(%)**	μ_{mon} **(D)**	μ_{agg} **(D)**	η_{SR}
TDBC	80	150	2.8 ± 0.2	49 ± 3	13	40	9
Cy3-Et	60	195	0.31 ± 0.03	14 ± 2	5	20	18
Cy3-H	268	207	5.7 ± 0.6	13 ± 4	10	20	4
Cy5-Ph	467	229	9.2 ± 0.5	0.028 ± 0.005	12	1	0.008
Cy7-Ph	410	-	4.4 ± 0.2	-	11	-	-
Cy7-DPA	637	-	2.3 ± 0.2	-	7	-	-

4.7.Temperature dependent spectroscopy of sugar matrix stabilized aggregates

To investigate the origins of such differences, we use temperature dependent spectroscopy. We stabilize all the 2D aggregates in a 50:50 (w/w) sucrose:trehalose sugar matrix, following a previously reported procedure.[117] Sugar matrix stabilization protects the aggregate morphologies at low temperature so that other possibilities like the changes in the aggregate structure itself can be ruled out. Moreover, the frustrated packing afforded by structural mismatch between the sugars keep the samples optically transparent by forming a glassy matrix (unlike water which crystallizes at 273 K). Figure 4.3b shows the absorption spectra of all J-aggregates in sugar matrix (dashed

lines) superimposed with their solution spectra (solid lines). We do not observe major changes in the lineshapes or peak positions indicating that the overall aggregate morphologies are still intact. In some cases, there is a slight broadening (Cy7-Ph) or shift (Cy5-Ph) in the sugar matrix, indicative of additional disorder though it is minor compared to the overall lineshape.

We conduct temperature dependent absorption spectroscopy on all the sugar matrix stabilized aggregates, along with temperature dependent emission for all the aggregates with detectable quantum yields. Figures 4.4b-g show one complete dataset for TDBC while those for the other dyes can be found in Figures 4.8-4.11. For TDBC, we observe that the aggregate peak red shifts and broadens as we increase the temperature from 78K to 300K (Figure 4.4b-c). Summarized in Table 4.2, all the Cy3 and Cy5 aggregates including TDBC redshift with increasing temperature while the Cy7 aggregates show blue or no shift (Figure 4.4b and Figure 4.8e-f).

The red shifting behavior for all Cy3 dyes implies a bright state that is lower in energy than the VHP. The high RT quantum yields suggest that they are not only at lower energy than the VHP but are also at the band-edge. Therefore, we classify all the Cy3 aggregates including TDBC as Kasha's J-aggregates with band-edge bright states. In contrast, Cy5-Ph aggregates have a red shifting peak with temperature even though the RT quantum yield is suppressed from the monomer. This implies that the bright state of Cy5-Ph is at lower energy of the VHP but still has significant dark states below such that non-radiative pathways dominate the excited state decay. Therefore, we classify Cy5-Ph as an I-aggregate with a bright state lower in energy than the VHP. All the Cy3 and Cy5 aggregates show similar trends in temperature dependent emission as well, where the aggregate peaks red shift with increasing temperature (Figures 4.10-4.11).

Recalling the theory by Chuang et al., the temperature dependent shifts are sensitive to the local slope of the DOS.[163] Therefore, Cy7-Ph which showed no shift (Figure 4.8), must have a bright state farther from the band-edge in a relatively flat region between the VHPs. Since Cy7-DPA is blue shifting with temperature, it has a bright state at higher energy than the VHP (or locally negative slope of the DOS). Therefore, we classify both Cy7 cases as I-aggregates.

These observations are also consistent with our previous studies where we used a thermal broadening based metric to conclude that Cy7-Ph has a bright state farther away from the band-edge as compared to Cy7-DPA.[145] The relative distance of the bright state from the band edge can be qualitatively gauged by means of the amount of thermal broadening. In cases where the bright state so far from the band edge that it is thermally inaccessible, one expects no broadening (irrespective of the relative position to the VHP), as in the Cy7-Ph aggregate (Figure 4.8). Cy7-DPA shows thermal broadening despite being an I-aggregate, meaning that the bright state is closer to the band-edge such that it is thermally accessible.

In band-edge J-aggregates, thermal line broadening and shifts are modeled using exciton-phonon coupling with the environment which have been previously described with power laws and uniquely reflect the combination of exciton DOS and exciton-phonon coupling spectral density (also called as system-bath coupling).[127,189–191] Linewdiths can be thought of as the sum of rates of varios phonon assisted exciton scattering processes. The rates are a result of energy conservation between the system and the surrounding bath, as well as the couplings between the two. The latter is a constant for homogenous, translationally symmetric systems while the former gives a weighted average of system+bath DOS, and therefore the power law. Such power law scalings of FWHM and peak shifts can be used as an indication of the types of underlying exciton-phonon coupling processes. We fit the extracted linewidths and peak energies to power laws as shown in

Figure 4.4d-g. The following eq. (4.3) and eq. (4.4), were used for fitting the FWHM (ω) and peak energies (ν_o) respectively:

$$\omega^2 = (aT^b)^2 + c^2 \tag{4.3}$$

$$\nu_0 = a_0 T^{b_0} + c_0 \tag{4.4}$$

The first terms denote the homogeneous contributions following a power law (b, b_0 for FWHM and peak energies, respectively) while the second term (c, c_0 for FWHM and peak energies, respectively) denotes the extrapolated inhomogeneous limit at 0 K. Table 4.2 summarizes the power laws obtained from temperature dependent absorptions for all band-edge aggregates. The corresponding power law fits for the rest of the aggregates are shown in Figure 4.9.

Table 4.2 Summary of temperature dependence absorption data for 2D aggregates.
Power laws (b parameter from eq. (4.3) for FWHM and b_0 from eq. (4.4) for peak energies), and direction of temperature dependent peak shifts. Error ranges are from 95% confidence intervals.

Dye	**Power law for FWHM (b)**	**Power law for peak energies (b)**	**Peak shift with increasing temperature**
TDBC	1.4 ± 0.2	1.8 ± 0.3	Red
Cy3-Et	0.9 ± 0.1	1.0 ± 0.2	Red
Cy3-H	1.0 ± 0.2	1.1 ± 0.6	Red
Cy5-Ph	1.0 ± 0.2	1.1 ± 0.3	Red
Cy7-Ph	-	-	None
Cy7-DPA	-	-	Blue

Despite similar excitonic shifts and energies, we find that the benzathiazole aggregates display a different power-law dependence in its spectral shift and FWHM compared to the benzimidazole dye TDBC aggregate. We hypothesize that the different heterocycle and additional alkyl group results in a modified phonon DOS for TDBC. The power laws observed here for 2D aggregates

are lower than those reported for other 1D and quasi-1D systems such as light-harvesting nanotubes (b = 2 ± 0.5) and pseudoisocyanine (b = 3.4).[117,191]

Changes in linewidths arise from the coupling of exciton degrees of freedom (system) to vibrational degrees of freedom (environment/ phonon bath). Specifically, under the weak-coupling, fast-environment limit, to which many of the J-aggregates studied belong, the power-law exponent (b) of the temperature dependent line width can be broken down as $b = d + s + 1$, where d and s are the scaling of the exciton DOS at the band edge, and low-frequency system-bath coupling spectral density respectively.[127,189,192] $s = 1$ for an Ohmic bath while $s < 1$ for a subohmic bath. A similar expression can be derived for temperature dependent peak shifts which reflects the same underlying band structure (see Section 4.11).[163] For 2D excitonic systems with non-nearest neighbor dipole-dipole couplings, the system DOS scaling has been shown to follow a $d = 0.5$ dependence.[193] Thus, we obtain $s = 0$ for TDBC and $s \sim -0.5$ for the rest of the benzothiazole Cy3 and Cy5 aggregates indicating that the system-bath coupling spectral density in the TDBC aggregate is independent of frequency while the negative sign for rest of the band-edge aggregates indicates an inverse scaling. The scaling laws may be explained by the fact that the excitonic couplings in these systems are quite large (~10^3 cm^{-1}), and the higher frequency components of system-bath coupling will be highly suppressed in comparison. For finite coherent length, pure dephasing may compete with population relaxation and lead to linear scaling with temperature.[192] Although, this is unlikely in our case, since all aggregates had upto micron scale sizes as seen from cryoEM images (Figure 4.6).[186]

4.8 Screening aggregate geometries using stochastic modeling of the Hamiltonian

The general method for calculating the excitonic DOS is explained in Figure 4.12 along with slip dependence of the bright state and the band edges for TDBC and Cy7-DPA. We screen large parameter space for of possible aggregate packing parameters (slips) and disorder values for all the aggregates using the stochastic sampling methods for the DOS, and Chebyshev kernels the absorption spectra.[178] The stochastic density of states is calculated by taking a random superposition of all eigenstates, projecting it down onto a specific energy in the spectrum, and then averaging over many random samplings. This approach is computationally less expensive than diagolalizing large Hamiltonians and allows for rapid screening of several aggregate geometries with realistic sizes (~ 10^6 monomer units). Several disorder realizations can be afforded at no additional cost. By screening thousands of configurations for each aggregate, we obtain the slip dependence of the excitonic band and the position of the bright state ($k = 0$). In Figure 4.13, we show large parameter screens for FWHM and peak positions of all six aggregates. Best fit slip parameters for each aggregate were determined by comparing the calculated spectral widths to 0 K FWHM obtained from the power law fits listed in Table 4.5 i.e parameter c from eq. (4.3). We narrow down the possible slip – disorder space to the grey squares in Figure 4.13.

From the narrowed down range of slips (grey squares on Figure 4.13), we use a slip of 5.0 Å and plot the calculated excitonic DOS and absorption spectra in Figure 4.5a. While the realistic slips may be slightly different for each aggregate depending on the central position substitution, we use this representative value as it was consistent with our experimental observations among the narrowed down range of slips. As the brick length increases from Cy3 to Cy7 dyes and relative

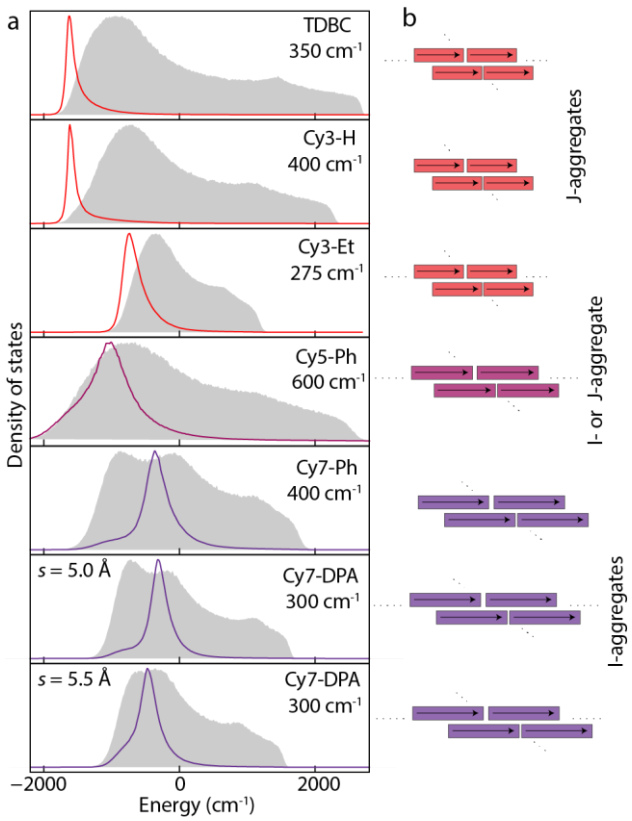

Figure 4.5 calculated excitonic band structures and corresponding aggregate geometries

a. Calculated exciton density of states (grey region) and absorption spectra (red lines) at 0 K of all 2D aggregates for a slip of 5.0 Å (top six panels) and given disorder values. The last panel shows the same for Cy7-DPA with higher slip of 5.5 Å, b. schematics of the corresponding brick layer geometries.

slip (normalized to brick length) decreases (Figure 4.5b), we observe that the excitonic band structure goes from band-edge J-aggregate to mid-band I-aggregate. Our calculations in Figure 4.5a show that all the Cy3 dyes have a band-edge bright state, lower energy than the VHP. This is consistent with our inference from Tables 4.1 and 4.2, based on temperature dependent shifts and emissive properties. Cy5-Ph, while lower energy than the VHP, also has a broad linewidth with significant oscillator strength farther up in the DOS, explaining the suppression of aggregate to monomer quantum yield and the red shifting behavior. Finally, Cy7-Ph and Cy7-DPA both have bright states away from the band-edge, explaining the I-aggregate behavior seen in our

experiments. Cy7-Ph also has the absorption peak in the relatively flat region of the DOS, consistent with our temperature dependent experiments which showed no shift. While Cy7-DPA appears to have local negative slope at 5.0 Å slip, the realistic slip is higher than that of Cy7-Ph due to a bulkier center position substitution as we have previously shown.[145] This is shown in the bottom two panels of Figure 4.5a, where a higher slip value pushes the bright state in a locally positive slope region of the DOS, explaining the temperature dependent blue shifts. The bottom three panels clearly confirm our inference from Table 4.2 that both the Cy7 aggregates are I-aggregates.

Thus, supramolecular modulation of chromophore packing in 2D aggregates can allow for tunable excitonic band structures where the position of the bright state relative to the band-edge and to the VHP can be controlled with slips and molecular lengths. Such dependencies are a direct consequence of the relative contributions of positive and negative couplings afforded by different brick layer geometries. Furthermore, these relations can be exploited to chemically tune the band structures of higher dimensional aggregates and ultimately control the photophysical properties relevant for their applications. J-aggregates can be useful for non-invasive SWIR imaging due to their high quantum yields and narrow linewidths but SWIR aggregates reported so far have very low quantum yields ($\phi_F < 1\%$), possibly because many are, in fact, non-band edge I-aggregates.[69,175] By making SWIR aggregates with higher slips, their bright states can be pushed close to the band-edge yielding high quantum yield J-aggregates in SWIR, which could be transformative for SWIR technologies.

We note that our findings are agnostic of the nature of the couplings (dipole-dipole, charge-transfer etc.) and depend mainly on the relative strengths of the short and long range couplings. Here, we show the importance of supramolecular packing parameter in modulating the relative

contributions of short and long range couplings. Specifically, the point dipole model greatly overestimates the short-range contributions and results in a very small I-aggregate region while the more accurate TC model gives a much larger I-aggregate region (Figures 4.12c-d). In addition to the supramolecular geometries, the type of the nearest-neighbor couplings can also be used to modulate the relative contributions from short and long range couplings.

4.9 Conclusions

Our work shows that different nanoscale aggregate geometries can be used to avail the vast diversities in the excitonic properties of 2D aggregates. Excitonic band structure of such aggregates can be experimentally probed using temperature dependent spectroscopy, which forms a comprehensive tool, relating specific experimental observables to distinct aspects of the excitonic band structure. We show temperature dependence studies of six 2D aggregates where carefully chosen dyes with varying brick lengths and central position substitutions afford the different aggregate geometries. Different nearest neighbor coupling curves could be realized with charge-transfer interactions (e.g. donor acceptor molecules).[27,113]

Photophysical properties are highly dependent on the position of bright state within the DOS. J-aggregates, with a band edge bright state, are known to have high quantum yields and superradiance rates,[12,38,79] making them applicable in several areas such as shortwave infrared imaging,[69,175] polaritonics,[148] and telecommunications.[66] J-aggregates have also been shown to exhibit fast picosecond FRET, serving as efficient antennas and bridges for energy transfer.[46,47] I-aggregates on the other hand have low quantum yields. Yet, the mid band bright state can exhibit collective oscillations of transition dipoles, enabling fast energy or charge transfer in the near-field.[136,145] Supramolecular tunability of the excitonic band structure, demonstrated here, will

therefore have exciting implications in several fields including shortwave infrared imaging, excitonic energy transfer, polaritonics, and plexitonics.[51,157]

4.10 Experimental methods

Materials: All dyes were obtained from FEW chemicals GmbH (catalog # S0046, S2278, S2275, S2284, S2433 and S0837 for TDBC, Cy3-Et, Cy3-H, Cy5-Ph, Cy7-Ph and Cy7-DPA respectively). Sodium chloride, sucrose, D-(+)-trehalose and methanol were obtained from Thermo Fisher Scientific. Milli-Q water (18 MΩ) was used for preparation of the aggregate samples. All materials were used as obtained without any further purification.

Preparation of aggregate solutions: All aggregates were prepared using a previously reported method of independent control of different solvation conditions.[186] A dye monomer solution of appropriate concentration was prepared in methanol, followed by injection into Milli-Q water or aqueous NaCl with a desired concentration. For specific mixing ratios (20% MeOH or 30% MeOH), the concentration of starting solution was adjusted appropriately. Solutions were allowed to equilibrate in the dark for 24 h prior to measurement. Glass vials as well as cuvettes used for all aggregates were pre-soaked in Milli-Q water. Following list shows specific final conditions for each aggregate.

TDBC: 0.2 mM dye, 20% MeOH

Cy3-Et: 0.5 mM dye, 20% MeOH, 0.05 M NaCl

Cy3-H[a]: 0.2 mM dye, 20% MeOH, 0.04 M NaCl

Cy5-Ph: 0.8 mM dye, 30% MeOH, 0.08 M NaCl

Cy7-Ph: 0.2 mM dye, 20% MeOH

Cy7-DPA: 0.2 mM dye, 20% MeOH

[a]Cy3-H aggregate was found to precipitate out of the solution over < 1 week, possibly due to air sensitivity. All solution samples were used within 48 h of preparation.

Sugar matrix stabilization: Saturated sugar solution made by dissolving a 50:50 sucrose/trehalose (w/w) in distilled water, followed by rigorous vortexing for a few minutes to ensure saturation.[81] 100 μL of equilibrated aggregate solution (after 24 h storing step) was deposited into a glass vial pre-soaked in Milli-Q water. To this, 100 μL of the sugar solution was added drop-wise and gently mixed while shielded from light. The sugar-aggregate mixture was dropped onto a 0.2 mm quartz cuvette from Starna Cells Inc. (also pre-soaked in Milli-Q water) and kept under vacuum in the dark for 24 h.

Room temperature absorption, emission, and quantum yield measurements: Absorption spectra were collected on a JASCO V-770 UV-Visible/NIR spectrophotometer and JASCO V-730 UV-Visible/NIR with a 2000 nm/min scan rate after blanking with the appropriate solvent. Photoluminescence spectra were obtained on a Horiba Instruments PTI QM-400 equipped with a liquid nitrogen cooled InGaAs detector for SWIR. Quartz cuvettes (2 x 10 mm path length) were used for room temperature absorbance and photoluminescence measurements.

Quantum yield (Φ_F) is defined as $\Phi_F = \frac{P_E}{P_A}$, where P_E and P_A represent the number of photons emitted and absorbed, respectively. Absolute quantum yields were determined in a Horiba petite integrating sphere for all compounds. To determine absolute quantum yield, the number of photons absorbed and emitted are measured independently. The emission background for the blank was normalized by the transmission ratio of the blank and sample at the excitation line. Quantum yield was calculated via FelixGX software provided by Horiba Instruments. Error was taken as the

standard deviation of three independent replicates. For monomers, sample optical density was kept below 0.1 to avoid fluorescence quenching and reabsorption effects. Since aggregate formation is concentration sensitive, aggregate samples had OD > 1 further complicated by the small Stokes shift which lead to reabsorption of emitted light from the fluorophore. Both of these effects were corrected in post processing, using previously derived correction factor with relevant modifications for our cuvette path length (2 x 10 mm).[194] In some cases (Cy3-Et monomer and Cy5-Ph aggregate), the quantum yields were too low to be reliably measured in the integrating sphere, so relative quantum yields were measured according to established protocol.[195] The standards used were commercial indocyanine dye Cy3[196] and Cy7-Ph monomer (this work) for Cy3-Et monomer and Cy5-Ph aggregate respectively.

Temperature dependent spectroscopy: Temperature dependent absorption measurements were performed using a Shimadzu UV/Vis/NIR spectrometer (SWIR samples) or Agilent Cary-60 spectrometer (Vis/NIR) samples. Dried sugar matrix samples were loaded inside Janis ST-100 cryostat using a custom built copper cuvette holder and cooled with liquid nitrogen. Cryostat was mounted inside commercial spectrometers with the help of custom-machined Al mounts. Lakeshore 330 Autotuning Temperature Controller was used to control the temperature. CAD files of all custom built parts are available upon request. For temperature dependent emission spectra, home-built setup equipped with Thorlabs CPS series lasers (532 nm for all Cy3 aggregates and 650 nm for Cy5-Ph), longpass filters of appropriate wavelengths (550 nm for all Cy3 aggregates and 695 nm for Cy5-Ph) and a Ag parabolic mirror were used for collection. The collected emission was fiber coupled into a Flame Ocean Optics spectrometer using a reflective collimator. Cryostat was mounted on an XY stage using custom built Al plates. All emission spectra were corrected for Jacobian conversion factor from wavelength to wavenumber scale. In some cases

where emission spectra were noisy, appropriate functions were used to get the best fit. FWHM and peak positions were extracted numerically from interpolated or fitted spectra in all cases. Estimates of temperature error of ± 2 K were shown on all power law graphs. Actual temperature fluctuations were across all measurements were less than ± 0.5 K.

Lifetime measurements Lifetimes were recorded at room temperature using a homebuilt, all-reflective epifluorescence setup.[197] The dye solutions were excited via a pulsed laser output from a 532 nm pulsed diode laser (LDH-P-FA-530B, PicoQuant) with 80 MHz repetition rates and 30 s acquisition times with excitation powers ranging from 11 nW to 3.76 μW depending on the samples. The emission was subsequently filtered with a 90:10 beam splitter [BSX10R, Thorlabs], various long pass filters and hot mirror [10CLVR-1, Newport], and detected by avalanch photodiodes (PD050-CTD, Micro Photon Devices). Time-correlated single photon counting (TCSPC) traces were histogrammed using a Picoquant HydraHarp 400 and analyzed via the corresponding software.

To determine the lifetime of TCSPC traces, we fitted the TCSPC histograms to a numerical convolution of the instrument response function (IRF) with biexponentials. The IRF was determined based on back-scatter from a cuvette with water (for all aggregate samples), and methanol (for all monomer samples), and fitted to an arbitrary function (convolution of a Gaussian and exponential) to get an analytical form. MATLAB code for the fitting is available upon request.

Cryo-electron microscopy (CryoEM): CryoEM of Cy3-H was obtained using a previously established protocol. We direct the readers to our previous work for the protocol and the cryoEM micrographs of rest of the aggregates studied here.[186]

4.11 Supporting experimental results

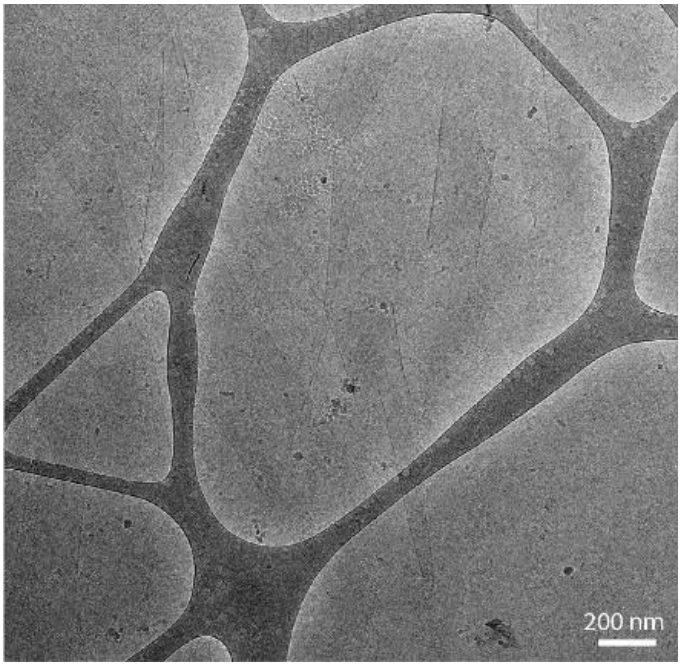

Figure 4.6 CryoEM image of Cy3-H J-aggregate showing 2D morphology.
Readers are directed to ref. 1 for cryoEM images of rest of the aggregates.

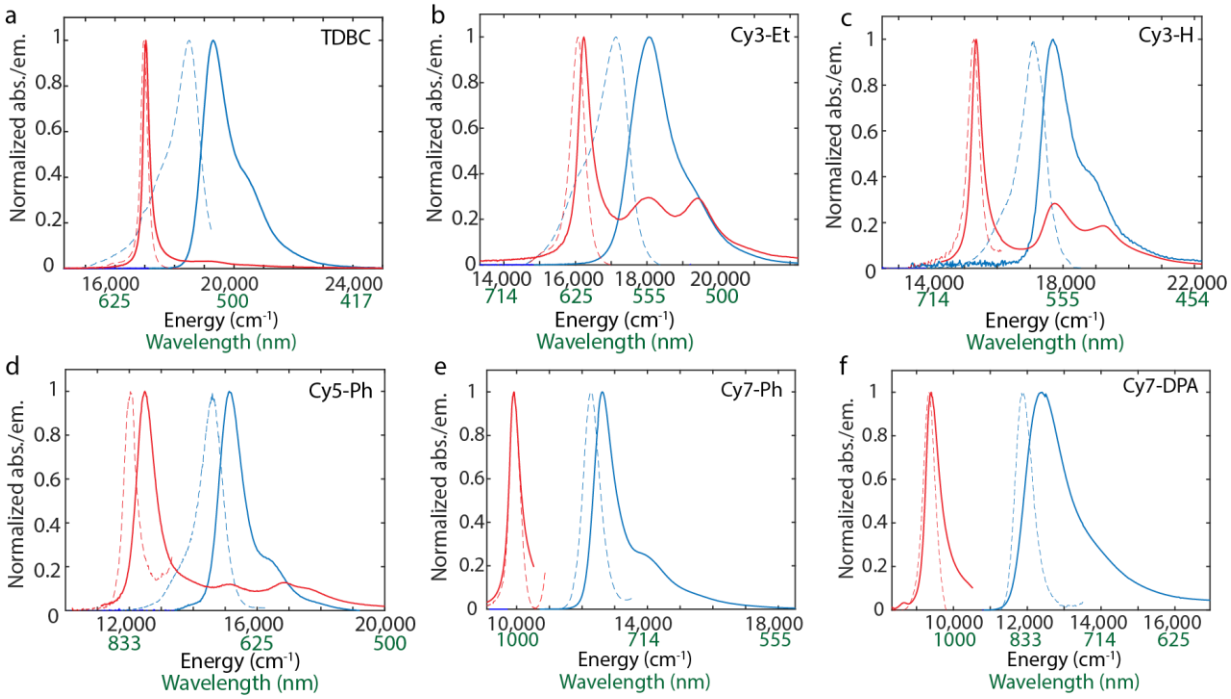

Figure 4.7 Room temperature solution UV-vis spectroscopy of all the six monomers and aggregates

Normalized absorption (solid lines) and normalized emission (dashed lines) of monomers (blue) and aggregates (red) a. TDBC (reproduced from main text), b. Cy3-Et, c. Cy3-H, d. Cy5-Ph, e. Cy7-Ph, and f. Cy7-DPA.

Table 4.3 Lifetime data of all emissive aggregates and all monomers.

Lifetimes are obtained from time correlated single photon counting using a biexponential fit. Instrument response function was numerically convolved in the fitting function.

Sample	a_1 **(%)**	a_2 **(%)**	τ_1 **(ps)**	τ_2 **(ps)**	τ_{avg} **(ps)**
TDBC monomer	98	2	78	462	80
TDBC aggregate	97	3	147	576	150
Cy3-Et monomer	93	7	56	388	60
Cy3-Et aggregate	93	7	185	598	195
Cy3-H monomer	83	17	243	536	268

Cy3-H aggregate	94	6	197	1049	207
Cy5-Ph monomer	84	16	426	935	467
Cy5-Ph aggregate	69	31	178	649	229
Cy7-Ph monomer	51	49	262	987	410
Cy7-DPA monomer	73	27	710	268	637

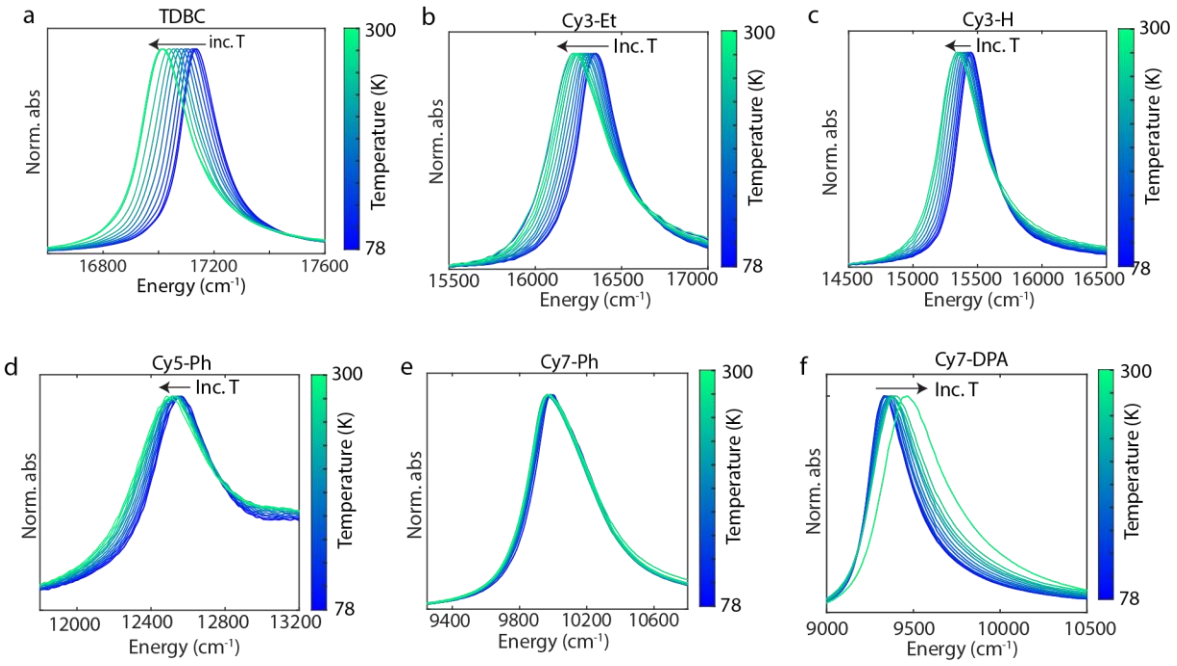

Figure 4.8 Normalized temperature dependent absorption spectra of all sugar matrix stabilized aggregates from 78 K (blue) to 300 K (green)

a. TDBC (reproduced from earlier), b. Cy3-Et, c. Cy3-H, d. Cy5-Ph, e. Cy7-Ph, and f. Cy7-DPA.

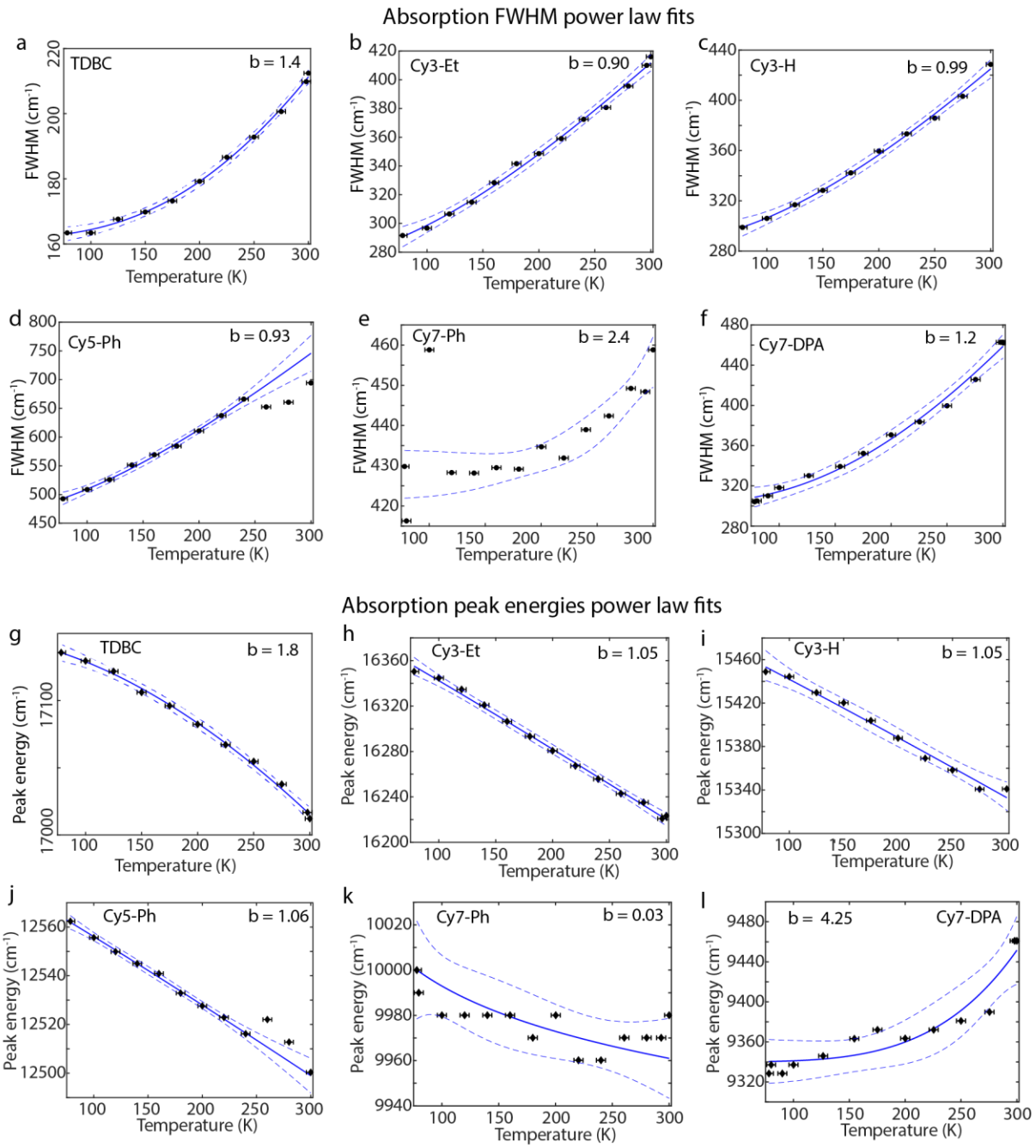

Figure 4.9 Temperature dependent absorption power laws for all the 2D aggregates.

a-f. FWHM (circles), (solid line) power law fits using eq. (4.3) and 95% prediction interval (dashed lines) of the fits for a. TDBC (reproduced from main text), b. Cy3-Et, c. Cy3-H, d. Cy5-Ph, e. Cy7-Ph, and f. Cy7-DPA. The data point on part e near 460 cm^{-1} is an outlier, the distance is artificially enhanced due to the short scale. g-l. Absorption peak energies (diamonds), power law fits using eq. (4.4) in main text (solid line) and 95% prediction interval (dashed lines) of the fits for g. TDBC

(reproduced from main text), h. Cy3-Et, i. Cy3-H, j. Ch5-Ph, k. Cy7-Ph, and l. Cy7-DPA. Error bars are estimates of ± 2 K.

Justification for squared FWHM power laws

For linewidths, we use a modified form of the previously used power laws where the two terms are added in quadrature according to eq. (4.3). We justify this on the basis of the lineshapes described by Voight functions, where a temperature dependent Lorentzian representing homogeneous disorder is convolved with a temperature independent Gaussian (inhomogeneous disorder).[117] The widths of both components are added in quadrature in the convolved function with the Lorentzian part being the dominant contribution in the studied temperature range. This captures the full range of temperature dependent behavior. In the high temperature limit, the *b* parameter from eq. (4.3) can be directly compared to previous power laws. Interpreting the power laws for mid-band I-aggregates is more complicated as the lineshapes may be dominated by multiple processes including relaxation to the band-edge.[145]

Table 4.4 Temperature dependent emission power law fit parameters.
from main text eq. (4.3) and (4.4) for FWHM and peak energies respectively.

Dye	**Power law for FWHM (*b*)**	**Power law for peak energies (*b*)**	**Peak shift with increasing temperature**
TDBC	1.0 ± 0.2	1.3 ± 0.3	Red
Cy3-Et	1.7 ± 0.6	0.9 ± 0.8	Red
Cy3-H	1.3 ± 0.5	2.4 ± 0.6	Red
Cy5-Ph	1.4 ± 0.2	1.4 ± 1.2	Red

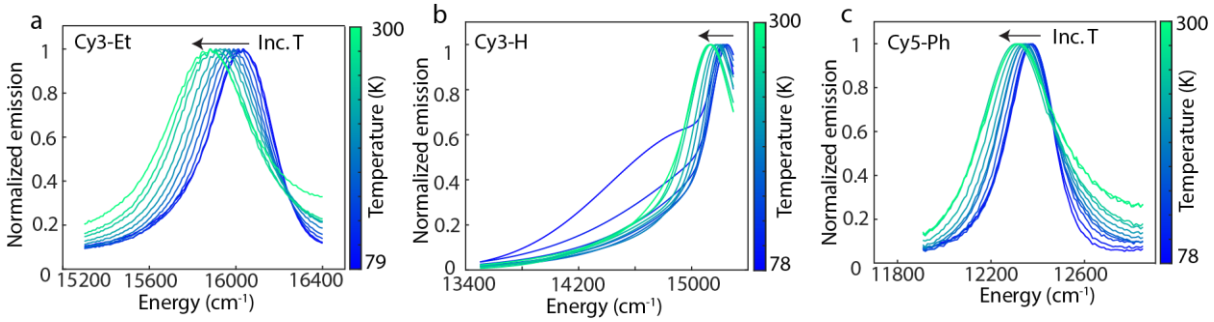

Figure 4.10 Normalized temperature dependent emission spectra of red shifting 2D aggregates.

a. Cy3-Et, b. Cy3-H, c. Cy5-Ph.

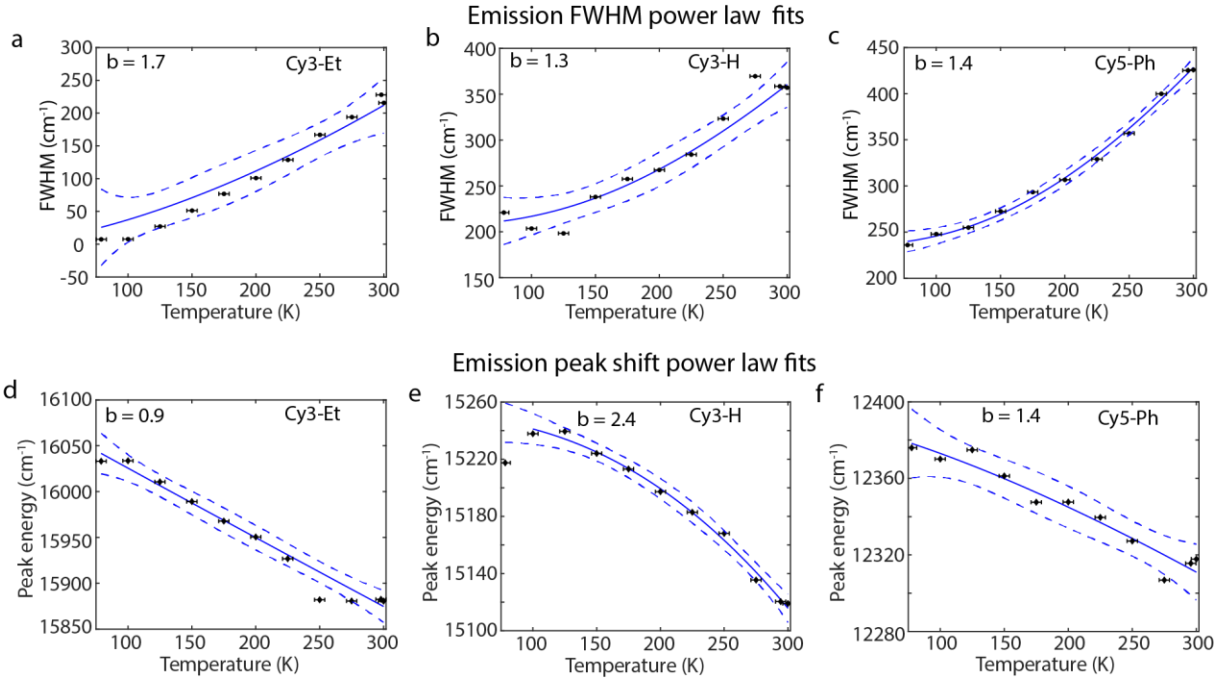

Figure 4.11 Temperature dependent emission data for all *the* band edge 2D aggregates.

a-c. FWHM (circles), power law fits using eq. (3) in main text (solid line) and 95% prediction interval (dashed lines) of the fits for a. Cy3-Et, b. Cy3-H, c. Cy5-Ph. Emission peak energies (diamonds), power law fits using eq. (4) in main text (solid line) and 95% prediction interval (dashed lines) of the fits for c. Cy3-Et, d. Cy3-H, e. Cy5-Ph. Error bars are estimates of ± 2 K.

Derivation of power laws for temperature dependent peak shifts

It is assumed that the exciton-phonon coupling is perturbative and that the environmental degrees of freedom relax faster than those of the systems such that a Markovian Redfield treatment is justified. The detailed derivation leading to this point can be found in previous works.[128,163]

We start with the Markovian lineshape operator in the system energy eigenbasis in the time domain

$$K(t) = \sum_{k=1}^{N} |k\rangle\langle k| \left(\Gamma_k^{\mathrm{pd}} + \sum_{l \neq k}^{N} \Gamma_{kl}^{\mathrm{rd}} \right) t$$

here $|k\rangle$ is the *k*th energy eigenstate of total *N* excitonic molecules, Γ_k^{pd} is the pure dephasing rate, and $\Gamma_{kl}^{\mathrm{rd}}$ is the dephasing rate induced by the population transfer from states *l* to *k*. For strongly delocalized excitonic aggregates $\Gamma_{kl}^{\mathrm{rd}}$ is the dominating contribution, and it takes the following form under the Markovian Redfield approximation:

$$\Gamma_{kl}^{\mathrm{rd}} = \frac{1}{N} \left\{ \frac{J(\omega_{kl})}{e^{\omega_{kl}/T} - 1} + i \frac{1}{\pi} \mathrm{p.\,v.} \int_0^{\infty} d\omega\, J(\omega) \left[\frac{2\omega_{kl}}{(\omega^2 - \omega_{kl}^2)(e^{\omega/T} - 1)} + \frac{1}{\omega - \omega_{kl}} \right] \right\}$$

where $J(x)$ is the bath spectral density, T is the temperature, and p. v. stands for Cauchy principal value of the following integral. We have taken $\hbar = 1$ for brevity. The real part of this expression gives the homogeneous part of the spectral width and the imaginary part describes the peak shift of the line shape.

In most cases we are interested in the bright state (ω_b), such that exciton density of state near the bright state can be cast into a power-law scaling form $D(\omega) = (\omega - \omega_b)^d$. For example, it is

well known that $d = -0.5, 0, 0.5$ for 1D, 2D, 3D nearest-neighbor coupled square lattices, respectively. Again, in the large aggregate limit, we replace the summation over *l* by an integral

$$K(t) \approx t \cdot (W_b + iS_b)$$

$$W_b = \int_0^\infty d\omega \, \frac{\omega^d J(\omega)}{e^{\omega/T} - 1}$$

$$S_b = \frac{2}{\pi} \text{p. v.} \int_0^\infty d\omega \int_0^\infty d\omega' \, \omega^d J(\omega') \left[\frac{\omega}{(\omega^2 - \omega'^2)(e^{\omega'/T} - 1)} + \frac{1}{\omega - \omega'} \right]$$

Following Heijs et al.,[189] we take the spectral density to be of the form $J(x) = \lambda x^s \theta(\omega_c - x)$ where λ and ω_c are constants and $\theta(x)$ is the Heaviside function. In the fast bath limit, i.e. $\omega_c/T \gg 1$, one arrives at the power-law temperature scaling of the spectral width

$$W_b = T^{d+s+1} \int_0^{\omega_c/T} dx \, \frac{x^{d+s}}{e^x - 1} \approx T^{d+s+1} \int_0^\infty dx \, \frac{x^{d+s}}{e^x - 1} \propto T^{d+s+1}$$

The spectral shift is slightly more involved but can be similarly derived

$$S_b(T) - S_b(0) = \frac{1}{\pi} \text{p. v.} \int_0^{J_c} d\omega \int_0^{\omega_c} d\omega' \, \frac{\omega^{d+1} \omega'^s}{(\omega^2 - \omega'^2)\left(e^{\frac{\omega'}{T}} - 1\right)}$$

$$= T^{d+s+1} \cdot \frac{1}{\pi} \text{p. v.} \int_0^{J_c/T} dx \int_0^{\omega_c/T} dx' \, \frac{x^d x'^s}{(x^2 - x'^2)(e^{x'} - 1)} \propto T^{d+s+1}$$

with additional assumptions that the system density of state scales as $(\omega - \omega_b)^d$ up to $J_c \gg T$, and that the principal value exists, both hold for all cases covered in our study.

4.12 Computational methods and supporting model results

We use the brick layer model with a Frenkel exciton Hamiltonian to relate the observed differences in the band structures to the molecular packing geometries. In Figure 4.12a, we outline our approach of computationally modeling the band structures for a specific aggregate packing geometry afforded by each dye structure. Following convention, we approximate the dye molecule extent as a brick with specified widths and length (*L*) and tile the bricks with a slip *s* (vertical offset between adjacent bricks).[29] The brick widths were kept constant as we do not expect π–π stacking distances to vary across the current dataset.

The procedure is summarized as follows: We start with a geometry optimization for a single monomer, followed by calculation of coupling curves with respect to slip for a dimer using transition charge (TC) densities where each atom within the dye molecule is assigned a partial charge. The TC coupling curves for all aggregates are shown in Figure 4.12b. An extended dipole model coupling curve is then to fit the TC curve (Figure 4.12c), obtaining effective extended dipole lengths and charges for the dyes (Table 4.5).[29] These dipoles are then embedded in a large 2D lattice, followed by the Frenkel exciton Hamiltonian to calculate the DOS of the extended 2D aggregates.

ZINDO Transition charge dimer model

Dyes were prepared for Zindo calculations by replacing Cl atoms with F atoms and truncating the sulfonate side chains at methyl groups. The geometry of each dye was then optimized by UFF to its planar form. The ZINDO $S_0 \rightarrow S_1$ transition density was calculated.[142] For constructing the TC dimer model, a second dye was positioned 4.0 Å along the vector perpendicular to the plane of the molecule, with a slip vector parallel to the Cl-Cl vector of the molecule. The coupling curve

at many slip values was then calculated from the transition charge densities. An extended dipole coupling function is then fit to the transition charges coupling curve,

$$J_{ext}(r_n - r_m) = \frac{\mu^2}{d}\left(\frac{1}{r_{m+,n+}} + \frac{1}{r_{m-,n-}} - \frac{1}{r_{m-,n+}} - \frac{1}{r_{m+,n-}}\right)$$

where μ is the effective dipole strength, d is the charge separation distance, and $r_{nm} = r_n - r_m$, the $\pm$ subscripts denote the 'extended charges within each brick segment. For full detailed description of the brick set up, please see our previous work of the subject.[145] As shown in Figure 4.12b the extended dipole provides a significantly better fit to atomistic transition charges coupling. The brick length for all bricks was taken to be the 5-5' position Cl-Cl distance on the optimized dye geometry with an additional 2 Å of buffer space added, while the short length of the brick was set to 4 Å for all dyes, approximately the average $\pi - \pi$ stacking distance for the aromatic heterocycles. As shown in Table 4.5, the final dipole strengths for the model were rescaled to be proportional monomer solution dipoles. We find that ZINDO dramatically overestimates the transition dipole in cyanine dyes but rescaling to the measured monomer transition dipole strength led to a total monomer to aggregate shift consistent with the experimental spectra without need for an effective aggregate dielectric.

Extraction of the H/I/J Regions of the Hamiltonian

The disorder free, $\delta_i = 0$, Frenkel Exciton Hamiltonian can be diagonalized Bloch waves.

$$H_{FE} = \sum_i (E_0 + \delta_i)|i\rangle\langle i| + \sum_{ij} J_{ext}(r_i - r_j)|i\rangle\langle j|$$

Thus, to simply extract the H/I/J regions of each fit model, we can set $E_0 \to 0$ without loss of generality, construct the coupling matrix J_{ext} and diagonalize via 2D FFT. All calculations were

done on aggregates of size $N_x = N_y = 405$, beyond the need for the method of images to impose boundary conditions on the aggregate. The k = 0 bright state is then calculated as the sum of the coupling matrix J_{ext}. Representations of these regions can be seen in main text Figure 4.12d-f.

We observe significant differences in the slip dependent properties of the excitonic band structure depending on the coupling model as well as the aggregate packing geometry. We show in Figures 4.12d-f the bandwidth and position of $k = 0$ bright state as a function of slip for zero disorder point dipole and extended dipole models of TDBC. The use of an extended dipole model opens up a larger range of slips which show I-aggregate behavior. We attribute this to the point dipole model that shows a steeper slip dependence and therefore, results in a very small I-aggregate region (Figure 4.12d). Further, the slip dependence for Cy7-DPA (Figure 4.12f) shows the effect of longer brick length, where again the possible slip range for I-aggregation is expanded. This is the result of increased positive contributions to the short-range couplings due to longer molecular species.[198] The total band width of the excitonic DOS is bounded by twice the absolute value of the net coupling which has a minimum at zero i.e. when it changes sign from positive to negative. As a result, the bandwidth is minimized around the boundary between I- and J-aggregate regions on Figures 4.12d-f.

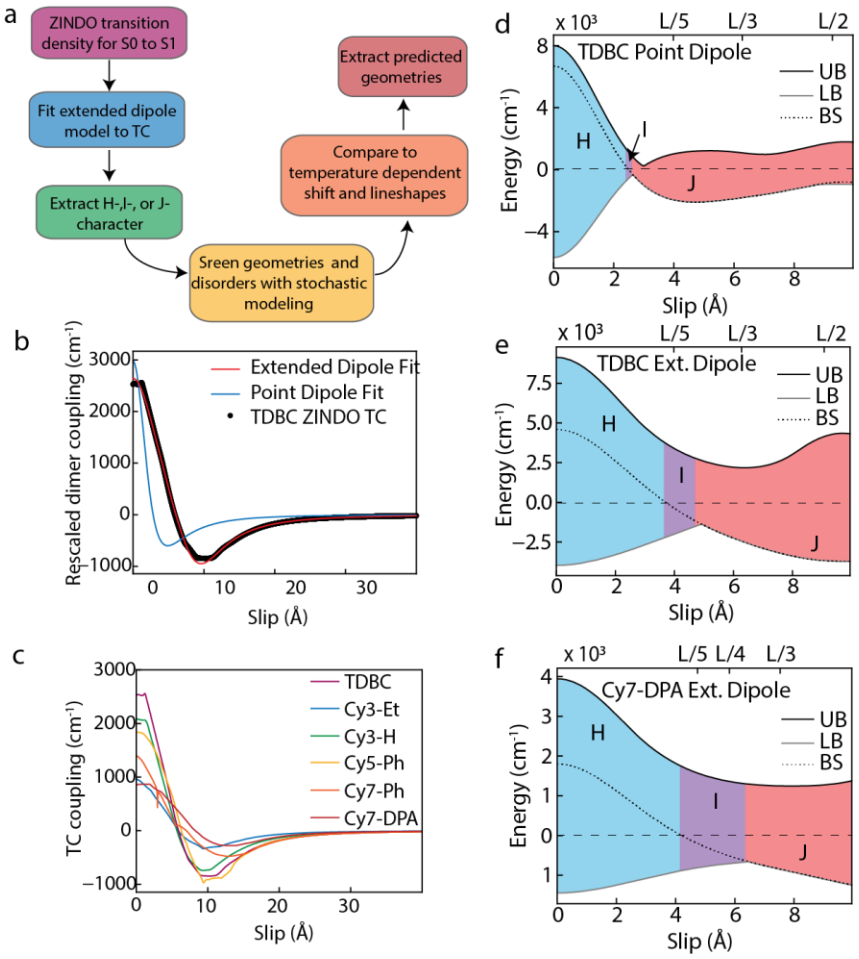

Figure 4.12 Modeling the excitonic band structures of 2D aggregates – methodology and supporting results

a. Flow chart describing the stochastic modeling approach, b. TDBC ZINDO transition charges coupling curve (black), shown with the fits of the extended dipole Hamiltonian (red) and the point dipole Hamiltonian (blue). The fit parameters for the extended dipole models are shown in Table S1. The fit magnitude of the point dipole for TDBC was 4.6 D. c. Slip dependent coupling curves for dimers of all dyes calculated from the transition charges (TC), d-f. Slip dependent behavior of the band structure– upper band edge (UB, black line), lower band edge (LB, grey line) and bright state (BS, dotted line) with H-, I- and J-aggregation regions color coded as blue, purple and red respectively for 2D aggregates of d. TDBC using point dipole model, e. TDBC using extended dipole model, f. Cy7-DPA using extended dipole model. Dashed lines indicate monomer energy and dotted lines indicate the bright state.

Table 4.5. Summary of the parameters used in the model for calculating excionic DOS and for screening aggregate slips - disorder values.

Brick lengths for each aggregate estimated from geometry optimized structure, ZINDO calculation results – transition dipole moment and it's ratio to experimental dipole moment calculated from eq. (4.2), extended dipole charge separations and magnitudes from fitting the TC coupling curves. Finally, the 0 K extrapolated FWHM obtained from temperature dependence i.e. parameter *c* in main text eq. (4.3).

Dye	**Cl-Cl distance (Å)**	**ZINDO transition dipole moment (D)**	**ZINDO/ Expt. Dipole ratio**	**Fit charge separation distance (Å)**	**Ext. Model Dipoles scaled dipole (D)**	**0 K FWHM (cm^{-1})**
TDBC	17.35	53.56	4.12	4.3	2.80	161 ± 2
Cy3-Et	16.84	51.16	10.23	4.4	1.70	276 ± 11
Cy3-H	16.78	51.50	5.15	4.1	2.50	286 ± 10
Cy5-Ph	18.89	60.73	5.06	4.8	2.60	464 ± 20
Cy7-Ph	21.76	75.39	6.56	5.4	2.00	428 ± 3
Cy7-DPA	21.64	69.01	9.86	6.3	1.80	302 ± 10

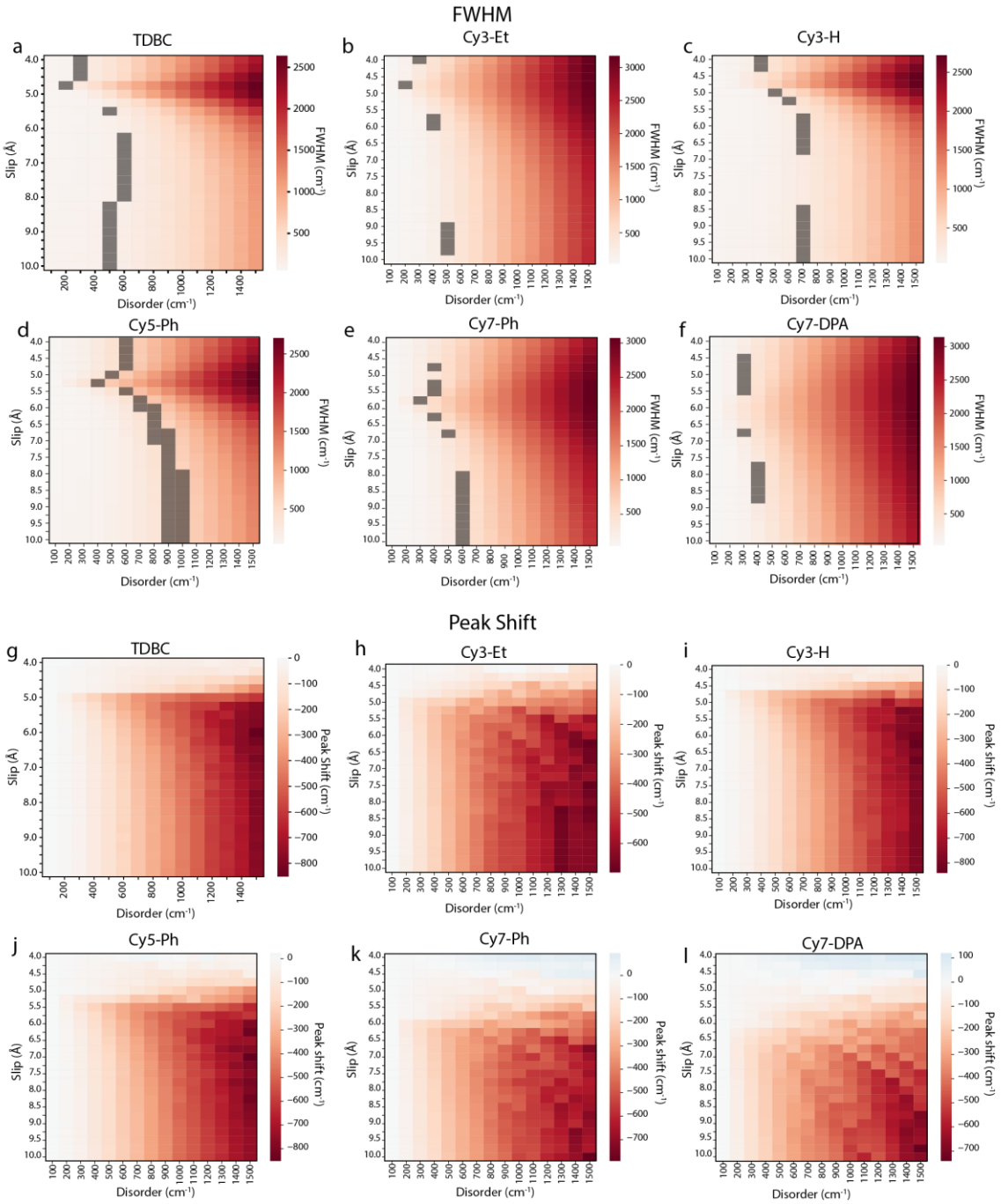

Figure 4.13 Screens of slips and disorder values using stochastic approach for all the 2D aggregates.

a-f, predicted FWHM values, and g-l predicted peak shifts relative to the zero disorder case for all aggregates at 0 K. Grey squares on FWHM screens denote parameters narrowed down by mean-square error fitting with respect to 0 K FWHM obtained from power law fits given in Table 4.5.

Rapid screening of disorder and slip conditions

Leveraging a recent stochastic wave function based method to efficiently extract the DOS and absorption of the Hamiltonian, slip and disorder is screened for all dye models.[178] We found that at a 4 cm^{-1} resolution of the DOS and k=0 absorption, only twelve stochastic wave functions and disorder realizations were necessary to produce the fully resolved spectra. Results from various aggregate geometry and disorder screens are shown in Figure 4.13. For specific slip and disorder values determined by a mean-square error comparison to 0 K FWHM obtained from the experimental power law fits, we narrow down the large parameter space to the grey squares. Excitonic DOS and absorption spectra for a given geometry (slip or brick length) and disorder value can be calculated using this method and are shown in Figure 4.5.

Chapter 5

Near-Atomic Resolution Structure of a Helical Tubular J-aggregate

In the previous chapter, we discussed the importance of nanoscale molecular arrangements towards excitonic properties of molecular aggregates. Currently, nanoscale structural information is obtained from models that are indirectly validated by fitting the optical spectra. Due the lack of a high resolution structure, such spectral assignments become ambiguous. Several explanations have been put forth for describing the molecular origins of the complex optical lineshapes as well as chiral signatures observed in circular and linear dichroism spectra. We address this challenge in the current chapter with first high-resolution structure of a model excitonic system – light harvesting nanotubes (LHNs). Moreover, a high resolution structure will also provide into the self-assembly process that will enable improved supramolecular design of such systems.

5.1 Light harvesting nanotubes – a model excitonic system

Amphiphilic cyanine dyes with long alkyl chain substituents were first reported in 1995 by Dähne and co-workers.[199] A commonly studied model system in this class is the dye 3,3′-bis(3-sulfopropyl)-5,5′,6,6′-tetrachloro-1,1′-dioctylbenzimidacarbocyanine or C8S3-Cl (Figure 5.1a inset), which is known to aggregate into tubular morphologies such as double-walled nanotubes or bundles.[200] The double-walled nanotubes, also known as light harvesting nanotubes (LHNs) have been shown to behave like a model excitonic system with robust micron scale exciton transport at room temperature.[81,88,164] Previous work has also shown that the excitonic band structure of LHNs is similar to Kasha's J-aggregate with a band-edge bright state.[79] Furthermore, the amount of

exciton delocalization in these systems can be photochemically controlled, as evidenced from photobrightening and photodarkening experiments.[79] LHNs also possess chiral signatures observed using circular and linear dichroism (CD and LD respectively) studies, though the origin of chirality is an open question as the starting monomers are achiral.[173,201–204] Over the decades, the LHNs have emerged as a prototypical tubular molecular aggregate system, with a number of spectroscopic as well as structural investigations.

Polar organic solvents such as methanol stabilize the monomeric form of C8S3-Cl with an absorption peak at 523 nm. Upon injecting the monomer solution in water with 30% MeOH (v/v) ratio, the dye self-assembles into light harvesting nanotubes (LHNs) with an immediate color change from red to magenta. Figure 5.1a shows the absorption spectra of C8S3-Cl monomer and aggregated LHNs. Figure 5.1b is a cryoEM micrograph of the LHNs showing a double walled nanotube morphology. Absorption spectrum of the LHNs features peculiar excitonic features with two sharp lines at 589 and 599 nm along and several shoulder peaks at higher energies. Previous studies assigned the two sharp peaks at 589 and 599 nm to polarization of excitons along the tube axis of outer and inner walls respectively and are therefore called as outer wall parallel ($OW_{\parallel}$) and inner wall parallel ($IW_{\parallel}$) peaks.[77,202] On the other hand, polarization along the circumference of the cylinders results in several broader shoulder peaks higher energy, labelled as $OW_{\perp}$ and $IW_{\perp}$ peaks in Figure 5.1a.

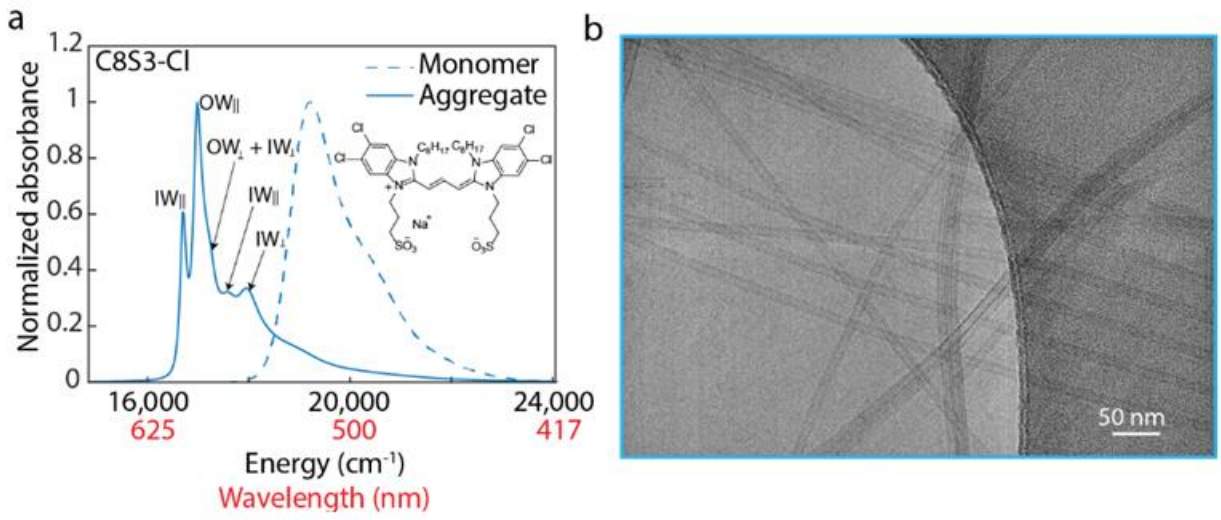

Figure 5.1 Light harvesting nanotubes (LHN) cryoEM and 3D

a. Absorption spectra of C8S3-Cl monomer (dashed) and J-aggregated light harvesting nanotubes (LHNs) in solid line. Structure of C8S3-Cl dye in inset, b. Representative cryoEM micrograph of LHNs showing double-walled nanotubular morphology.

5.2 Structure of LHNs

Structural origin of these excitonic features in LHNs has puzzled experimentalists and theorists alike. Excitonic coupling in the LHNs and other higher dimensional molecular aggregates are highly sensitive to the precise molecular geometries as well as disorder. A thorough understanding of the relations between the two will be instrumental in chemically modulating exciton transport in such systems. However, unraveling the atomic level structure of these systems has been a challenge as these are inherently soft materials, sensitive to their environments. Common structure determination techniques such as X-rays do not provide high enough resolution, and can often be destructive. Small-angle X-ray scattering (SAXS) also requires prior information from models to interpret the scattering curves.[205] A high resolution structure of the LHNs will help understand the driving forces for the self-assembly and eventually, allow chemists to engineer supramolecular systems with precise control over supramolecular packings. As we have seen in Chapter 4, these

supramolecular packing parameters can be ultimately used to tune the excitonic behaviors of the aggregates.

Table 5.1 shows a literature survey of structural studies on pristine LHNs, their methodology and key findings. Experimental probes such as cryo-electron tomography (cryoET) and redox chemistry were indeed valuable in uncovering a lot of mesoscale structure such as the double-walled nature of LHNs, twisted and straight bundle structures. Atomic force microscopy and near-field scanning optical microscopy revealed that the nanotubes indeed fluoresced uniformly along the whole tube, indicating a preserved supramolecular structure. However, more nanoscale structural details are still missing. Most of the nanoscale structural knowledge so far is from models or simulations that are validated by fitting to the optical spectra. But the inherent complexity of the excitonic spectra makes such assignments ambiguous.

One such ambiguity is whether the molecules are arranged in a brick layer type arrangement or herringbone-like arrangement. Frenkel exciton models with dipole treatment based on both of these geometries have been fit to optical spectra. While the brick layer model considers 1 molecule per unit cell, symmetry breaking observed even in the isolated inner wall spectra justified the herringbone model with 2 molecules per unit cell. Adding additional van der Waals or charge transfer nearest neighbor couplings can also complicate such spectral assignments. The sensitive nature of the self-assembly makes it difficult to preserve the solution-state molecular arrangement in experimentally relevant environments. Therefore, preservation of the original structure as well as high-resolution structure determination technique are two essential prerequisites for uncovering the nanoscale structure of LHNs unambiguously.

Table 5.1. A literature survey of different approaches taken so far to obtain the structure of LHNs.

Reference	Method used to obtain structural details	Key findings
Kirstein et al., 2000[201]	CryoEM micrographs CD spectroscopy	Chirality in bundled nanotubes of C8O3
Didraga et al. (Knoester), 2004[25]	Brick layer model informed by CD and LD CryoEM micrographs	CryoEM showed double-walled morphology of the tubes
Berlepsch et al., 2007[206]	CryoEM micrographs	Tubes formed rope-like bundles over weeks
Lyon et al. (Stevenson), 2008[207]	Cyclic voltammetry, optical spectroscopy and spectroelectrochemistry of immobilized LHNs on ITO	Initial oxidation of outer wall, followed by irreversible dehydrogenation and dimerization. Inner wall stayed relatively intact.
Eisele et a. (Rabe & Vanden Bout), 2009[164]	Atomic force microscopy and near-field scanning optical microscopy	The supramolecular structure was uniform within individual nanotubes as well as across an ensemble.
Berlepsch et al. (Bottcher), 2011[208]	CryoEM 3D reconstruction of mixed C8S3 and C8S2 tubes	2 nm resolution map with pitch angle of 17.3°
Eisele et al. (Knoester & Vanden Bout), 2012[77]	Redox chemistry Herringbone model fitted to absorption spectra	Excitonic decoupling of inner and outer wall Explains symmetry breaking in isolated spectra
Clark et al. (Vanden Bout), 2013[202]	Linear dichroism of double-walled nanotubes and photochemically isolated inner wall spectra	Total six transitions isolated for doubled-walled nanotubes (3 parallel and perpendicular pairs), 4 of which assigned to inner wall
Eisele et al. (Nicastro, Knoester & Bawendi), 2014[88]	Cryo-electron tomography of LHNs and bundles Herringbone model informed with absorption spectra	Hierarchical assembly of the LHNs with observations of straight and twisted bundles

Megow et al., 2015[209]	MD simulations with two molecules per unit cell in brick layer arrangement	Site dependent dispersive shifts due to van der Waals interactions explained the peak splitting
Kriete et al. (Pshenichnikov), 2017[210]	Replaced Cl atoms with Br Herringbone model fitted to absorption spectra	Br tubes were claimed to be wider than Cl Spectral differences were attributed to higher radius of Br tubes
Bondarenko et al. (Marrink & Knoester), 2020[211]	Multiscale modelling – MD (Herringbone arrangement), microelectrostatics and Frenkel exciton Hamiltonian, optimized with absorption spectra	Energetic and structural disorder, higher packing density in IW explained the spectral splitting
Patmanidis et al. (Marrink), 2020[205]	MD simulations (with brick layer, staircase and herringbone arrangements) Small-angle X-ray scattering	Brick layer and herringbone arrangements were plausible, brick layer being more stable Interdigitated alkyl chains led to reduced widths between the two walls

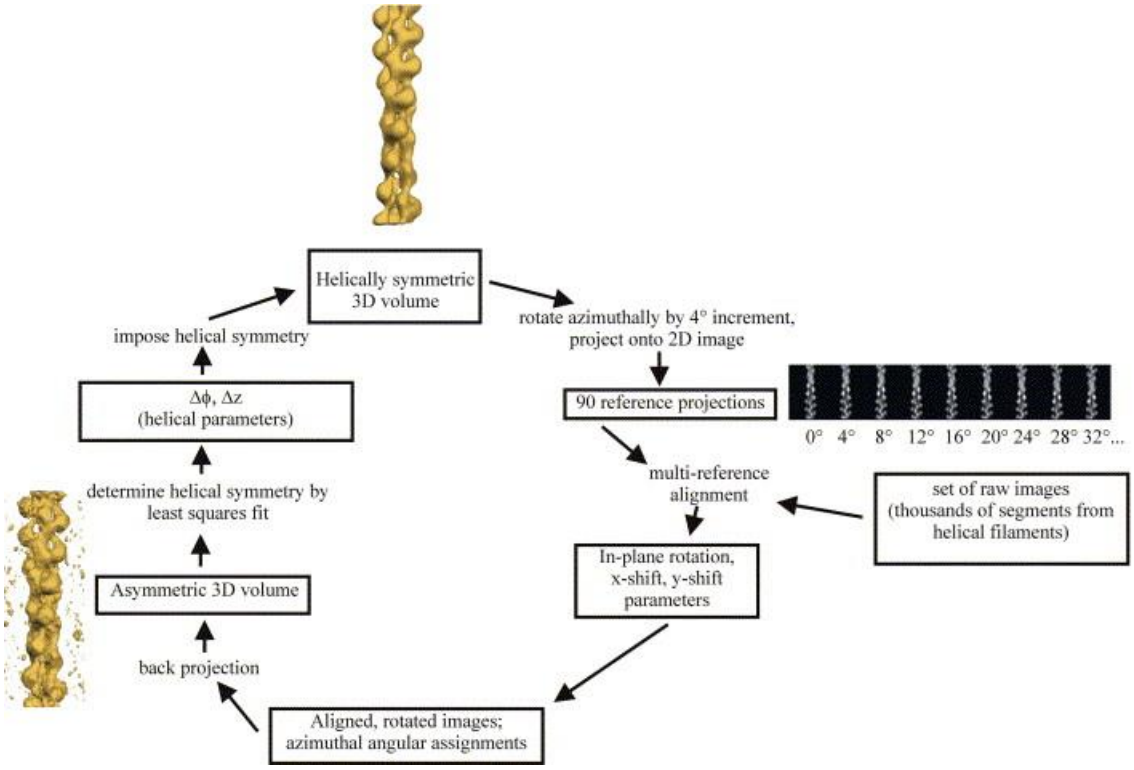

Figure 5.2 Schematic explaining the methodology of Iterative Helical Real Space Reconstruction (IHRSR)

Adapted from Egelman, 2007[212]

5.3 Iterative helical real space reconstruction (IHRSR)

We address such challenges with a cryo-electron microscopy (cryoEM) of vitrified LHN samples. Vitrification by plunge-freezing in liquid ethane is extensively used in biological assemblies to preserve the native structures and protect from beam damage.[213,214] Molecular aggregate assemblies are also hydrated soft structures like protein or lipid assemblies. Previous cryoEM and cryoET studies on LHNs used the vitrification technique to cryo-protect the samples.[45,88] Particularly, we use Iterative Helical Real Space Reconstruction (IHRSR) algorithm, developed by the Egelman in 2000, to computationally analyze the cryoEM images of vitrified LHNs.[212,215] IHRSR is designed for single-particle analysis of weakly diffracting disordered

helical polymers and is depicted in Figure 5.2.[216] Starting with initial reference 3D volume, the algorithm takes projections of several azimuthal rotations, followed by a cross-correlation with thousand or tens of thousands of segments obtained from cryoEM images of the sample. The best correlations yield the helical screw symmetry parameters – coupled azimuthal rotation and displacement along the tube axis ($\Delta\phi, \Delta z$ respectively). The aligned images are then back-projected to get a 3D volume, but with the information from the sample encoded in it. Then, it optimizes the new screw parameters $\Delta\phi, \Delta z$ that would fit symmetrized volume to the actual volume. These new parameters are then imposed on the next cycle until a minimum is reached iteratively. The general principle is quite similar to how most data fitting algorithms optimize fit parameters by minimizing mean square errors. One point to be noted is that, the IHRSR algorithm is independent of any starting reference volume and the right parameters are obtained even when you start from a solid cylinder with no structural features.[216] The ambiguity arises for the assignment of the helical hand. Though, it is actually inherent to any helical reconstruction technique with limited resolution and pertains to the peak assignments in the power spectra.[216,217]

5.4 CryoEM structure of LHNs

Figure 5.3a shows a power spectrum of the LHNs averaged from the power spectra of thousands of segments on the cryoEM micrographs. The meridian layer line (corresponding to n = 0 Bessel function) provides the helical rise of 9.9 Å. A striking feature in the power spectrum, we were able to see layer lines as far as 3.9 Å providing the first evidence of a high-resolution periodic structure

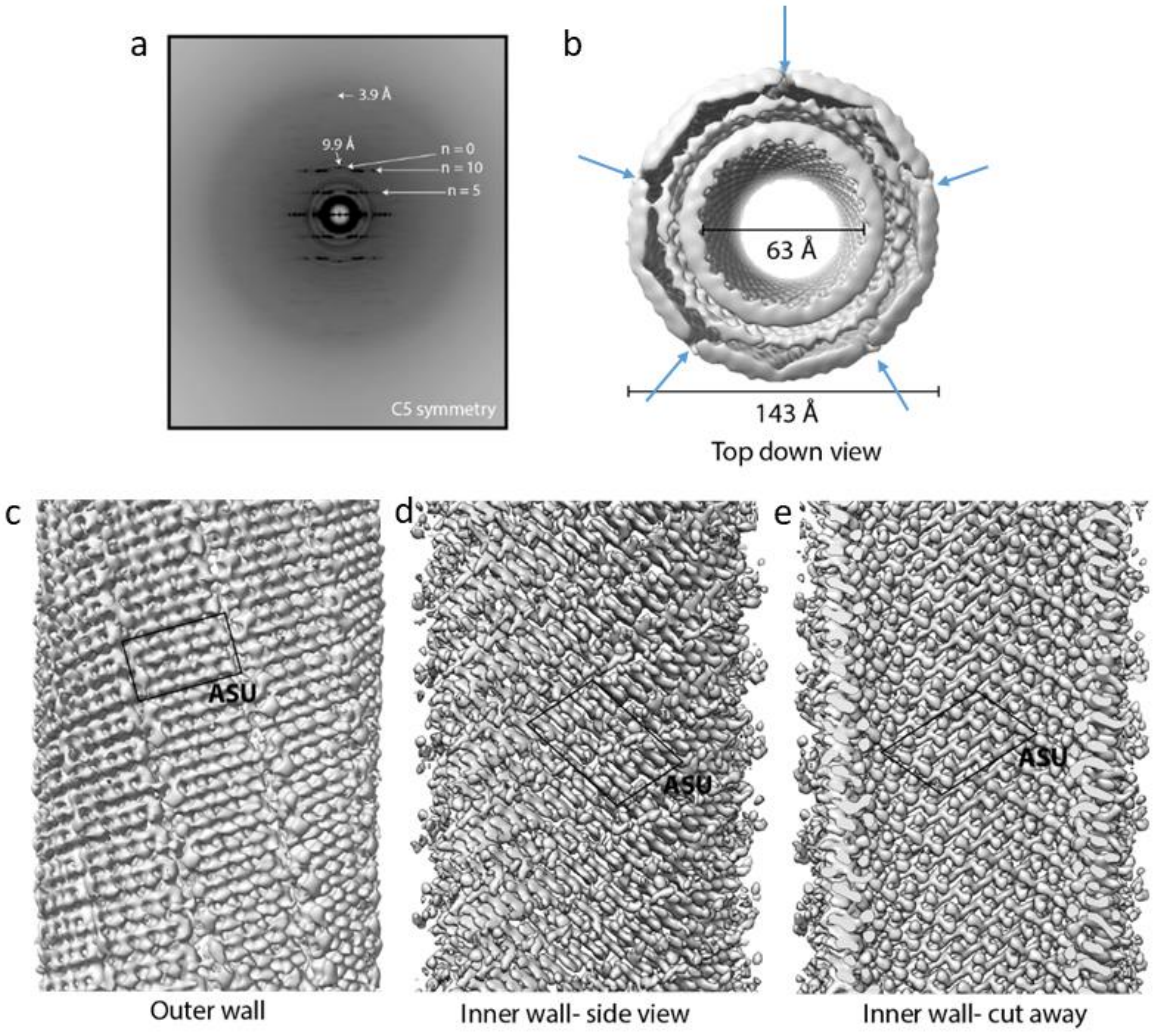

Figure 5.3 CryoEM reconstruction of LHNs from IHRSR

a. Power spectrum averaged from ~ 10^4 segments of LHNs, b. Top view of the double-walled nanotubes with diameters labelled and blue arrows indicating the groves, c. Side view of the outer wall density, d. Side view and e. Cut away view of the inner wall density.

in the LHNs, commonly thought of as disordered solution state assembly. Further, the observation of layer lines corresponding to Bessel functions of order n = 0, 5, 10 etc. indicates a possibility of C5 rotational symmetry besides the helical symmetry. We then use these parameters as starting points for the IHRSR algorithm and iteratively reconstruct the density maps for both outer and inner walls, shown in Figures 5.3b-e. We obtained a cryo-EM map at 3.3 Å, and the helical

symmetry converged with helical rise of 9.9 Å and twist of 33.6 °. The diameters of both inner and outer walls as shown in Figure 5.3b match previous reports within error.[77]

5.5 Molecular structure from 3D maps

The inner wall density was refined with a molecular model, an overlay of the two is shown in Figure 5.4. We first optimize the geometry of a dimer using Coot[218] followed by a refinement in PHENIX.[219] We observe excellent correlation between the molecular model and reconstructed density. The asymmetric unit (ASU) for inner wall comprises of 6 monomeric units (Figure 5.4c) while that for the outer wall has 8 monomeric units. Overall, the 14 unique monomeric environments collectively give rise to the excitonic features of the LHNs observed in Figure 1a. In the inner wall, 5 ASUs go around the circumference of the tube to complete a single turn (Figure 5.4d). Figures 5.4e-f show space filling models two segments (color coded magenta and cyan). This clearly shows that the symmetry breaking in the optical spectra arises, not from the Herringbone structure, but from the 6 monomer and 8 monomer ASUs for inner and outer wall respectively.

A crucial finding is that the molecules adopt a slip stacked arrangement, a signature of excitonic J-aggregates, albeit with a brick layer like formation as opposed to a herringbone-like structure that previous models had proposed.[77,209] The herringbone model was originally invoked

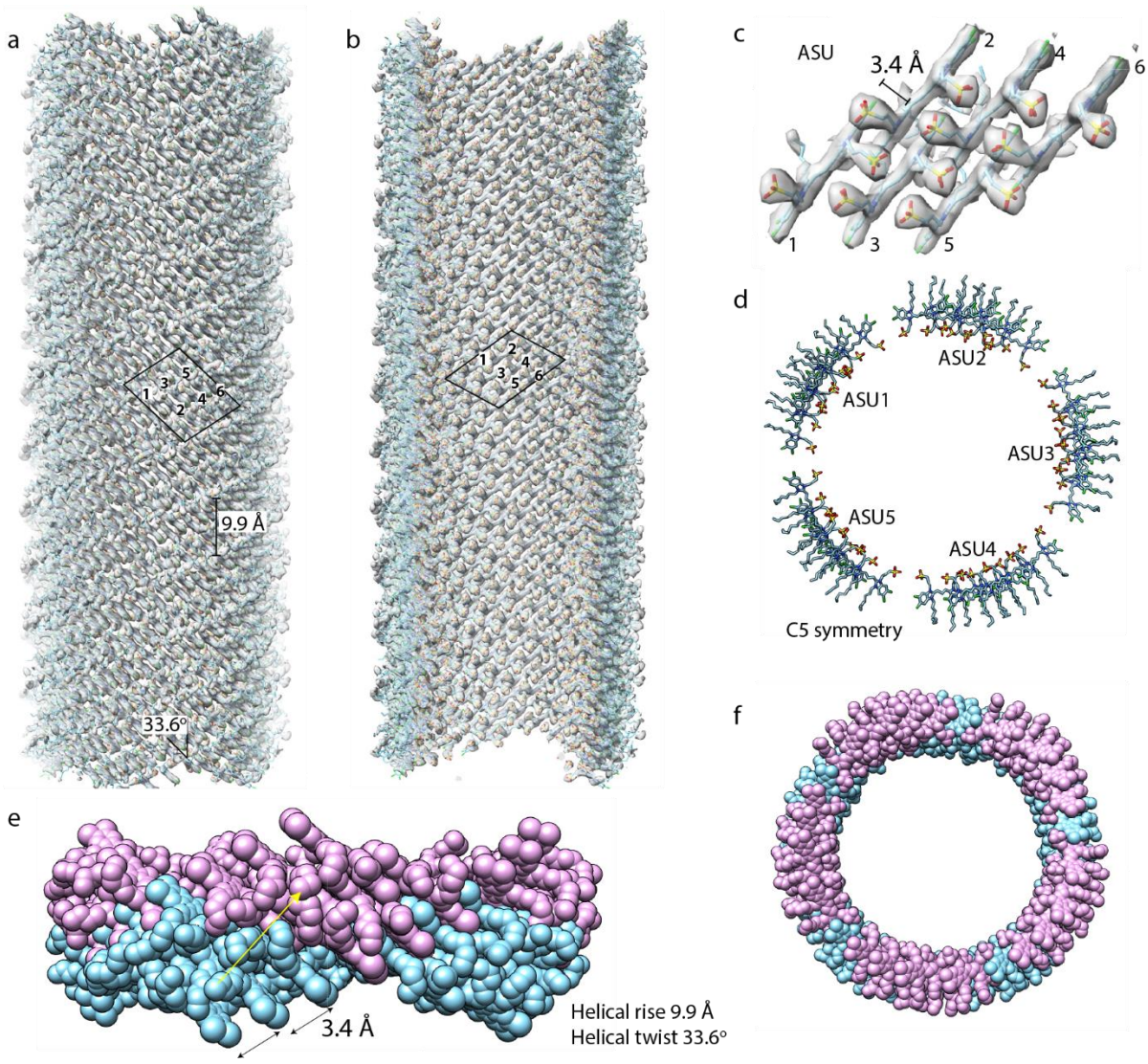

Figure 5.4. Molecular structure of inner wall obtained using IHRSR density maps.

a-b. Inner wall density overlaid with the structure showing excellent agreement with the reconstructed density, a. Side view, and b. Cut away view showing regularity of interlocked sulfonates, c. Structure of asymmetric unit (ASU) with 6 non-identical monomers, d. Top down view of the 5 repeats of the ASUs around the circumference, e. Side view and f. Top down view of two translated repeats of the ring in part d.

to explain the peak splitting in the inner wall spectra arising from symmetry breaking in the unit cell. While it was a reasonable motivation with the limited structural information available at the

time, our results clearly show that symmetry breaking arises not from the herringbone arrangement but from the 6 monomer ASU, wherein each monomer is non-identical. The π–π stacking distance between adjacent monomers is 3.4 Å and the slip between adjacent molecules is 12.7 Å or 5.3 Å. The two slip values arise from the fact that excitonic couplings between extended dipolar systems, with no boundary effects, are symmetric about half dipole length. Moreover, this slip value (~1/3 of molecular length) falls under the J-aggregation region with a band edge bright state. The excitonic band structure with a band edge bright state was indirectly verified in previous work using temperature dependent quantum yield and superradiance measurements.[79] The excitonic properties of these systems, often calculated using the Frenkel exciton model, are highly sensitive to such packing parameters.[25,124] Previously, estimates from gas phase calculations or MD simulations were used in the models.[25,211] This is the first direct experimental

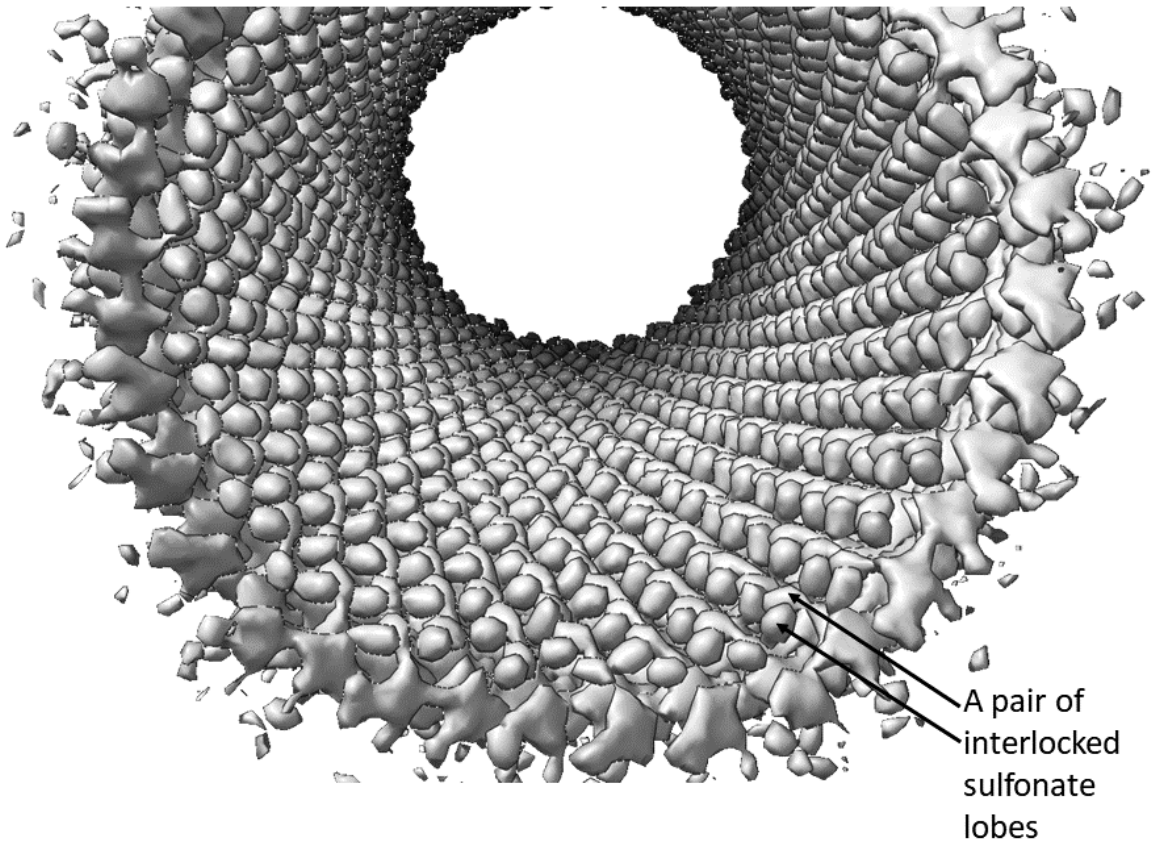

Figure 5.5 Top cut away inner wall density

A zoomed in inner wall density with cut away top down view from the perspective point inside the cylinder. The sulfonate lobes are show regular interlocked pattern on a single concentric ring.

observation of these molecular level geometric parameters in excitonic aggregates. The helical symmetry parameters obtained from this structure are 9.9 Å helical rise (Δz) and helical twist ($\Delta\phi$) of 33.6°.

Furthermore, we observe regular V-shaped interlocked patterns in the lumen of the inner wall (Figure 5.4b and 5.5). These interlocked lobes are assigned to the sulfonate groups from neighboring dye molecules that repel each other to form the highly regular interlocked pattern. We believe that the role of the sulfonate chains in the self-assembly is not just limited to the hydrophilicity of the dye but goes beyond in determining the slip-stacked arrangement enforced

by the interlocking sulfonate groups. Further, the 3 methylene spacers in the sulfonate chains may also be important for the interlocking. Too small methylene spacer between the dye backbone and sulfonates would have too much repulsion to allow for such interlocking, disrupting the entire self-assembly. On the other hand, larger methylene spacers might make the self-assembly too disordered or even enforce a completely different type of morphology. This could explain why Pawlik et al. observed an aggregate lineshape characteristic of sheet-like structures (similar to TDBC aggregate) for C8S4 aggregate (with 4 methylene spacer between the dye backbone and the sulfonates).[92,200] Due to higher degree of disorder in the outer wall, we were not able to reconstruct an outer was molecular model directly from the cryoEM density map.

5.6 Dimerized Frenkel exciton model based on inner wall structure

Using the structural parameters obtained from the above reconstruction, we construct a modified Frenkel exciton model where we use a brick layer arrangement dimer as a building block for the nanotube. Preliminary results from this model are shown in Figure 5.6. We use the redox chemistry approach to selectively photobleach the outer wall and isolate the inner wall spectra.[77] Using the dimerized Frenkel exciton Hamiltonian, we calculate absorption, LD and CD spectra for the inner wall that capture the complex excitonic features in the experimental spectra very well (Figure 5.6).

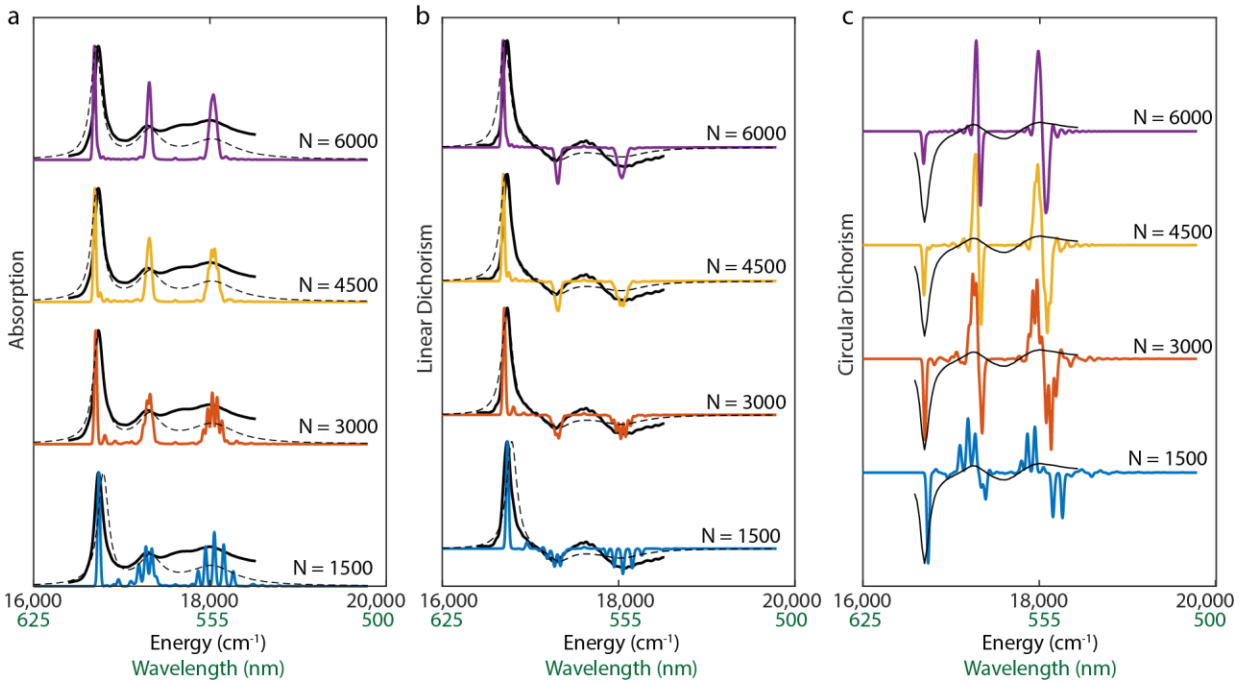

Figure 5.6. Modeling the optical spectra of isolated inner walls (IW) of LHNs using the cryoEM structure and dimerized Frenkel exciton model.

a. Absorption, b. linear dichroism, and c. circular dichroism spectra of isolated IW. Solid black lines: experimental spectra; colored lines: spectra calculated from the dimerized Frenkel exciton Hamiltonian corresponding to IW structures of varying sizes, blue: 1500, red: 3000, yellow: 4500, and purple: 6000 monomers; dashed black lines: calculated spectra assuming periodic boundary conditions with added Lorentzian broadenings (Lorentzian widths were obtained from experimental spectra). CD spectra with periodic boundary conditions and Lorentzian broadening could not be calculated in this case.

5.7 Significant differences between C8S3-Cl and C8S3-Br nanotubes

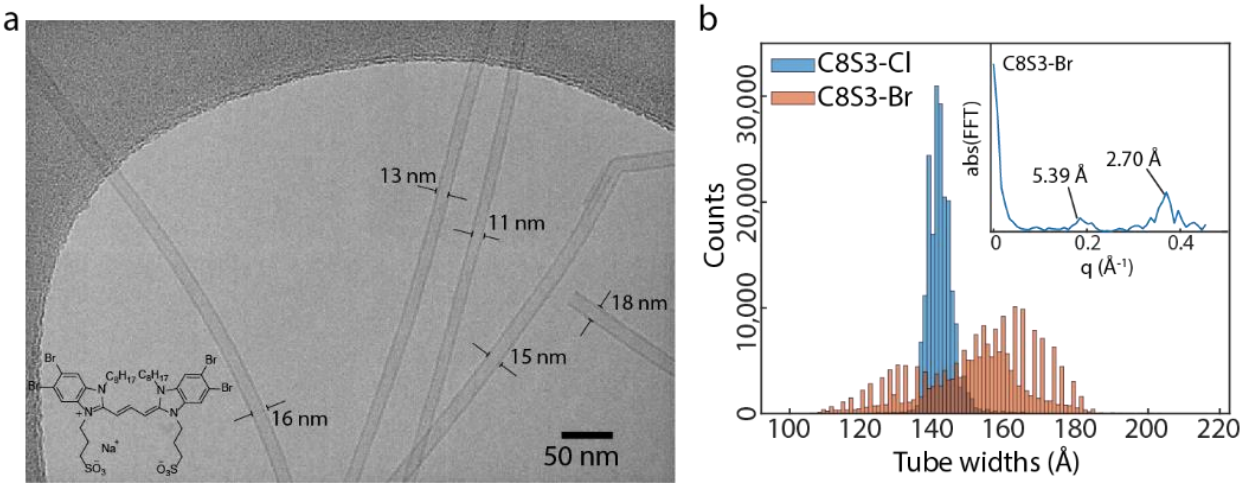

Figure 5.7 C8S3-Br double-walled nanotubes cryoEM and width comparison with C8S3-Cl a. CryoEM micrograph of C8S3-Br nanotubes showing variable tube diameters labelled on the image, inset. Structure of C8S3-Br, and b. Histograms of C8S3-Cl and C8S3-Br tube widths over ~104 segments, inset. Fourier spectrum of C8S3-Br histogram showing the step size of the discretized tube widths.

In order to understand the origin of the assembly better, we introduced a covalent modification on the 5, 5', 6 and 6' sites replacing Cl with slightly larger Br atoms (Figure 5.7a inset). We use the nomenclature C8S3-Cl for the prototypical LHNs and C8S3-Br for the modified ones. Nanotubular aggregates of C8S3-Br were previously reported to be wider than C8S3-Cl nanotubes as seen from the cryoEM micrograph of one double-walled nanotube.[210] In Figure 5.7, we show a representative cryoEM micrograph of an ensemble of C8S3-Br nanotubes. Unlike previously reported, both inner and outer wall diameters were variable with some narrower and some wider tubes than C8S3-Cl. Surprisingly, both inner and outer walls seem to increase or decrease in sync as the distance between the two walls appears to be the same. To address this discrepancy, we analyzed thousands of images of both C8S3-Cl and C8S3-Br nanotubes and histogram the outer wall widths of ~10^4 nanotubes in Figure 5.7b. While C8S3-Cl has a single narrow distribution

centered around ~ 140 Å, C8S3-Br shows a much wider bimodal distribution spreading from 110 Å – 180 Å. Because of the variable diameters, we could not apply the IHRSR algorithm on the C8S3-Br nanotubes to obtain reconstructed 3D map.

Another interesting observation is that the width distribution of C8S3-Br is not continuous like C8S3-Cl. Rather, C8S3-Br has discrete jumps in the distribution with certain bins having much higher probabilities than their neighboring ones. We Fourier transform the C8S3-Br histogram as shown in the inset of Figure 5.7b and observe two peaks at 2.70 Å and 5.39 Å, corresponding to the step size for the discretized widths.

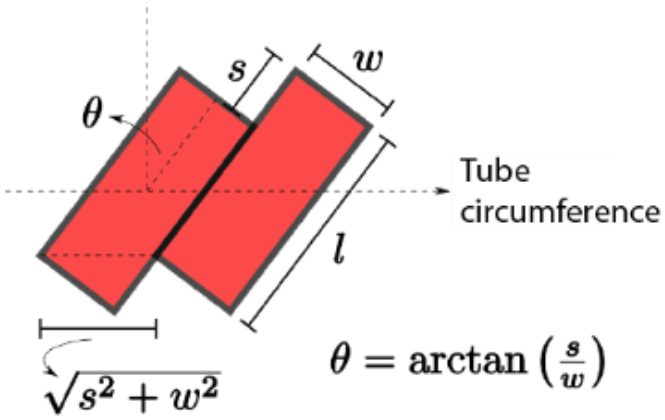

Figure 5.8 Geometric model based on slip stacked brick arrangement for C8S3-Br nanotubes Geometric relations for projection of a brick on the circumference were obtained using this model.

Starting from a simple brick layer arrangement model shown in Figure 5.8 we use the discrete width increments to calculate the chiral angle in the C8S3-Br tubes. From this model, the projection of a single monomer brick along the circumference of the tube is given by $\sqrt{s^2 + w^2}$, ignoring the curvature of the tubes. Here, s and w are the slip between adjacent molecules and the

perpendicular distance between the stacked faces. The slip and stacking distance are related by the chiral angles as $s = w \cdot \tan(\theta)$. Assuming smallest discrete jump is from a single monomer addition to the circumference as it the basic building block of the whole assembly, we can relate this to the circumference change from the discrete tube widths. Therefore,

$$\sqrt{s^2 + w^2} = \pi d'$$

where d' is the step size in the tube widths. Substituting for s from the above equation and solving for θ, we obtain

$$\theta = \cos^{-1}\left(\frac{w}{\pi d'}\right)$$

Extrapolating the stacking distance $w = 3.4$ Å from C8S3-Cl nanotubes and using the discrete step size obtained from the Fourier transform, we get the possible value of the chiral angle as $\theta = 66.4^{o}$. It is possible to experimentally measure this value from LD spectra where the peak splitting between the parallel and perpendicular peaks can be related to the chiral angles.

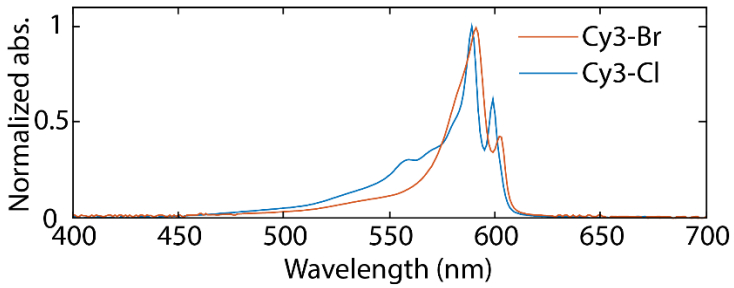

Figure 5.9 Comparison of absorption spectra of C8S3-Cl and C8S3-Br double-walled nanotubes

Normalized absorption spectrum of C8S3-Cl double-walled nanotubes or the prototypical LHNs (blue), overlaid with normalized absorption of C8S3-Br double-walled nanotubes with a wider width distribution.

Our results show that small chemical modifications may preserve the overall morphologies of the extended self-assemblies but the nanoscale structure with molecular details is highly sensitive to even small modifications. As the excitonic couplings are highly sensitive to the nanoscale structure, it is quite remarkable that the spectral features are quite conserved (Figure 5.9).

5.8 Conclusions

We present the first high-resolution structure of a supramolecular J-aggregate – light harvesting nanotubes (LHNs) of amphiphilic cyanine dye C8S3-Cl obtained from 3D reconstruction of cryoEM images using Iterative Helical Real Space Reconstruction (IHRSR) algorithm. Our structure provides key insights into self-assembly summarized as follows - (i) the aggregate has a brick layer arrangement of molecules with symmetry breaking arising from 6 monomer ASU in the inner and 8 monomer ASU in the outer wall; (ii) the outer wall has grooves that are absent in the inner wall; (iii) the sulfonate chains in both inner and outer walls show a highly conserved interlocked arrangement which may play a role in enforcing the slip-stacked arrangement that is responsible for the J-aggregate characteristics; (iv) small chemical modification from Cl to Br atoms lead to a highly distinct self-assembly with a much wider tube width distribution. Another peculiar observation is the discretized tube diameters which hints at the C8S3-Br tubes also have an underlying periodic structure such that only certain widths are allowed.

The helical nanotubular aggregates continue to be a rich model system for studying novel excitonic behaviors such as superradiance and artificial light harvesting. In future, this new information will enable the construction of more accurate models to describe the complex excitonic properties observed in such systems. The structural insights presented here will provide

guidelines for designing new supramolecular systems, wherein the rich excitonic properties can be directly engineered into the supramolecular structure. The interlocking of sulfonates can be further explored by chemically modifying the chain lengths and substitutions at the 3,3' positions.

5.9 Experimental section

Aggregate preparation

C8S3-Cl was obtained from FEW Chemicals GmbH and used without further purification. C8S3-Br was synthesized following a previously reported protocol.[210] C8S3-Cl aggregates (or LHNs) were prepared by injecting a methanol solution of C8S3 dye at 1.46 mM into Milli-Q water with the final conditions 0.48 mM dye and 30% MeOH (v/v) in glass vials pre-soaked in Milli-Q water for hydrophilization. The aggregate solutions were stored in parafilm sealed vials in dark at room temperature for 24 h before taking any measurements. C8S3-Br nanotubes were prepared similarly by injecting 10 mM methanol solution of dye monomer into milli-Q water giving 2mM dye, 20% MeOH as the final conditions. C8S3-Br was stored for longer time (1-2 weeks) to allow for growth of long tubes. Shorter equilibration times gave bundled aggregates for C8S3-Br.

Inner wall isolation

For isolation of inner wall spectra on C8S3-Cl LHNs, a modified form of previously reported procedure was used.[77] C8S3 LHNs were prepared by dissolving C8S3 monomer (2.58 mg, 2.86 μmol) into 2.4 mL spectroscopic grade methanol (Fisher). This solution was sonicated for 30 seconds to ensure complete dissolution before adding 4.76 mL Milli-Q H_2O. The solution was parafilmed and stored in the dark for 24 h before measuring the absorbance to confirm doubled-walled LHN formation. For outer wall bleaching, 0.6 mL of 0.011 M aqueous $AgNO_3$ solution in Milli-Q H_2O was added to the LHNs in a scintillation vial. The vial was briefly shaken to ensure

mixing, then illuminated with a flashlight until the outer wall peak was completely bleached (~ 10 min) and kept in dark subsequently. Further spectroscopic measurements were done immediately.

Spectroscopic measurements

UV-Vis and LD spectra were taken on Agilent Cary-60 spectrometer in 0.2 mm or 0.01 mm path length quartz cuvettes obtained from Starna Cells. For LD spectra, a linear polarizer (Thorlabs LPVIS050, mounted on a rotational stage) was inserted into the spectrophotometer between the sample and lamp source. To achieve parallel or perpendicular polarizations, the polarizer was set to 0° or 90°, respectively. The instrument was blanked using the appropriate solvent for each polarizer orientation. The sample was flown at a rate of 4 mL/min through a 0.2 mm path length flow cell (Starna Cells) using a syringe pump (AL-1000, Thermo Fisher) in order to align the nanotubes to the direction of the flow. CD spectra were taken on ChiraScan V100 in 0.2 mm path length cuvettes while purging the chamber with N_2 gas.

CryoEM data collection and processing

2 μl of C8S3-Cl or C8S3-Br double-walled nanotubes sample were applied to plasma-cleaned lacey carbon grids, followed by plunge-freezing in liquid ethane using a Leica EM GP. Data collection was carried out at liquid nitrogen temperature on a Titan Krios microscope (ThermoFisher Scientific) operated at an accelerating voltage of 300 kV. 40 movie frames were collected with defocus values range between -1 to -2.5 μm on a K3 camera (Gatan), with a total dose of ~55 electrons per $Å^2$. For C8S3-Cl double-walled nanotube, a total of 193,693 384px-long segments were manually boxed in EMAN2 from 2000 image, followed by testing the helical symmetry possibilities in SPIDER. The C5 rotational symmetry yield the most reasonable map which was used as an initial map to further processing in RELION 3.0.[220] Three rounds of

Refine3D, PostProcessing, contrast transfer function (CTF) refinement and Bayesian polishing were done until the map improved with recognizable small molecule features at the resolution of 3.3 Å. The helical parameters converged to a rotation of 33.6° and an axial rise of 9.9 Å per subunit. The resolution of the final reconstruction was determined by the Fourier shell correlation (FSC) between two independent half maps, which was 3.3 Å at FSC = 0.143.

Model building and refinement

We use the C8S3-Cl PDB model as an initial template to dock into the cryoEM map by rigid body fitting in UCSF Chimera,[221] and then manually edited the model in Coot.[218] The refined monomeric model of C8S3 was then re-built in Chimera with helical symmetry and rotational symmetry, followed by real-space refinement with Phenix.[219] The coordinates of LHNs will be deposited to the Protein Data Bank, and the corresponding cryoEM map will be deposited in the EMDB.

Chapter 6

Challenges and Opportunities

We discussed how aggregation can be used as a platform to tune photophysical properties of chromophores and to avail unconventional photophysical behaviors. In the previous chapters, we showed ways for overall chemical control over aggregate self-assembly and the excitonic properties. We also discussed high resolution cryoEM structure for a tubular J-aggregate that will allow better understanding of the origin of the excitonic properties. Several questions still remain open challenges for facilitating practical applications and improving our fundamental understanding of excitons in molecular systems. This chapter summarizes some of these challenges, their significance to the overall field, and plans to address them.

6.1 Enthalpic and entropic contributions to the self-assembly

In Chapter 3, we focused on thermodynamic control of aggregation. However, many of these systems, especially the tubular aggregates have slow growth components. Because of the slow nature of the growth, it was possible to treat each state being in quasi-equilibrium in Chapter 3. In some cases, we have now observed that both tubular and 2D morphologies are possible, and their slow interconversion can be really cumbersome for further studies. Understanding the driving forces for such interconversions will enable a more precise control over aggregation. Temperature dependent melting studies as well as time dependent aggregation studies can be performed with a real time spectral collection setup.

Plan: Figure 6.1 shows preliminary data from temperature dependent aggregate melting studies (not to be confused with the cryogenic temperature dependence in Chapters 2 and 4 with

sugar matrix stabilized aggregates). We prepare the aggregates by injecting a methanol solution of the dye into water or aqueous NaCl (specific conditions were the same as Chapter 3) and allowed to equilibrate in dark at room temperature. This can be kept inside a Peltier temperature control setup connected to a UV-Vis spectrometer. Freezing and boiling points of solvent mixtures are measured previously. Copper tape is used for good thermal contact. Absorption spectra collected after heating to different temperatures show a 'melting' of 2D J-aggregates into H-aggregates and monomers (Figure 6.1). We use a modified version of the model in Chapter 3 to separate enthalpic and entropic contributions to the self-assembly for a dimer system.

$$2M \rightleftharpoons H \tag{6.1}$$

$$C_{total} = C_M + 2C_H \tag{6.2}$$

$$2e^{-\Delta H^o/RT} e^{\Delta S^o/R} C_M^2 - C_M - C_{Tot} = 0 \tag{6.3}$$

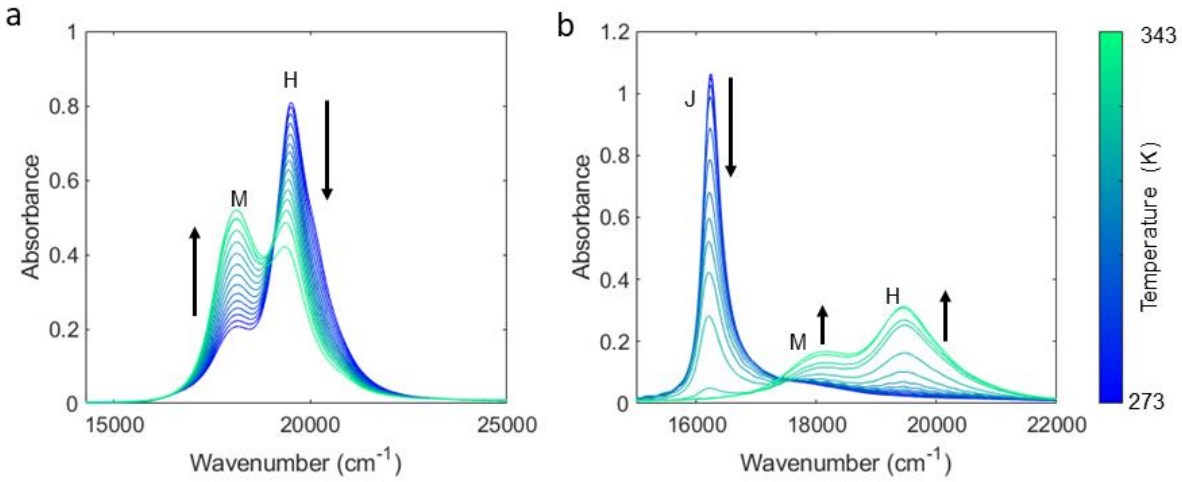

Figure 6.1. Aggregate melting studies with Cy3-Et dimer and 2D aggregate.
Absorption spectra of Cy3-Et a. H-aggregate (dimer) solution and b. 2D sheet-like J-aggregate solution with temperature. Arrows indicate changes with increasing temperature.

Keeping $\Delta H°$ and $\Delta S°$ as open parameters, the quadratic polynomial can be solved for a given temperature to obtain the mole fractions of monomer and H-aggregate. We were able to fit the

model to the experimental data for Cy3-Et dimer melting studies (Figure 6.2). We obtain $\Delta H° = -26$ kJ/mol and $\Delta S° = -6$ J/K.mol, suggesting that the dimerization of Cy3-Et is primarily enthalpically driven. Once we extend this to larger J-aggregates, we may expect a shift in this behavior. The hydrophobic effect may play a role for the extended systems where the entropy increase is driven by a large number of solvent molecules expelled from the solvation shells of individual monomers.

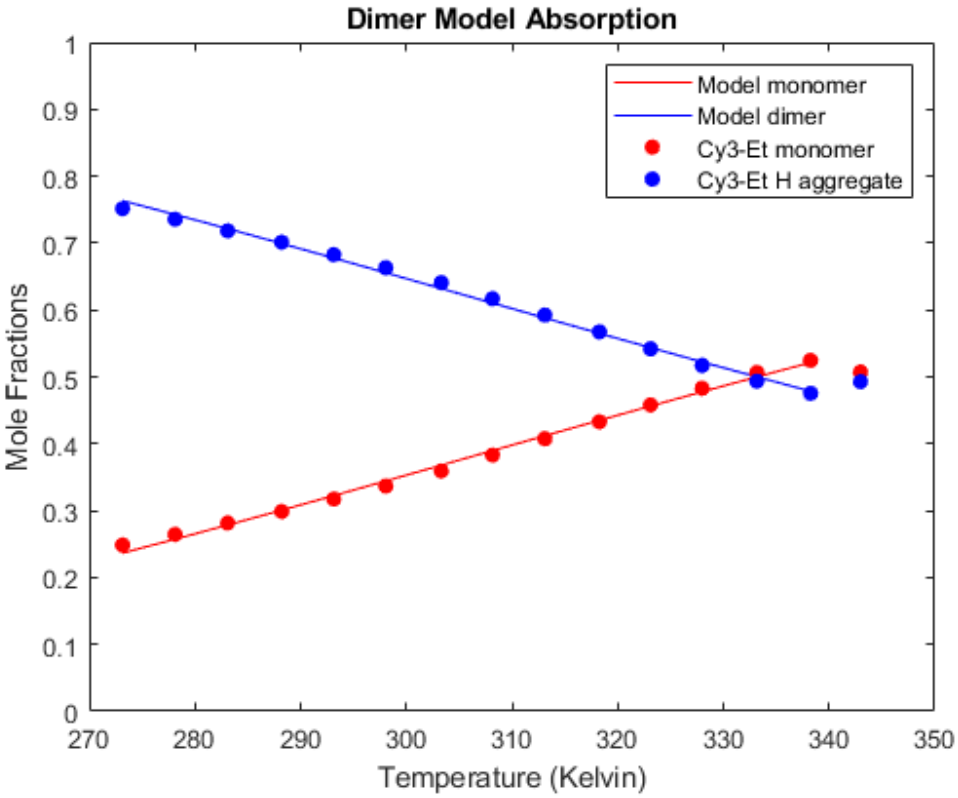

Figure 6.2. Preliminary results from melting studies of Cy3-Et H-aggregate fitted to a monomer-dimer conversion model

Mole fractions of Cy3-Et monomer (red circles) and H-aggregate (blue circles) obtained from temperature dependent melting studies. Lines are concurrent fits for both components obtained from the a thermodynamic model for $\Delta H° = -26$ kJ/mol and $\Delta S° = -6$ J/mol.K. A solution of H-aggregate at equilibrium was heated using a Peltier setup with added copper tapes and spectra

were taken after temperature equilibration. Last temperature point was excluded as the solution had started bubbling.

6.2 Kinetics of aggregation

Real time observation of the aggregate self-assembly will provide a lot of insights relevant for modulating exciton transport in the aggregates. C8S3 LHNs, whose structure was discussed in Chapter 5, show complicated optical features in absorption and circular dichroism (CD) spectra such as strong excitonic superradiance and amplified CD signals. Observing the origin

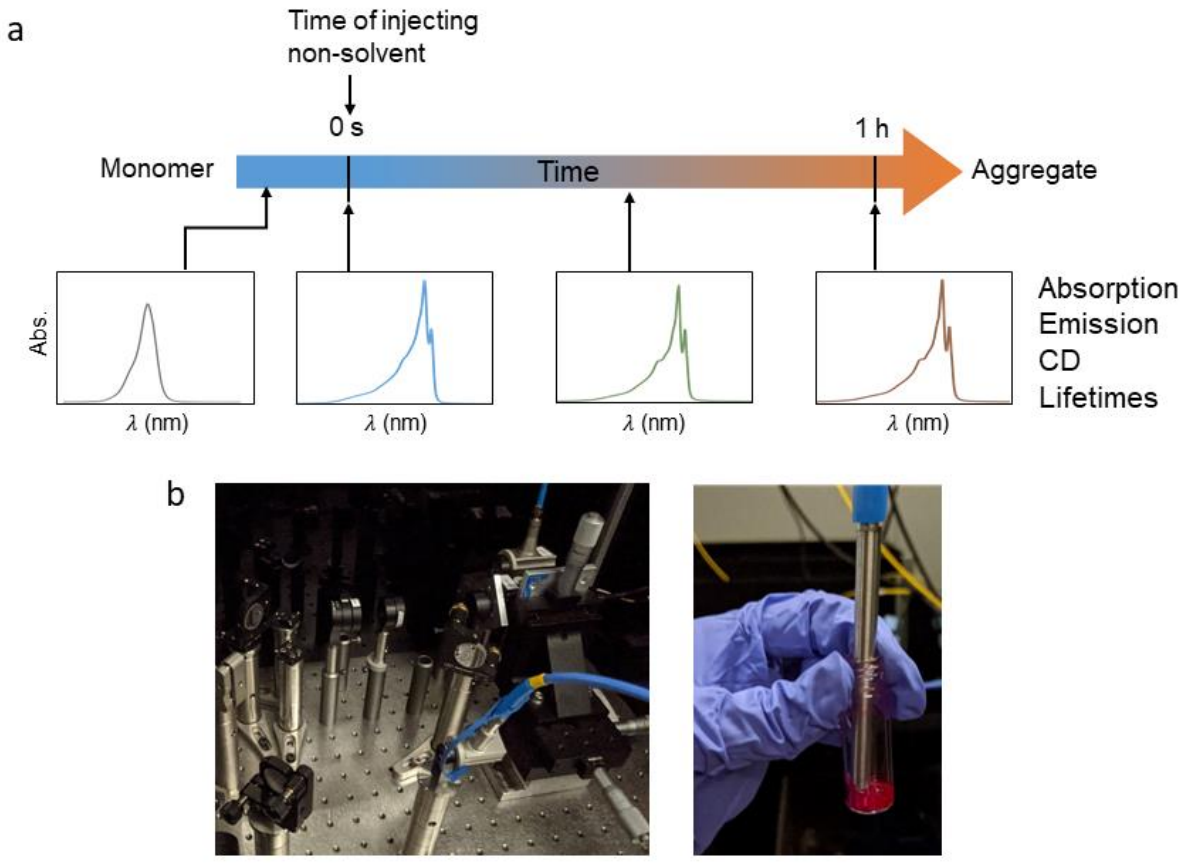

Figure 6.3 Schematic representation of real-time spectroscopies for aggregate formation, experimental setup for in-situ time-resolved photoluminescence measurement

a. Schematic showing collection of spectroscopic measurements before, during and after adding the non-solvent to the dye monomers allowing for real-time spectroscopies to study aggregate

formation, b. Photographs of in-situ time-resolved photoluminescence experiment – (left) detection setup, and (right) collection setup with a dip-probe allowing for real-time photon collection during aggregate formation.

structural features that lead to the unusual spectral signatures will help answer several questions: (i) Why do planar achiral molecules assemble into chiral structures with a preferred handedness? (ii) What is the extent of structural disorder initially vs a long time after mixing? Real time spectroscopic studies can help answer such questions. One can collect absorption, emission, lifetimes and CD spectra before, during and after mixing the non-solvent with the monomer (Figure 6.3a). Correlating the real-time information from all spectroscopies will provide a complete picture of the aggregation process.

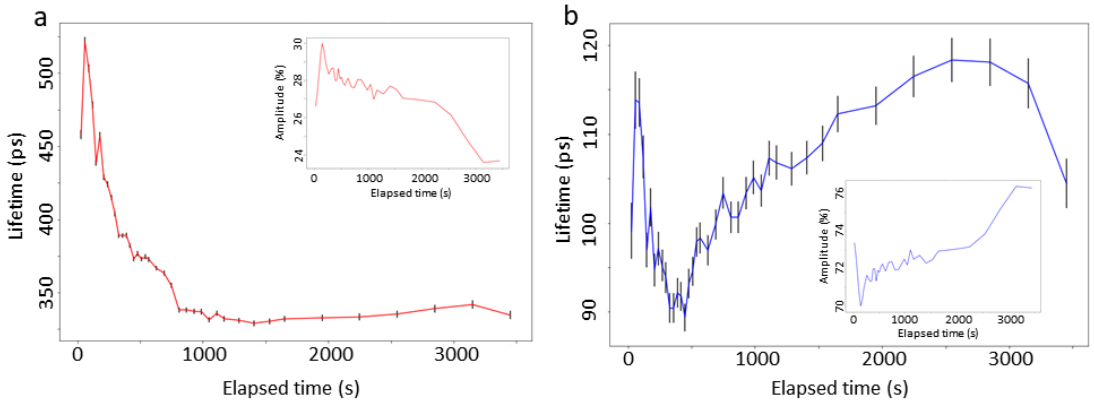

Figure 6.4. Preliminary results from in-situ time-resolved photoluminescence of C8S3 LHNs a-b. Each lifetime component (red and blue) with the amplitudes corresponding to each lifetime component (insets) as a function of time elapsed from the addition of non-solvent. Parameters were extracted from biexponential fits of in-situ time-resolved photoluminescence data, t = 0 s corresponds to the time of injection of water into a monomer solution. Error bars are from confidence intervals of the fits.

Plan: Real-time steady-state spectra can be collected on a commercial spectrometer with a kinetic set up where spectra can be automatically taken at a given time interval. For lifetimes, we

use a home built in-situ time resolved photoluminescence setup shown in Figure 6.3b. We excite and collect using a single fiber which is then branched off and the emitted photons are collected using a time-correlated single photon counting (TCSPC) set up. Figure 6.4 shows the preliminary data from this experiment where the C8S3 monomer was taken in a vial and photons were continuously collected as the water was added to it. $t = 0\ s$ corresponds to the time of water addition. The photons are then post processed to obtain TCSPC histograms as the aggregation progressed in real time. The histograms were fit to bi-exponentials. The progress of each lifetime component over the course of real time is shown in Figure 6.4. We observe that there is a longer component that decreases initially and then eventually settles to a values of ~325 ps. We hypothesize that this is relaxation to the band-edge component that remains constant once the structure is formed. The other shorter component shows sharp decrease in the lifetime for the first 500 s, followed by a slow increase. Further real time spectroscopies will help assign these lifetimes to the underlying excitonic processes.

Such spectroscopic studies can also be corroborated with time-dependent cryoEM studies by freezing the samples at different times after mixing the monomer solutions and non-solvents. Though, due to the low throughput of plunge-freezing method, this will not provide the same temporal resolution as other spectroscopic studies. Nevertheless, samples can be frozen few seconds after mixing and ~ 1 h hour after mixing. Such studies will allow observation of the morphological changes that correspond to the real-time spectroscopic measurements. One crucial assumption is that there are no further rearrangements once the samples are frozen in liquid ethane.

6.3 Separating inter- and intra-aggregate disorder

The origin of characteristic spectral lineshapes of extended I- or J-aggregates has been a long standing puzzle.[32,35] One way to get additional information about this is by separating ensemble broadening effects from single aggregate disorder. Specifically, molecules within an aggregates can have an inhomogeneous distribution of energies, deviations from random fluctuations may occur in presence of structural defects such as bends or folds in the sheets, or individual site deletions due to photobleaching or chemical reactivity.[79] Understanding the effects of various types of disorder will be a starting point in modulating exciton transport.

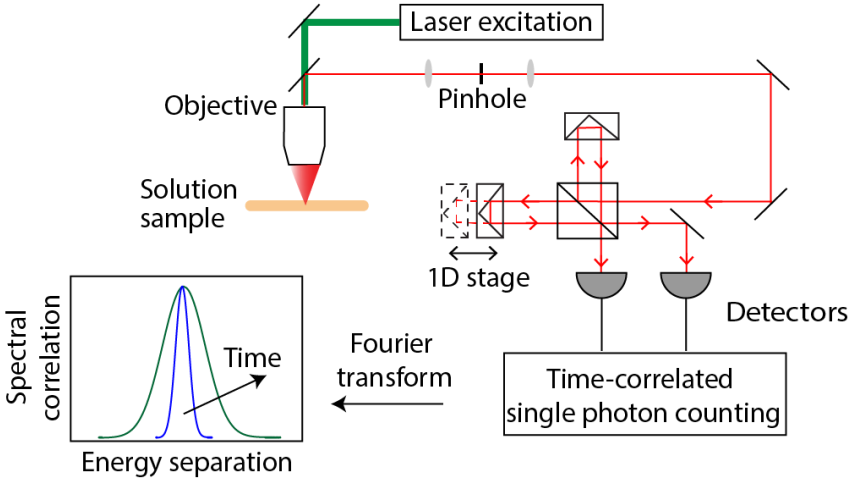

Figure 6.5. Schematic for solution-photon correlation Fourier spectroscopy (s-PCFS) set-up. Epifluorescence excitation with an objective and pinhole for collection of photons from the confocal region within a solution sample inside a thin capillary tube. The collected photons are sent through an interferometry set-up equipped with time-correlated single photon counting modules. This allows for spectral correlations of the collected photons providing estimates of energetic disorders within the aggregates.

Plan: Solution photon-correlated Fourier spectroscopy (s-PCFS) is a technique that combines confocal microscopy with Fourier spectroscopy wherein photons coming from the confocal volume of a microscope objective are collected and sent either through a 50:50 beam splitter or a

Mark-Zehnder interferometer set-up (same as the interferometer used in decay-associated Fourier spectroscopy).[197,222,223] The former allows for g_2 measurements while the latter, provides g_2 along with spectral correlations. By taking the photons collected at very short time intervals (less than the diffusion time of an aggregate), we can effectively look at single aggregate spectral correlations as well as ensemble spectral correlations within the same setup. Further, taking similar data on 2D as well as tubular aggregates will be useful in delineating the role of morphology in exciton transport.

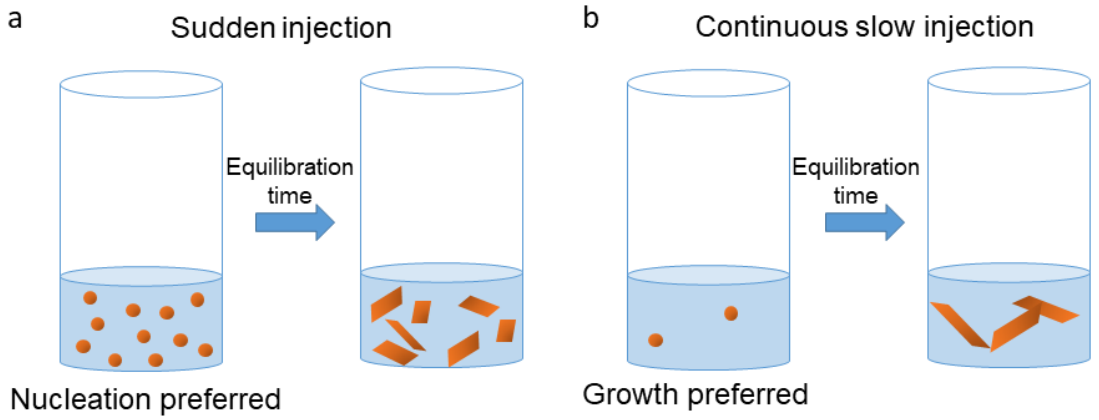

Figure 6.6. Schematic of kinetic control of aggregation with different rates of addition of monomer.

a. Current method: sudden injection of a concentrated monomer into a non-solvent leading to immediate nucleation, b. slow addition of the monomer over a continuous time period allows for growth, enabling longer aggregates.

6.4 Size and shape control

In Chapter 4, we modulated the nanoscale packing geometries such as slips and brick lengths in 2D aggregates. Currently, we have no control on the overall sizes and aspect ratios of the aggregates that are formed through solution self-assembly. Previous theoretical studies with crystalline aggregates have shown that aspect ratios may play a role in the asymmetric lineshapes

that were also observed in Chapter 4.[35,36] Exciton transport can also be affected by these parameters through a disorder dependence.

Plan: To delineate such effects, making size and shape controlled aggregates can be an avenue to pursue in the future. The best way to do this would be through kinetic control of nucleation and growth. Kinetic control can be achieved via several means such as concentration and temperature. A slow addition approach can be used to avoid excessive nucleation and promote growth, enabling larger sized aggregates (Figure 6.6). H-bonding groups (carboxylates, amines) or other directional groups can be strategically placed on the core cyanine dye structure to promote growth in a specific direction.[106,224]

6.5 High-resolution cryoEM of 2D aggregates

In Chapter 5, we discussed the nanoscale structure of tubular aggregates and its importance for modeling excitonic properties accurately. A similar high-resolution structure of 2D aggregates in the native solution state has never been experimentally confirmed. Specifically, brick dimensions and the number of monomers in the effective 'unit cell' have not been directly observed. This information can be obtained using cryoEM electron diffraction and single particle analysis based approach. Normally, diffraction patterns from microcrystals can be directly obtained using selected-area electron diffraction (SAED). However, due to extremely low contrast in these single layer sheets, SAED patterns become hard to analyze.

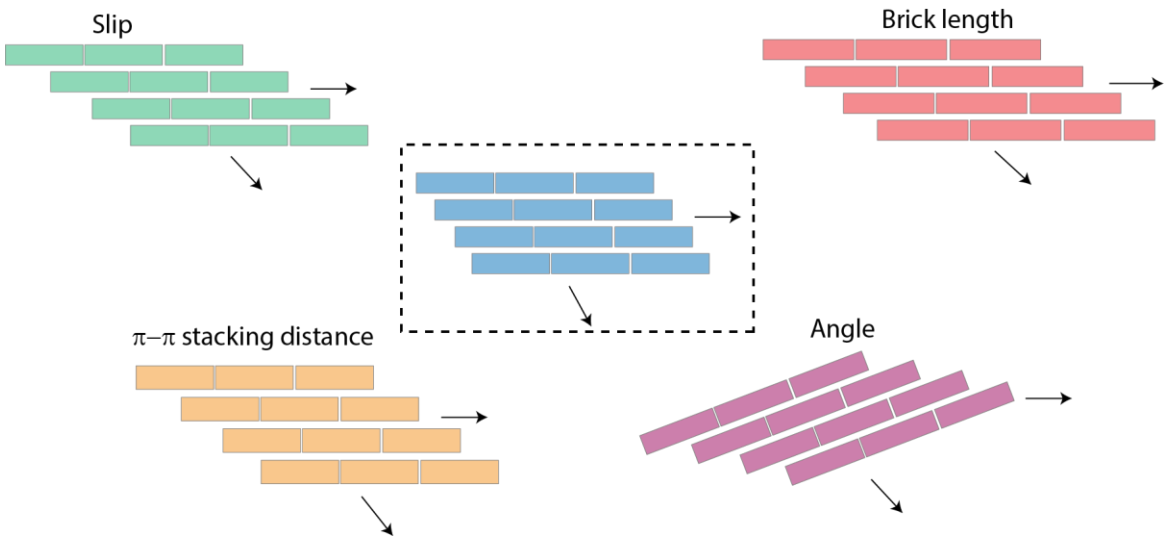

Figure 6.7. Possibilities of molecular packing geometries in 2D aggregates that can be observed in high resolution cryoEM structure.

Expected geometric differences in 2D aggregates with respect to the central structure (blue) that can be directly observed with single particle analysis based cryoEM structure determination method. Black arrows indicate the directions of sheet growth.

Plan: Using thinner grids such as single layer graphene or ultrathin carbon, 100s and 1000s of images can be automatically collected images, followed by alignment steps. Superimposing a large number of Fourier transforms will improve the signal-to-noise ratio. Analyzing these diffractions should be straightforward in a standard XRD software. In either case, practical considerations for electron dosage need to be kept in mind so as to not alter the native atomic arrangement and blur the data. Further, comparative datasets with different molecular packings can be used to directly confirm the effects of specific substituents on nanoscale packing parameters. For example: as shown in Chapters 2 and 4, Cy7-DPA should have a higher slip than Cy7-Ph, both of which should have a higher brick length than Cy5-Ph (Figure 6.7). Further, the direction of the molecular bricks within the sheets as well as differences in the brick widths or cofacial stacking distances between molecules are all unknown parameters that can be uncovered with direct observation of nanoscale

structures (Figure 6.7). SPA approach does not provide information about structural disorder, as it will be averaged out in the superimposition. But especially in disordered systems such as the aggregates, averaging out of the 'noise' can be really useful in backing out the molecular scale parameters (such as slip), even if it's not near-atomic resolution.

6.6 Conclusions

The directions outlined above present the next steps to findings from this dissertation. Understanding the enthalpic and entropic contributions to self-assembly will enable better design and control of aggregation. If the formation of extended aggregates is found to be enthalpically driven, additional intermolecular interactions can be built into the chromophore structures such as donor-acceptor interactions or more delocalizable π-clouds. In entropically driven self-assemblies, one can fine tune chromophore-solvent interactions and sizes of the aggregates. Real-time observation of how the aggregates are formed will explain the origins of the complicated structural and excitonic features and provide pathways for fine tuning of structural disorder within the aggregates. Exploring the origin of the unusual asymmetric lineshapes of the aggregates is useful for several optoelectronic as well as bioimaging applications. Size and shape control of the aggregates as well as s-PCFS studies discussed above will provide insights into this question. On the structural side, high-resolution cryoEM studies will allow for direct confirmation of the nanoscale structure. This will enable precise structural modifications to the cyanine dye structure for desired excitonic properties.

6.7 Overall remarks

Ever since the first observation of J-aggregation in the 1930s and early descriptions of molecular excitons, such chromophore assemblies have attracted researchers from diverse areas. The aspect that stands out to me the most about this work is the confluence of concepts from supramolecular chemistry, photochemistry and quantum chemistry.

Building on such concepts, we provide pathways for chemically controlling the self-assembly and excitonic properties of higher dimensional aggregates. We show that molecular aggregation, can be used as a platform for tuning photophysical properties in addition to existing approaches such as covalent modification and confinement. Further, aggregation allows for novel photophysical behaviors that are not conventionally accessible. A particular long-standing goal is using J-aggregation to redshift absorption and emission all the way into SWIR while maintaining high quantum yields and molar absorptivities. Using the insights and tools provided here, this goal can now be realized by making a higher slip aggregate in SWIR that will have a band-edge bright state. This dissertation also provides guidelines for designing new aggregates, followed by a general workflow for thorough characterizations of their morphologies, supramolecular structures, and excitonic band structures.

Broad future directions in the field should address the challenges with practical applicability and explore novel excitonic behaviors. For example, investigations of triplet excitonic states in molecular aggregates can provide means for development of efficient triplet sensitizers. For practical applicability, making the aggregates processable for patternable devices as well as protection of the nanoscale structure for preserving excitonic properties in different environments will be major challenges to be addressed.

References

(1) Brixner, T.; Hildner, R.; Köhler, J.; Lambert, C.; Würthner, F. Exciton Transport in Molecular Aggregates - From Natural Antennas to Synthetic Chromophore Systems. *Adv. Energy Mater.* **2017**, *7* (16), 1700236.

(2) Maiuri, M.; Ostroumov, E. E.; Saer, R. G.; Blankenship, R. E.; Scholes, G. D. Coherent Wavepackets in the Fenna-Matthews-Olson Complex Are Robust to Excitonic-Structure Perturbations Caused by Mutagenesis. *Nat. Chem.* **2018**, *10* (2), 177–183.

(3) Tretiak*, S.; Chris Middleton; Vladimir Chernyak, and; Mukamel*, S. Exciton Hamiltonian for the Bacteriochlorophyll System in the LH2 Antenna Complex of Purple Bacteria. *J. Phys. Chem. B* **2000**, *104* (18), 4519–4528.

(4) Parkash, J.; Robblee, J. H.; Agnew, J.; Gibbs, E.; Collings, P.; Pasternack, R. F.; De Paula, J. C. Depolarized Resonance Light Scattering by Porphyrin and Chlorophyll a Aggregates. *Biophys. J.* **1998**, *74* (4), 2089–2099.

(5) Gülen, D. Significance of the Excitonic Intensity Borrowing in the J-/H-Aggregates of Bacteriochlorophylls/Chlorophylls. *Photosynth. Res.* **2006**, *87* (2), 205–214.

(6) Grieco, C.; Kohl, F. R.; Hanes, A. T.; Kohler, B. Probing the Heterogeneous Structure of Eumelanin Using Ultrafast Vibrational Fingerprinting. *Nat. Commun. 2020 111* **2020**, *11* (1), 1–9.

(7) Yamagata, H.; Spano, F. C. Interplay between Intrachain and Interchain Interactions in Semiconducting Polymer Assemblies: The HJ-Aggregate Model. *J. Chem. Phys.* **2012**, *136* (18), 184901.

(8) Yamagata, H.; Spano, F. C. Strong Photophysical Similarities between Conjugated Polymers and J-Aggregates. *J. Phys. Chem. Lett.* **2014**, *5* (3), 622–632.

(9) Spano, F. C. The Spectral Signatures of Frenkel Polarons in H- and J-Aggregates. *Acc. Chem. Res.* **2009**, *43* (3), 429–439.

(10) Elisa Palacios-Lidón; Emin Istif; M. Benito, A.; K. Maser, W.; Jaime Colchero. Nanoscale J-Aggregates of Poly(3-Hexylthiophene): Key to Electronic Interface Interactions with Graphene Oxide as Revealed by KPFM. *Nanoscale* **2019**, *11* (23), 11202–11208.

(11) Würthner, F.; Kaiser, T. E.; Saha-Möller, C. R. J-Aggregates: From Serendipitous Discovery to Supramolecular Engineering of Functional Dye Materials. *Angewandte Chemie - International Edition*. April 4, 2011, pp 3376–3410.

(12) Bricks, J. L.; Slominskii, Y. L.; Panas, I. D.; Demchenko, A. P. Fluorescent J-Aggregates of Cyanine Dyes: Basic Research and Applications Review. *Methods Appl. Fluoresc.* **2017**, *6* (1), 012001.

(13) Li, K.; Duan, X.; Jiang, Z.; Ding, D.; Chen, Y.; Zhang, G.-Q.; Liu, Z. J-Aggregates of Meso-[2.2]Paracyclophanyl-BODIPY Dye for NIR-II Imaging. *Nat. Commun. 2021 121* **2021**, *12* (1), 1–9.

(14) Wan, Y.; Stradomska, A.; Knoester, J.; Huang, L. Direct Imaging of Exciton Transport in Tubular Porphyrin Aggregates by Ultrafast Microscopy. *J. Am. Chem. Soc.* **2017**, *139* (21), 7287–7293.

(15) Lin, H.; Camacho, R.; Tian, Y.; Kaiser, T. E.; Würthner, F.; Scheblykin, I. G. Collective Fluorescence Blinking in Linear J-Aggregates Assisted by Long-Distance Exciton

Migration. *Nano Lett.* **2010**, *10* (2), 620–626.

(16) Fidder, H.; Terpstra, J.; Wiersma, D. A. Optical Dynamics of Excitons in Aggregates of a Carbocyanine Dye. *Phosphorescence Abil. upon Aggreg. Dye Mol. J. Chem. Phys.* **1991**, *94*, 721.

(17) Von Berlepsch, H.; Böttcher, C. Network Superstructure of Pseudoisocyanine J-Aggregates in Aqueous Sodium-Chloride Solution Revealed by Cryo-Transmission Electron Microscopy. *J. Phys. Chem. B* **2002**, *106* (12), 3146–3150.

(18) Baraclough, M.; Seetharaman, S. S.; Hooper, I. R.; Barnes, W. L. Metamaterial Analogues of Molecular Aggregates. *ACS Photonics* **2019**, *6* (11), 3003–3009.

(19) Kasha, M. Energy Transfer Mechanisms and the Molecular Exciton Model for Molecular Aggregates. *Radiat. Res.* **1963**, *20* (1), 55–71.

(20) Kasha, M.; Rawls, H. R.; El-Bayoumi, M. A. The Exciton Model In Molecular Spectroscopy. *Pure Appl. Chem.* **1965**, *11* (3–4), 371–392.

(21) Jelley, E. E. Spectral Absorption and Fluorescence of Dyes in the Molecular State. *Nature* **1936**, *138* (3502), 1009–1010.

(22) Scheibe, G. Über Die Veränderlichkeit Der Absorptionsspektren in Lösungen Und Die Nebenvalenzen Als Ihre Ursache. *Angew. Chemie* **1937**, *50* (11), 212–219.

(23) Bücher, H.; Kuhn, H. Scheibe Aggregate Formation of Cyanine Dyes in Monolayers. *Chem. Phys. Lett.* **1970**, *6* (3), 183–185.

(24) Yamagata, H.; Spano, F. C. Vibronic Coupling in Quantum Wires: Applications to Polydiacetylene. *J. Chem. Phys.* **2011**, *135* (5).

(25) Didraga, C.; Pugžlys, A.; Hania, P. R.; von Berlepsch, H.; Duppen, K.; Knoester, J. Structure, Spectroscopy, and Microscopic Model of Tubular Carbocyanine Dye Aggregates. *J. Phys. Chem. B* **2004**, *108* (39), 14976–14985.

(26) Hestand, N. J.; Spano, F. C. Molecular Aggregate Photophysics beyond the Kasha Model: Novel Design Principles for Organic Materials. *Acc. Chem. Res.* **2017**, *50* (2), 341–350.

(27) Bialas, D.; Zhong, C.; Würthner, F.; Spano, F. C. Essential States Model for Merocyanine Dye Stacks: Bridging Electronic and Optical Absorption Properties. *J. Phys. Chem. C* **2019**, *123* (30), 18654–18664.

(28) Grisanti, L.; D'Avino, G.; Painelli, A.; Guasch, J.; Ratera, I.; Veciana, J. Essential State Models for Solvatochromism in Donor−Acceptor Molecules: The Role of the Bridge. *J. Phys. Chem. B* **2009**, *113* (14), 4718–4725.

(29) Czikklely, V.; Forsterling, H. D.; Kuhn, H. Extended Dipole Model for Aggregates of Dye Molecules. *Chem. Phys. Lett.* **1970**, *6* (3), 207–210.

(30) Möbius, D.; Kuhn, H. Energy Transfer in Monolayers with Cyanine Dye Sheibe Aggregates. *J. Appl. Phys.* **1988**, *64* (10), 5138–5141.

(31) Duschl, C.; Frey, W.; Knoll, W. The Crystalline Structure of Two-Dimensional Cyanine Dye Single Crystals as Revealed by Electron Diffraction. *Thin Solid Films* **1988**, *160* (1–2), 251–255.

(32) Knapp, E. W. Lineshapes of Molecular Aggregates, Exchange Narrowing and Intersite Correlation. *Chem. Phys.* **1984**, *85* (1), 73–82.

(33) Liess, A.; Arjona-Esteban, A.; Kudzus, A.; Albert, J.; Krause, A.; Lv, A.; Stolte, M.;

Meerholz, K.; Würthner, F. Ultranarrow Bandwidth Organic Photodiodes by Exchange Narrowing in Merocyanine H- and J-Aggregate Excitonic Systems. *Adv. Funct. Mater.* **2019**, *29* (21), 1805058.

(34) Turkin, A.; Malý, P.; Lambert, C. Fluorescence Band Exchange Narrowing in a Series of Squaraine Oligomers: Energetic vs. Structural Disorder. *Phys. Chem. Chem. Phys.* **2021**, *23* (34), 18393–18403.

(35) Müller, M.; Paulheim, A.; Eisfeld, A.; Sokolowski, M. Finite Size Line Broadening and Superradiance of Optical Transitions in Two Dimensional Long-Range Ordered Molecular Aggregates. *J. Chem. Phys.* **2013**, *139* (4), 044302.

(36) Bondarenko, A. S.; Jansen, T. L. C.; Knoester, J. Exciton Localization in Tubular Molecular Aggregates: Size Effects and Optical Response. *J. Chem. Phys.* **2020**, *152* (19), 194302.

(37) Marciniak, H.; Auerhammer, N.; Ricker, S.; Schmiedel, A.; Holzapfel, M.; Lambert, C. Reduction of the Fluorescence Transition Dipole Moment by Excitation Localization in a Vibronically Coupled Squaraine Dimer. **2019**.

(38) Özçelik, S.; Akins, D. L. Superradiance of Aggregated Thiacarbocyanine Molecules. *J. Phys. Chem. B* **1999**, *103* (42), 8926–8929.

(39) Eisfeld, A.; Marquardt, C.; Paulheim, A.; Sokolowski, M. Superradiance from Two Dimensional Brick-Wall Aggregates of Dye Molecules: The Role of Size and Shape for the Temperature Dependence. *Phys. Rev. Lett.* **2017**, *119* (9), 097402.

(40) Meinardi, F.; Cerminara, M.; Sassella, A.; Bonifacio, R.; Tubino, R. Superradiance in

Molecular h Aggregates. *Phys. Rev. Lett.* **2003**, *91* (24).

(41) Kemnitz, K.; Yoshihara, K.; Suzumoto, T.; Tani, T.; Lindrum, M.; Moll, J.; Daehne, S. Primary Photophysical Processes InJ-Aggregates of Spectral Sensitisers. *J. Chem. Sci.* **1993**, *105* (6), 783–795.

(42) Haider, G.; Sampathkumar, K.; Verhagen, T.; Nádvorník, L.; Sonia, F. J.; Valeš, V.; Sýkora, J.; Kapusta, P.; Němec, P.; Hof, M.; et al. Superradiant Emission from Coherent Excitons in van Der Waals Heterostructures. *Adv. Funct. Mater.* **2021**, *31* (29).

(43) Friedman, H. C.; Cosco, E. D.; Atallah, T. L.; Sletten, E. M.; Caram, J. R. Establishing Design Principles for Emissive Organic SWIR Chromophores from Energy Gap Laws. *ChemRxiv* **2020**.

(44) Hilborn, R. C. Einstein Coefficients, Cross Sections, *f* Values, Dipole Moments, and All That. *Am. J. Phys.* **1982**, *50* (11), 982–986.

(45) Freyria, F. S.; Cordero, J. M.; Caram, J. R.; Doria, S.; Dodin, A.; Chen, Y.; Willard, A. P.; Bawendi, M. G. Near-Infrared Quantum Dot Emission Enhanced by Stabilized Self-Assembled J-Aggregate Antennas. *Nano Lett. 0* (0), null.

(46) Wang, C.; Weiss, E. A. Accelerating FRET between Near-Infrared Emitting Quantum Dots Using a Molecular J-Aggregate as an Exciton Bridge. *Nano Lett.* **2017**, *17* (9), 5666–5671.

(47) Wang, C.; Weiss, E. A. Sub-Nanosecond Resonance Energy Transfer in the Near-Infrared within Self-Assembled Conjugates of PbS Quantum Dots and Cyanine Dye J-Aggregates. *J. Am. Chem. Soc.* **2016**, *138* (30), 9557–9564.

(48) West, W.; Carroll, B. H. Energy Transfer in the Photo-Sensitization of Silver Halide Photographic Emulsions: Optical Sensitization, Supersensitization, and Antisensitization. *J. Chem. Phys.* **1951**, *19* (4), 417–427.

(49) Herz, A. H. Aggregation of Sensitizing Dyes in Solution and Their Adsorption onto Silver Halides. *Adv. Colloid Interface Sci.* **1977**, *8* (4), 237–298.

(50) Balci, S.; Kucukoz, B.; Balci, O.; Karatay, A.; Kocabas, C.; Yaglioglu, G. Tunable Plexcitonic Nanoparticles: A Model System for Studying Plasmon-Exciton Interaction from the Weak to the Ultrastrong Coupling Regime. *ACS Photonics* **2016**, *3* (11), 2010–2016.

(51) Saikin, S. K.; Eisfeld, A.; Valleau, S.; Aspuru-Guzik, A. Photonics Meets Excitonics: Natural and Artificial Molecular Aggregates. *Nanophotonics* **2013**, *2* (1), 21–38.

(52) Walters, C. M.; Pao, C.; Gagnon, B. P.; Zamecnik, C. R.; Walker, G. C. Bright Surface-Enhanced Raman Scattering with Fluorescence Quenching from Silica Encapsulated J-Aggregate Coated Gold Nanoparticles. *Adv. Mater.* **2018**, *30* (5), 1705381.

(53) Chen, X.; Chen, Y. H.; Qin, J.; Zhao, D.; Ding, B.; Blaikie, R. J.; Qiu, M. Mode Modification of Plasmonic Gap Resonances Induced by Strong Coupling with Molecular Excitons. *Nano Lett.* **2017**, *17* (5), 3246–3251.

(54) Li, C.; Wu, F.; Jiang, P.; Wang, Y.; Wang, L.; Yu, L. Tunable Strong Plasmon-Exciton Coupling between Single Silver Nanocube Dimer and J-Aggregates. *Phys. B Condens. Matter* **2019**, *569*, 40–47.

(55) Wang, H.; Wang, H.-Y.; Bozzola, A.; Toma, A.; Panaro, S.; Raja, W.; Alabastri, A.;

Wang, L.; Chen, Q.-D.; Xu, H.-L.; et al. Dynamics of Strong Coupling between J-Aggregates and Surface Plasmon Polaritons in Subwavelength Hole Arrays. *Adv. Funct. Mater.* **2016**, *26* (34), 6198–6205.

(56) Hao, Y.-W.; Wang, H.-Y.; Jiang, Y.; Chen, Q.-D.; Ueno, K.; Wang, W.-Q.; Misawa, H.; Sun, H.-B. Hybrid-State Dynamics of Gold Nanorods/Dye J-Aggregates under Strong Coupling. *Angew. Chemie Int. Ed.* **2011**, *50* (34), 7824–7828.

(57) Vasa, P.; Wang, W.; Pomraenke, R.; Lammers, M.; Maiuri, M.; Manzoni, C.; Cerullo, G.; Lienau, C. Real-Time Observation of Ultrafast Rabi Oscillations between Excitons and Plasmons in Metal Nanostructures with J-Aggregates. *Nat. Photonics 2013 72* **2013**, *7* (2), 128–132.

(58) Freyria, F. S.; Cordero, J. M.; Caram, J. R.; Doria, S.; Dodin, A.; Chen, Y.; Willard, A. P.; Bawendi, M. G. Near-Infrared Quantum Dot Emission Enhanced by Stabilized Self-Assembled J-Aggregate Antennas. *Nano Lett.* **2017**, *17* (12), 7665–7674.

(59) Chunyan Tan; Evrim Atas; Jürgen G. Müller; Mauricio R. Pinto; Valeria D. Kleiman, * and; Schanze*, K. S. Amplified Quenching of a Conjugated Polyelectrolyte by Cyanine Dyes. *J. Am. Chem. Soc.* **2004**, *126* (42), 13685–13694.

(60) Sneyd, A. J.; Fukui, T.; Paleček, D.; Prodhan, S.; Wagner, I.; Zhang, Y.; Sung, J.; Collins, S. M.; Slater, T. J. A.; Andaji-Garmaroudi, Z.; et al. Efficient Energy Transport in an Organic Semiconductor Mediated by Transient Exciton Delocalization. *Sci. Adv.* **2021**, *7* (32).

(61) Eisfeld, A.; Briggs, J. S. Dye Aggregates in Luminescent Solar Concentrators. *Phys. Status Solidi Appl. Mater. Sci.* **2018**, *215* (2).

(62) Pozin, S. I.; Lypenko, D. A.; Perelygina, O. M.; Gribkova, O. L.; Prokhorov, V. V.; Mal'tsev, E. I. Polymer Composite with J-Aggregates of Polymethine Dye as a Charge-Transport Layer of Organic Light-Emitting Diode. *Inorg. Mater. Appl. Res. 2021 121* **2021**, *12* (1), 94–100.

(63) Imaging Through Haze For Security Systems | Sensors Unlimited https://www.sensorsinc.com/applications/general/imaging-through-haze (accessed Aug 17, 2021).

(64) Carr, J. A.; Franke, D.; Caram, J. R.; Perkinson, C. F.; Saif, M.; Askoxylakis, V.; Datta, M.; Fukumura, D.; Jain, R. K.; Bawendi, M. G.; et al. Shortwave Infrared Fluorescence Imaging with the Clinically Approved Near-Infrared Dye Indocyanine Green. *Proc. Natl. Acad. Sci. U. S. A.* **2018**, *115* (17), 4465–4470.

(65) Zhao, L.; Ren, X.; Yan, X. Assembly Induced Super-Large Red-Shifted Absorption: The Burgeoning Field of Organic near-Infrared Materials. *CCS Chemistry*. 2021, pp 678–693.

(66) Bouit, P. A.; Wetzel, G.; Berginc, G.; Loiseaux, B.; Toupet, L.; Feneyrou, P.; Bretonnière, Y.; Kamada, K.; Maury, O.; Andraud, C. Near IR Nonlinear Absorbing Chromophores with Optical Limiting Properties at Telecommunication Wavelengths. *Chem. Mater.* **2007**, *19* (22), 5325–5335.

(67) Cosco, E. D.; Spearman, A. L.; Ramakrishnan, S.; Lingg, J. G. P.; Saccomano, M.; Pengshung, M.; Arús, B. A.; Wong, K. C. Y.; Glasl, S.; Ntziachristos, V.; et al. Shortwave Infrared Polymethine Fluorophores Matched to Excitation Lasers Enable Non-Invasive, Multicolour in Vivo Imaging in Real Time. *Nat. Chem. 2020 1212* **2020**, *12* (12), 1123–1130.

(68) Cosco, E. D.; Arús, B. A.; Spearman, A. L.; Atallah, T. L.; Lim, I.; Leland, O. S.; Caram, J. R.; Bischof, T. S.; Bruns, O. T.; Sletten, E. M. Bright Chromenylium Polymethine Dyes Enable Fast, Four-Color In Vivo Imaging with Shortwave Infrared Detection. *J. Am. Chem. Soc.* **2021**, *143* (18), 6836–6846.

(69) Chen, W.; Cheng, C. A.; Cosco, E. D.; Ramakrishnan, S.; Lingg, J. G. P.; Bruns, O. T.; Zink, J. I.; Sletten, E. M. Shortwave Infrared Imaging with J-Aggregates Stabilized in Hollow Mesoporous Silica Nanoparticles. *J. Am. Chem. Soc.* **2019**, *141* (32), 12475–12480.

(70) Thimsen, E.; Sadtler, B.; Berezin, M. Y. Shortwave-Infrared (SWIR) Emitters for Biological Imaging: A Review of Challenges and Opportunities. *Nanophotonics* **2017**, *6* (5), 1043–1054.

(71) Naczynski, D. J.; Stafford, J. H.; Türkcan, S.; Jenkins, C.; Koh, A. L.; Sun, C.; Xing, L. Rare-Earth-Doped Nanoparticles for Short-Wave Infrared Fluorescence Bioimaging and Molecular Targeting of AVβ3-Expressing Tumors. *Mol. Imaging* **2018**, *17*.

(72) Izquierdo, E.; Robin, A.; Keuleyan, S.; Lequeux, N.; Lhuillier, E.; Ithurria, S. Strongly Confined HgTe 2D Nanoplatelets as Narrow Near-Infrared Emitters.

(73) Tenney, S. M.; Vilchez, V.; Sonnleitner, M. L.; Huang, C.; Friedman, H. C.; Shin, A. J.; Atallah, T. L.; Deshmukh, A. P.; Ithurria, S.; Caram, J. R. Mercury Chalcogenide Nanoplatelet–Quantum Dot Heterostructures as a New Class of Continuously Tunable Bright Shortwave Infrared Emitters. *J. Phys. Chem. Lett.* **2020**, *11* (9), 3473–3480.

(74) Cosco, E. D.; Caram, J. R.; Bruns, O. T.; Franke, D.; Day, R. A.; Farr, E. P.; Bawendi, M. G.; Sletten, E. M. Flavylium Polymethine Fluorophores for Near- and Shortwave Infrared

Imaging. *Angew. Chemie - Int. Ed.* **2017**, *56* (42), 13126–13129.

(75) Pascal, S.; Bellier, Q.; David, S.; Bouit, P. A.; Chi, S. H.; Makarov, N. S.; Le Guennic, B.; Chibani, S.; Berginc, G.; Feneyrou, P.; et al. Unraveling the Two-Photon and Excited-State Absorptions of Aza-BODIPY Dyes for Optical Power Limiting in the SWIR Band. *J. Phys. Chem. C* **2019**.

(76) Harrison, W. J.; Mateer, D. L.; Tiddy, G. J. T. Liquid-Crystalline j-Aggregates Formed by Aqueous Ionic Cyanine Dyes. *J. Phys. Chem.* **1996**, *100* (6), 2310–2321.

(77) Eisele, D. M.; Cone, C. W.; Bloemsma, E. A.; Vlaming, S. M.; van der Kwaak, C. G. F.; Silbey, R. J.; Bawendi, M. G.; Knoester, J.; Rabe, J. P.; Vanden Bout, D. A. Utilizing Redox-Chemistry to Elucidate the Nature of Exciton Transitions in Supramolecular Dye Nanotubes. *Nat. Chem.* **2012**, *4* (8), 655–662.

(78) Kirstein, S.; Möhwald, H. Herringbone Structure in Two-Dimensional Single Crystals of Cyanine Dyes. II. Optical Properties. *J. Chem. Phys* **1995**, *103*, 826.

(79) Doria, S.; Sinclair, T. S.; Klein, N. D.; Bennett, D. I. G.; Chuang, C.; Freyria, F. S.; Steiner, C. P.; Foggi, P.; Nelson, K. A.; Cao, J.; et al. Photochemical Control of Exciton Superradiance in Light-Harvesting Nanotubes. *ACS Nano* **2018**, *12* (5), 4556–4564.

(80) Fidder, H.; Knoester, J.; Wiersma, D. A. Optical Properties of Disordered Molecular Aggregates: A Numerical Study. *J. Chem. Phys.* **1991**, *95* (11), 7880–7890.

(81) Caram, J. R.; Doria, S.; Eisele, D. M.; Freyria, F. S.; Sinclair, T. S.; Rebentrost, P.; Lloyd, S.; Bawendi, M. G. Room-Temperature Micron-Scale Exciton Migration in a Stabilized Emissive Molecular Aggregate. *Nano Lett.* **2016**, *16* (11), 6808–6815.

(82) Lee, E. M. Y.; Tisdale, W. A.; Willard, A. P. Can Disorder Enhance Incoherent Exciton Diffusion? *J. Phys. Chem. B* **2015**, *119* (30), 9501–9509.

(83) De Boer, S.; Wiersma, D. A. Dephasing-Induced Damping of Superradiant Emission in J-Aggregates. *Chem. Phys. Lett.* **1990**, *165* (1), 45–53.

(84) Drobizhev, M. A.; Sapozhnikov, M. N.; Scheblykin, I. G.; Varnavsky, O. P.; Van Der Auweraer, M.; Vitukhnovsky, A. G. Relaxation and Trapping of Excitons in J-Aggregates of a Thiacarbocynine Dye. *Chem. Phys.* **1996**, *211* (1–3), 455–468.

(85) Kamalov, V. F.; Struganova, I. a.; Yoshihara, K. Temperature Dependent Radiative Lifetime of J-Aggregates. *J. Phys. Chem.* **1996**, *100* (21), 8640–8644.

(86) Tolbert, L. M.; Zhao, X. Beyond the Cyanine Limit: Peierls Distortion and Symmetry Collapse in a Polymethine Dye. *J. Am. Chem. Soc.* **1997**, *119* (14), 3253–3258.

(87) Pascal, S.; Haefele, A.; Monnereau, C.; Charaf-Eddin, A.; Jacquemin, D.; Le Guennic, B.; Andraud, C.; Maury, O. Expanding the Polymethine Paradigm: Evidence for the Contribution of a Bis-Dipolar Electronic Structure. *J. Phys. Chem. A* **2014**, *118* (23), 4038–4047.

(88) Eisele, D. M.; Arias, D. H.; Fu, X.; Bloemsma, E. A.; Steiner, C. P.; Jensen, R. A.; Rebentrost, P.; Eisele, H.; Tokmakoff, A.; Lloyd, S.; et al. Robust Excitons Inhabit Soft Supramolecular Nanotubes. *Proc. Natl. Acad. Sci.* **2014**, *111* (33), E3367–E3375.

(89) Berlepsch, H. V; Böttcher, C. Cryo-Transmission Electron Microscopy Reveals Mesoscopic H- and J-Aggregates of near Infrared Cyanine Dyes. *J. Photochem. Photobiol. A Chem.* **2010**, *214* (1), 16–21.

(90) Prokhorov, V. V; Perelygina, O. M.; Pozin, S. I.; Mal'tsev, E. I.; Vannikov, A. V. Polymorphism of Two-Dimensional Cyanine Dye J-Aggregates and Its Genesis: Fluorescence Microscopy and Atomic Force Microscopy Study. *J. Phys. Chem. B* **2015**, *119* (48), 15046–15053.

(91) V. Berlepsch, H.; Böttcher, C. Supramolecular Structure of TTBC J-Aggregates in Solution and on Surface. *Langmuir* **2013**, *29* (16), 4948–4958.

(92) Von Berlepsch, H.; Kirstein, S.; Böttcher, C. Supramolecular Structure of J-Aggregates of a Sulfonate Substituted Amphiphilic Carbocyanine Dye in Solution: Methanol-Induced Ribbon-to-Tubule Transformation. *J. Phys. Chem. B* **2004**, *108* (48), 18725–18733.

(93) Scholes, G. D.; Rumbles, G. Excitons in Nanoscale Systems. *Nat. Mater.* **2006**, *5* (11), 920–920.

(94) Cherniukh, I.; Rainò, G.; Stöferle, T.; Burian, M.; Travesset, A.; Naumenko, D.; Amenitsch, H.; Erni, R.; Mahrt, R. F.; Bodnarchuk, M. I.; et al. Perovskite-Type Superlattices from Lead Halide Perovskite Nanocubes. *Nature* **2021**, *593*.

(95) Yuning Hong; Y. Lam, J. W.; Zhong Tang, B. Aggregation-Induced Emission: Phenomenon, Mechanism and Applications. *Chem. Commun.* **2009**, *0* (29), 4332–4353.

(96) Chen, W.; Cheng, C.; Cosco, E.; Ramakrishnan, S.; Lingg, J.; Bruns, O.; Zink, J. I.; Sletten, E. Shortwave Infrared Imaging with J-Aggregates Stabilized in Hollow Mesoporous Silica Nanoparticles. *ChemRxiv* **2018**, DOI: 10.26434/chemrxiv.7503506.v1.

(97) Hansen, M. P.; Malchow, D. S. Overview of SWIR Detectors, Cameras, and Applications. *Proc. SPIE* **2008**, *6939*, 69390I.

(98) Thimsen, E.; Sadtler, B.; Berezin, M. Y. Shortwave-Infrared (SWIR) Emitters for Biological Imaging: A Review of Challenges and Opportunities. *Nanophotonics* **2017**, *6* (5), 1043–1054.

(99) Hong, G.; Antaris, A. L.; Dai, H. Near-Infrared Fluorophores for Biomedical Imaging. *Nat. Biomed. Eng.* **2017**, *1* (1), 0010.

(100) Levitz, A.; Marmarchi, F.; Henary, M. Introduction of Various Substitutions to the Methine Bridge of Heptamethine Cyanine Dyes: Via Substituted Dianil Linkers. *Photochem. Photobiol. Sci.* **2018**, *17* (10), 1409–1416.

(101) Bricks, J. L.; Kachkovskii, A. D.; Slominskii, Y. L.; Gerasov, A. O.; Popov, S. V. Molecular Design of near Infrared Polymethine Dyes: A Review. *Dye. Pigment.* **2015**, *121*, 238–255.

(102) Boyd, G. T. Applications Requirements for Nonlinear-Optical Devices and the Status of Organic Materials. *J. Opt. Soc. Am. B* **1989**, *6* (4), 685.

(103) Thomas, R.; Thomas, A.; Pullanchery, S.; Joseph, L.; Somasundaran, S. M.; Swathi, R. S.; Gray, S. K.; Thomas, K. G. Plexcitons: The Role of Oscillator Strengths and Spectral Widths in Determining Strong Coupling. *ACS Nano* **2017**, *12* (1), 402–415.

(104) Hilborn, R. C. Einstein Coefficients, Cross Sections, f Values, Dipole Moments, and All That. *Am. J. Phys.* **1982**, *50*, 982.

(105) Tong Zhu, Yan Wan, L. H. Direct Imaging of Frenkel Exciton Transport by Ultrafast Microscopy. *Acc. Chem. Res.* **2017**, *50*, 1725–1733.

(106) Kaiser, T. E.; Stepanenko, V.; Würthner, F. Fluorescent J-Aggregates of Core-Substituted

Perylene Bisimides: Studies on Structure−Property Relationship, Nucleation−Elongation Mechanism, and Sergeants-and-Soldiers Principle. *J. Am. Chem. Soc.* **2009**, *131* (19), 6719–6732.

(107) May, V; Kühn, O. *Charge and Energy Transfer Dynamics in Molecular Systems*, 3rd ed.; Wiley-VCH:Berlin, 2011.

(108) Nabetani, A.; Tomioka, A.; Tamaru, H.; Miyano, K. Optical Properties of Two-Dimensional Dye Aggregate. *J. Chem. Phys.* **1995**, *102* (13), 5109–5117.

(109) Bakalis, L. D.; Rubtsov, I.; Knoester, J. Absorption Spectra of Mixed Two-Dimensional Cyanine Aggregates on Silver Halide Substrates. *J. Chem. Phys.* **2002**, *117* (11), 5393–5403.

(110) Wolter, S.; Magnus Westphal, K.; Hempel, M.; Würthner, F.; Kühn, O.; Lochbrunner, S. Low Temperature Exciton Dynamics and Structural Changes in Perylene Bisimide Aggregates. *J. Chem. Phys.* **2017**, *50* (18), 184005.

(111) Kaufmann, C.; Kim, W.; Nowak-Król, A.; Hong, Y.; Kim, D.; Würthner, F. Ultrafast Exciton Delocalization, Localization, and Excimer Formation Dynamics in a Highly Defined Perylene Bisimide Quadruple π-Stack. *J. Am. Chem. Soc.* **2018**, *140* (12), 4253–4258.

(112) Wan, Y.; Stradomska, A.; Fong, S.; Guo, Z.; Schaller, R. D.; Wiederrecht, G. P.; Knoester, J.; Huang, L. Exciton Level Structure and Dynamics in Tubular Porphyrin Aggregates. *J. Phys. Chem. C* **2014**, *118* (43), 24854–24865.

(113) Zheng, C.; Zhong, C.; Collison, C. J.; Spano, F. C. Non-Kasha Behavior in Quadrupolar

Dye Aggregates: The Red-Shifted H-Aggregate. *J. Phys. Chem. C* **2019**, *123* (5), 3203–3215.

(114) Berlepsch, H. V; Böttcher, C. Tubular J-Aggregates of a New Thiacarbocyanine Cy5 Dye for the Far-Red Spectral Region – a Spectroscopic and Cryo-Transmission Electron Microscopy Study. *Phys. Chem. Chem. Phys.* **2018**, *20* (28), 18969–18977.

(115) Vitukhnovsky, A. G.; Lobanov, A. N.; Pimenov, A.; Yonezawa, Y.; Kometani, N.; Asami, K.; Yano, J. Absorption Spectra Simulation of Amalgamation-Type Cyanine Dye Aggregates in LB Films. *J. Lumin.* **2000**, *87* (89), 260–262.

(116) Clark, K. A.; Krueger, E. L.; Vanden Bout, D. A. Direct Measurement of Energy Migration in Supramolecular Carbocyanine Dye Nanotubes. *J. Phys. Chem. Lett.* **2014**, *5* (13), 2274–2282.

(117) Caram, J. R.; Doria, S.; Eisele, D. M.; Freyria, F. S.; Sinclair, T. S.; Rebentrost, P.; Lloyd, S.; Bawendi, M. G. Room-Temperature Micron-Scale Exciton Migration in a Stabilized Emissive Molecular Aggregate. *Nano Lett.* **2016**, *16* (11), 6808–6815.

(118) Eisele, D. M.; Berlepsch, H. V.; Böttcher, C.; Stevenson, K. J.; Vanden Bout, D. A.; Kirstein, S.; Rabe, J. P. Photoinitiated Growth of Sub-7 Nm Silver Nanowires within a Chemically Active Organic Nanotubular Template. *J. Am. Chem. Soc.* **2010**, *132* (7), 2104–2105.

(119) Scheblykin, I. G.; Sliusarenko, O. Y.; Lepnev, L. S.; Vitukhnovsky, A. G.; Auweraer, M. Van Der. Excitons in Molecular Aggregates of 3,3′-Bis-[3-Sulfopropyl]-5,5′-Dichloro-9-Ethylthiacarbocyanine (THIATS): Temperature Dependent Properties. *J. Phys. Chem. B* **2001**, *105*, 4636–4646.

(120) Scheblykin, I. G.; Bataiev, M. M.; Van der Auweraer, M.; Vitukhnovsky, A. G. Dimensionality and Temperature Dependence of the Radiative Lifetime of J-Aggregates with Davydov Splitting of the Exciton Band. *Chem. Phys. Lett.* **2000**, *316* (1–2), 37–44.

(121) Anantharaman, S. B.; Stöferle, T.; Nüesch, F. A.; Mahrt, R. F.; Heier, J. Exciton Dynamics and Effects of Structural Order in Morphology-Controlled J-Aggregate Assemblies. *Adv. Funct. Mater.* **2019**, *29* (21), 1806997.

(122) Misawa, K.; Ono, H.; Minoshima, K.; Kobayashi, T. New Fabrication Method for Highly Oriented J Aggregates Dispersed in Polymer Films. *Appl. Phys. Lett.* **1993**, *63* (5), 577–579.

(123) Takahashi, D.; Oda, H.; Izumi, T.; Hirohashi, R. Substituent Effects on Aggregation Phenomena in Aqueous Solution of Thiacarbocyanine Dyes. *Dye. Pigment.* **2005**, *66* (1), 1–6.

(124) Czikkely, V.; Försterling, H. D.; Kuhn, H. Light Absorption and Structure of Aggregates of Dye Molecules. *Chem. Phys. Lett.* **1970**, *6* (1), 11–14.

(125) Pandya, R.; Chen, R. Y. S.; Cheminal, A.; Thomas, T.; Thampi, A.; Tanoh, A.; Richter, J.; Shivanna, R.; Deschler, F.; Schnedermann, C.; et al. Observation of Vibronic-Coupling-Mediated Energy Transfer in Light-Harvesting Nanotubes Stabilized in a Solid-State Matrix. *J. Phys. Chem. Lett.* **2018**, *9* (18), 5604–5611.

(126) Mukamel, S. *Principles of Nonlinear Optical Spectroscopy*; Oxford University Press: New York, 1995.

(127) Heijs, D. J.; Malyshev, V. A.; Knoester, J. Thermal Broadening of the J-Band in

Disordered Linear Molecular Aggregates: A Theoretical Study. *J. Chem. Phys.* **2005**, *123* (14), 144507.

(128) Ma, J.; Cao, J. Förster Resonance Energy Transfer, Absorption and Emission Spectra in Multichromophoric Systems. I. Full Cumulant Expansions and System-Bath Entanglement. *J. Chem. Phys.* **2015**, *142* (9), 094106.

(129) Hestand, N. J.; Spano, F. C. Expanded Theory of H- and J-Molecular Aggregates: The Effects of Vibronic Coupling and Intermolecular Charge Transfer. *Chem. Rev.* **2018**, *118* (15), 7069–7163.

(130) Spano, F. C. Analysis of the UV/Vis and CD Spectral Line Shapes of Carotenoid Assemblies: Spectral Signatures of Chiral H-Aggregates. *J. Am. Chem. Soc.* **2009**, *131* (12), 4267–4278.

(131) Chuang, C.; Bennett, D. I. G.; Caram, J. R.; Aspuru-Guzik, A.; Bawendi, M. G.; Cao, J. Generalized Kasha's Scheme for Classifying Two-Dimensional Excitonic Molecular Aggregates: Temperature Dependent Absorption Peak Frequency Shift. *Arxiv* **2019**, arXiv:1901.01318v1.

(132) Kaiser, T. E.; Scheblykin, I. G.; Thomsson, D.; Wu, F. Temperature-Dependent Exciton Dynamics in J-AggregatessWhen Disorder Plays a Role. *J. Phys. Chem. B* **2009**, 15836–15842.

(133) Scholes, G. D.; Fleming, G. R.; Olaya-Castro, A.; van Grondelle, R. Lessons from Nature about Solar Light Harvesting. *Nat. Chem.* **2011**, *3* (10), 763–774.

(134) Nugraha, A. R. T.; Saito, R.; Sato, K.; Araujo, P. T.; Jorio, A.; Dresselhaus, M. S.

Dielectric Constant Model for Environmental Effects on the Exciton Energies of Single Wall Carbon Nanotubes. *Appl. Phys. Lett.* **2010**, *97* (9), 091905.

(135) Ferretti, M.; Hendrikx, R.; Romero, E.; Southall, J.; Cogdell, R. J.; Novoderezhkin, V. I.; Scholes, G. D.; Van Grondelle, R. Dark States in the Light-Harvesting Complex 2 Revealed by Two-Dimensional Electronic Spectroscopy. *Sci. Rep.* **2016**, *6* (1), 20834.

(136) Gao, X.; Eisfeld, A. Near-Field Spectroscopy of Nanoscale Molecular Aggregates. *J. Phys. Chem. Lett.* **2018**, *9* (20), 6003–6010.

(137) Nasr, C.; Liu, D.; Hotchandani, S.; Kamat, P. V. Dye-Capped Semiconductor Nanoclusters. Excited State and Photosensitization Aspects of Rhodamine 6G H-Aggregates Bound to SiO2 and SnO2 Colloids. *J. Phys. Chem.* **1996**, *100* (26), 11054–11061.

(138) Barazzouk, S.; Lee, H.; Hotchandani, S.; Kamat, P. V. Photosensitization Aspects of Pinacyanol H-Aggregates. Charge Injection from Singlet and Triplet Excited States into SnO 2 Nanocrystallites. *J. Phys. Chem. B* **2000**, *104* (15), 3616–3623.

(139) Lambert, C.; Koch, F.; Völker, S. F.; Schmiedel, A.; Holzapfel, M.; Humeniuk, A.; Röhr, M. I. S.; Mitric, R.; Brixner, T. Energy Transfer Between Squaraine Polymer Sections: From *Helix* to *Zigzag* and All the Way Back. *J. Am. Chem. Soc.* **2015**, *137* (24), 7851–7861.

(140) Turro, N. J.; Ramamurthy, V.; Scaiano, J. C. *Principles of Molecular Photochemistry : An Introduction*; University Science Books: Sausalito, 2009.

(141) Lotya, M.; Rakovich, A.; Donegan, J. F.; Coleman, J. N. Measuring the Lateral Size of

Liquid-Exfoliated Nanosheets with Dynamic Light Scattering. *Nanotechnology* **2013**, *24* (26), 265703.

(142) Frisch, M. J.; Trucks, G. W.; Schlegel, H. B.; Scuseria, G. E.; Robb, M. A.; Cheeseman, J. R.; Scalmani, G.; Barone, V.; Petersson, G. A.; Nakatsuji, H.; et al. Gaussian16 {R}evision {B}.01. 2016.

(143) Allec, S. I.; Ilawe, N. V; Wong, B. M. Unusual Bandgap Oscillations in Template-Directed φ-Conjugated Porphyrin Nanotubes. *J. Phys. Chem. Lett.* **2016**, *7* (13), 2362–2367.

(144) Davydov, A. S. THE THEORY OF MOLECULAR EXCITONS. *Sov. Phys. Uspekhi* **1964**, *7* (2), 145–178.

(145) Deshmukh, A. P.; Koppel, D.; Chuang, C.; Cadena, D. M.; Cao, J.; Caram, J. R. Design Principles for Two-Dimensional Molecular Aggregates Using Kasha's Model: Tunable Photophysics in Near and Short-Wave Infrared. *J. Phys. Chem. C* **2019**, *123* (30), 18702–18710.

(146) Sun, C.; Li, B.; Zhao, M.; Wang, S.; Lei, Z.; Lu, L.; Zhang, H.; Feng, L.; Dou, C.; Yin, D.; et al. J-Aggregates of Cyanine Dye for NIR-II in Vivo Dynamic Vascular Imaging beyond 1500 Nm. *J. Am. Chem. Soc.* **2019**, *141* (49), 19221–19225.

(147) Cacciola, A.; Triolo, C.; Di Stefano, O.; Genco, A.; Mazzeo, M.; Saija, R.; Patanè, S.; Savasta, S. Subdiffraction Light Concentration by J-Aggregate Nanostructures. *ACS Photonics* **2015**, *2* (7), 971–979.

(148) Zhong, X.; Chervy, T.; Wang, S.; George, J.; Thomas, A.; Hutchison, J. A.; Devaux, E.;

Genet, C.; Ebbesen, T. W. Non-Radiative Energy Transfer Mediated by Hybrid Light-Matter States. *Angew. Chemie - Int. Ed.* **2016**, *55* (21), 6202–6206.

(149) Scheblykin, I. G.; Varnavsky, O. P.; Verbouwe, W.; De Backer, S.; Van Der Auweraer, M.; Vitukhnovsky, A. G. Relaxation Dynamics of Excitons in J-Aggregates Revealing a Two-Component Davydov Splitting. *Chem. Phys. Lett.* **1998**, *282* (3–4), 250–256.

(150) Yamaguchi, A.; Kotnetani, N.; Yonezawa, Y. Luminescence Properties of the Mixed J-Aggregate of Oxacyanine Dye and Thiacyanine Dye. Formation of a Persistence-Type Aggregate. *J. Phys. Chem. B* **2005**, *109* (4), 1408–1414.

(151) Debnath, P.; Chakraborty, S.; Deb, S.; Nath, J.; Dey, B.; Bhattacharjee, D.; Soda, H.; Tominaga, M.; Suzuki, Y.; Kawamata, J.; et al. Effect of Nano Clay Laponite on Stability of SHG Active J-Aggregate of a Thiacyanine Dye onto LB Films. *Appl. Clay Sci.* **2017**, *147*, 105–116.

(152) Laban, B.; Vodnik, V.; Dramićanin, M.; Novaković, M.; Bibić, N.; Sovilj, S. P.; Vasić, V. M. Mechanism and Kinetics of J-Aggregation of Thiacyanine Dye in the Presence of Silver Nanoparticles. *J. Phys. Chem. C* **2014**, *118* (40), 23393–23401.

(153) Zhang, F.; Sautter, K.; Larsen, A. M.; Findley, D. A.; Davis, R. C.; Samha, H.; Linford, M. R. Chemical Vapor Deposition of Three Aminosilanes on Silicon Dioxide: Surface Characterization, Stability, Effects of Silane Concentration, and Cyanine Dye Adsorption. *Langmuir* **2010**, *26* (18), 14648–14654.

(154) Oh, J. W.; Kumazaki, S.; Rubtsov, I. V.; Suzumoto, T.; Tani, T.; Yoshihara, K. Ultrafast Energy Transfer in J-Aggregate on AgBr Microcrystals: Its Dependence on Dye Coverage. *Chem. Phys. Lett.* **2002**, *352* (5–6), 357–362.

(155) Hasegawa, D.; Nakata, K.; Tokunaga, E.; Okamura, K.; Du, J.; Kobayashi, T. Vibrational Energy Flow between Modes by Dynamic Mode Coupling in THIATS J-Aggregates. *J. Phys. Chem. A* **2013**, *117* (45), 11441–11448.

(156) Tanaka, Y.; Yoshikawa, H.; Masuhara, H. Thiacarbocyanine Dye J-Aggregation in Optical Trapping Potential. In *Optical Trapping and Optical Micromanipulation III*; Dholakia, K., Spalding, G. C., Eds.; SPIE, 2006; Vol. 6326, p 63262J.

(157) Chevrier, K.; Benoit, J. M.; Symonds, C.; Paparone, J.; Laverdant, J.; Bellessa, J. Organic Exciton in Strong Coupling with Long-Range Surface Plasmons and Waveguided Modes. *ACS Photonics* **2018**, *5* (1), 80–84.

(158) Prokhorov, V. V.; Pozin, S. I.; Lypenko, D. A.; Perelygina, O. M.; Mal'tsev, E. I.; Vannikov, A. V. Molecular Arrangements in Two-Dimensional J-Aggregate Monolayers of Cyanine Dyes. *Macroheterocycles* **2012**, *5* (4–5), 371–376.

(159) Kirstein, S.; Möhwald, H.; Shimomura, M. Crystalline Two-Dimensional Domains of Cyanine Dyes at Interfaces. *Chem. Phys. Lett.* **1989**, *154* (4), 303–308.

(160) Kim, O. K.; Je, J.; Jernigan, G.; Buckley, L.; Whitten, D. Super-Helix Formation Induced by Cyanine J-Aggregates onto Random-Coil Carboxymethyl Amylose as Template. *J. Am. Chem. Soc.* **2006**, *128* (2), 510–516.

(161) Garoff, R. A.; Litzinger, E. A.; Connor, R. E.; Fishman, I.; Armitage, B. A. Helical Aggregation of Cyanine Dyes on DNA Templates: Effect of Dye Structure on Formation of Homo- and Heteroaggregates. *Langmuir* **2002**, *18* (16), 6330–6337.

(162) Hannah, K. C.; Armitage, B. A. DNA-Templated Assembly of Helical Cyanine Dye

Aggregates: A Supramolecular Chain Polymerization. *Acc. Chem. Res.* **2004**, *37* (11), 845–853.

(163) Chuang, C.; Bennett, D. I. G.; Caram, J. R.; Aspuru-Guzik, A.; Bawendi, M. G.; Cao, J. Generalized Kasha's Model: T-Dependent Spectroscopy Reveals Short-Range Structures of 2D Excitonic Systems. *Chem* **2019**, *5* (12), 3135–3150.

(164) Eisele, D. M.; Knoester, J.; Kirstein, S.; Rabe, J. P.; Vanden Bout, D. A. Uniform Exciton Fluorescence from Individual Molecular Nanotubes Immobilized on Solid Substrates. *Nat. Nanotechnol.* **2009**, *4* (10), 658–663.

(165) Chen, Z.; Lohr, A.; Saha-Möller, C. R.; Würthner, F. Self-Assembled π-Stacks of Functional Dyes in Solution: Structural and Thermodynamic Features. *Chem. Soc. Rev.* **2009**, *38* (2), 564–584.

(166) Kopainsky, B.; Hallermeier, J. K.; Kaiser, W. The First Step of Aggregation of Pic: The Dimerization. *Chem. Phys. Lett.* **1981**, *83* (3), 498–502.

(167) Ben-Shaul, A.; Gelbart, W. M. Statistical Thermodynamics of Amphiphile Self-Assembly: Structure and Phase Transitions in Micellar Solutions. In *Micelles, Membranes, Microemulsions, and Monolayers*; Gelbart, W. M., Ben-Shaul, A., Roux, D., Eds.; Springer: New York, NY, 1994; pp 1–104.

(168) Israelachvili, J. N. *Intermolecular and Surface Forces*, 3rd ed.; Elsevier, 2011.

(169) Montcuquet, A. S.; Hervé, L.; Navarro, F.; Dinten, J. M.; Mars, J. I. In Vivo Fluorescence Spectra Unmixing and Autofluorescence Removal by Sparse Nonnegative Matrix Factorization. *IEEE Trans. Biomed. Eng.* **2011**, *58* (9), 2554–2565.

(170) Smulders, M. M. J.; Nieuwenhuizen, M. M. L.; De Greef, T. F. A.; Van Der Schoot, P.; Schenning, A. P. H. J.; Meijer, E. W. How to Distinguish Isodesmic from Cooperative Supramolecular Polymerisation. *Chem. - A Eur. J.* **2010**, *16* (1), 362–367.

(171) Fukui, T.; Kawai, S.; Fujinuma, S.; Matsushita, Y.; Yasuda, T.; Sakurai, T.; Seki, S.; Takeuchi, M.; Sugiyasu, K. Control over Differentiation of a Metastable Supramolecular Assembly in One and Two Dimensions. *Nat. Chem.* **2017**, *9* (5), 493–499.

(172) Prokhorov, V. V.; Mal'tsev, E. I.; Perelygina, O. M.; Lypenko, D. A.; Pozin, S. I.; Vannikov, A. V. High Precision Nanoscale AFM Height Measurements of J-Aggregates. *Nanotechnologies Russ. 2011 65* **2011**, *6* (5), 286–297.

(173) Kriete, B.; Feenstra, C. J.; Pshenichnikov, M. S. Microfluidic Out-of-Equilibrium Control of Molecular Nanotubes. *Phys. Chem. Chem. Phys.* **2020**, *22* (18), 10179–10188.

(174) Gibbs, H. M.; Khitrova, G.; Koch, S. W. Exciton–Polariton Light–Semiconductor Coupling Effects. *Nat. Photonics* **2011**, *5* (5), 273–273.

(175) Sun, C.; Li, B.; Zhao, M.; Wang, S.; Lei, Z.; Lu, L.; Zhang, H.; Feng, L.; Dou, C.; Yin, D.; et al. J-Aggregates of Cyanine Dye for NIR-II in Vivo Dynamic Vascular Imaging beyond 1500 Nm. *J. Am. Chem. Soc.* **2019**, *141* (49), 19221–19225.

(176) Scheblykin, I. G.; Bataiev, M. M.; Van Der Auweraer, M.; Vitukhnovsky, A. G. Dimensionality and Temperature Dependence of the Radiative Lifetime of J-Aggregates with Davydov Splitting of the Exciton Band. *Chem. Phys. Lett.* **2000**, *316* (1–2), 37–44.

(177) Yefimova, S. L.; Grygorova, G. V; Klochkov, V. K.; Borovoy, I. A.; Sorokin, A. V; Malyukin, Y. V. Molecular Arrangement in Cyanine Dye J-Aggregates Formed on CeO2

Nanoparticles. *J. Phys. Chem. C* **2018**, *122* (36), 20996–21003.

(178) Bradbury, N. C.; Chuang, C.; Deshmukh, A. P.; Rabani, E.; Baer, R.; Caram, J. R.; Neuhauser, D. Stochastically Realized Observables for Excitonic Molecular Aggregates. *J. Phys. Chem. A* **2020**, *124* (49), 10111–10120.

(179) Clark, J.; Silva, C.; Friend, R. H.; Spano, F. C. Role of Intermolecular Coupling in the Photophysics of Disordered Organic Semiconductors: Aggregate Emission in Regioregular Polythiophene. *Phys. Rev. Lett.* **2007**, *98* (20), 206406.

(180) Marques, S. R.; Labastide, J. A.; Barnes, M. D. Evolution of HJ Coupling in Nanoscale Molecular Self-Assemblies. *J. Phys. Chem. C* **2018**, *122* (27), 15723–15728.

(181) Oleson, A.; Zhu, T.; Dunn, I. S.; Bialas, D.; Bai, Y.; Zhang, W.; Dai, M.; Reichman, D. R.; Tempelaar, R.; Huang, L.; et al. Perylene Diimide-Based Hj- and HJ-Aggregates: The Prospect of Exciton Band Shape Engineering in Organic Materials. *J. Phys. Chem. C* **2019**, *123* (33), 20567–20578.

(182) Wang Li-Li Li Editors, H. *Nanomedicine and Nanotoxicology In Vivo Self-Assembly Nanotechnology for Biomedical Applications*.

(183) Ghosh, B.; Mardanya, S.; Singh, B.; Zhou, X.; Wang, B.; Chang, T.-R.; Su, C.; Lin, H.; Agarwal, A.; Bansil, A. Saddle-Point Van Hove Singularity and Dual Topological State in ${\rm Pt}_{2}{\rm HgSe}_{3}$. *Phys. Rev. B* **2019**, *100*, 235101.

(184) Xing, D. Y.; Liu, M.; Gong, C. D. Comment on Anomalous Isotope Effect and van Hove Singularity in Superconducting Cu Oxides. *Physical Review Letters*. 1992, p 1090.

(185) Li, G.; Luican, A.; Lopes Dos Santos, J. M. B.; Castro Neto, A. H.; Reina, A.; Kong, J.;

Andrei, E. Y. Observation of Van Hove Singularities in Twisted Graphene Layers. *Nat. Phys.* **2009**.

(186) Deshmukh, A. P.; Bailey, A. D.; Forte, L. S.; Shen, X.; Geue, N.; Sletten, E. M.; Caram, J. R. Thermodynamic Control over Molecular Aggregate Assembly Enables Tunable Excitonic Properties across the Visible and Near-Infrared. *J. Phys. Chem. Lett.* **2020**, *11* (19), 8026–8033.

(187) Moll, J.; Daehne, S.; Durrant, J. R.; Wiersma, D. A. Optical Dynamics of Excitons in J Aggregates of a Carbocyanine Dye. *J. Chem. Phys.* **1995**, *102* (16), 6362–6370.

(188) Sorokin, A. V.; Ropakova, I. Y.; Grynyov, R. S.; Vilkisky, M. M.; Liakh, V. M.; Borovoy, I. A.; Yefimova, S. L.; Malyukin, Y. V. Strong Difference between Optical Properties and Morphologies for J-Aggregates of Similar Cyanine Dyes. *Dye. Pigment.* **2018**, *152*, 49–53.

(189) Heijs, D. J.; Malyshev, V. A.; Knoester, J. Decoherence of Excitons in Multichromophore Systems: Thermal Line Broadening and Destruction of Superradiant Emission. *Phys. Rev. Lett.* **2005**, *95* (17), 177402.

(190) Mattoon, R. W. Polymer Spectra of a Cyanine Dye. *J. Chem. Phys.* **2004**, *12* (6), 268.

(191) Renge, I.; Wild, U. P. Solvent, Temperature, and Excitonic Effects in the Optical Spectra of Pseudoisocyanine Monomer and J-Aggregates. *J. Phys. Chem. A* **1997**, *101* (43), 7977–7988.

(192) Dijkstra, A. G.; Duan, H.-G.; Knoester, J.; Nelson, K. A.; Cao, J. How Two-Dimensional Brick Layer J-Aggregates Differ from Linear Ones: Excitonic Properties and Line

Broadening Mechanisms. *J. Chem. Phys.* **2016**, *144* (13), 134310.

(193) Chuang, C.; Cao, J. Universal Scalings in Two-Dimensional Anisotropic Dipolar Excitonic Systems. *Phys. Rev. Lett.* **2021**, *127*.

(194) Gu, Q.; Kenny, J. E. Improvement of Inner Filter Effect Correction Based on Determination of Effective Geometric Parameters Using a Conventional Fluorimeter. *Anal. Chem.* **2009**, *81* (1), 420–426.

(195) Würth, C.; Grabolle, M.; Pauli, J.; Spieles, M.; Resch-Genger, U. Relative and Absolute Determination of Fluorescence Quantum Yields of Transparent Samples. *Nat. Protoc. 2013 88* **2013**, *8* (8), 1535–1550.

(196) Lim, I.; Vian, A.; Wouw, H. L. van de; Day, R. A.; Gomez, C.; Liu, Y.; Rheingold, A. L.; Campàs, O.; Sletten, E. M. Fluorous Soluble Cyanine Dyes for Visualizing Perfluorocarbons in Living Systems. *J. Am. Chem. Soc.* **2020**, *142* (37), 16072–16081.

(197) Atallah, T. L.; Sica, A. V.; Shin, A. J.; Friedman, H. C.; Kahrobai, Y. K.; Caram, J. R. Decay-Associated Fourier Spectroscopy: Visible to Shortwave Infrared Time-Resolved Photoluminescence Spectra. *J. Phys. Chem. A* **2019**, *123* (31), 6792–6798.

(198) Brent P. Krueger; Gregory D. Scholes, and; Fleming*, G. R. Calculation of Couplings and Energy-Transfer Pathways between the Pigments of LH2 by the Ab Initio Transition Density Cube Method. *J. Phys. Chem. B* **1998**, *102* (27), 5378–5386.

(199) De Rossi, U.; Moll, J.; Spieles, M.; Bach, G.; D??hne, S.; Kriwanek, J.; Lisk, M. Control of the J-Aggregation Phenomenon by Variation of the N-Alkyl-Substituents. *J. fur Prakt. Chemie/Chemiker-Zeitung* **1995**, *337* (1), 203–208.

(200) Pawlik, A.; Ouart, A.; Kirstein, S.; Abraham, H. W.; Daehne, S. Synthesis and UV/Vis Spectra of J-Aggregating 5,5′,6,6′-Tetrachlorobenzimidacarbocyanine Dyes for Artificial Light-Harvesting Systems and for Asymmetrical Generation of Supramolecular Helices. *European J. Org. Chem.* **2003**, *2003* (16), 3065–3080.

(201) Kirstein, S.; von Berlepsch, H.; Böttcher, C.; Burger, C.; Ouart, A.; Reck, G.; Dähne, S. Chiral J-Aggregates Formed by Achiral Cyanine Dyes. *ChemPhysChem* **2000**, *1* (3), 146–150.

(202) Clark, K. A.; Cone, C. W.; Bout, D. A. Vanden. Quantifying the Polarization of Exciton Transitions in Double-Walled Nanotubular J-Aggregates. *J. Phys. Chem. C* **2013**, *117* (50), 26473–26481.

(203) Schade, B.; Singh, A. K.; Wycisk, V.; Cuellar-Camacho, J. L.; Berlepsch, H.; Haag, R.; Böttcher, C. Stereochemistry-Controlled Supramolecular Architectures of New Tetrahydroxy-Functionalised Amphiphilic Carbocyanine Dyes. *Chem. – A Eur. J.* **2020**, *26* (30), 6919–6934.

(204) Roodenko, K.; Nguyen, H. M.; Caillard, L.; Radja, A.; Thissen, P.; Gordon, J. M.; Gartstein, Y. N.; Malko, A. V; Chabal, Y. J. Anisotropic Optical Properties of Thin-Film Thiacarbocyanine Dye Aggregates. *J. Phys. Chem. C* **2013**, *117* (39), 20186–20192.

(205) Patmanidis, I.; de Vries, A. H.; Wassenaar, T. A.; Wang, W.; Portale, G.; Marrink, S. J. Structural Characterization of Supramolecular Hollow Nanotubes with Atomistic Simulations and SAXS. *Phys. Chem. Chem. Phys.* **2020**, *22* (37), 21083–21093.

(206) von Berlepsch, H.; Kirstein, S.; Hania, R.; Pugžlys, A.; Böttcher, C. Modification of the Nanoscale Structure of the J-Aggregate of a Sulfonate-Substituted Amphiphilic

Carbocyanine Dye through Incorporation of Surface-Active Additives. *J. Phys. Chem. B* **2007**, *111* (7), 1701–1711.

(207) Lyon, J. L.; Eisele, D. M.; Kirstein, S.; Rabe, J. P.; Vanden Bout, D. A.; Stevenson, K. J. Spectroelectrochemical Investigation of Double-Walled Tubular J-Aggregates of Amphiphilic Cyanine Dyes. *J. Phys. Chem. C* **2008**, *112* (4), 1260–1268.

(208) Berlepsch, H. V; Ludwig, K.; Kirstein, S.; Böttcher, C. Mixtures of Achiral Amphiphilic Cyanine Dyes Form Helical Tubular J-Aggregates. *Chem. Phys.* **2011**, *385* (1–3), 27–34.

(209) Megow, J.; Röhr, M. I. S.; Schmidt am Busch, M.; Renger, T.; Mitrić, R.; Kirstein, S.; Rabe, J. P.; May, V. Site-Dependence of van Der Waals Interaction Explains Exciton Spectra of Double-Walled Tubular J-Aggregates. *Phys. Chem. Chem. Phys.* **2015**, *17* (10), 6741–6747.

(210) Kriete, B.; Bondarenko, A. S.; Jumde, V. R.; Franken, L. E.; Minnaard, A. J.; Jansen, T. L. C.; Knoester, J.; Pshenichnikov, M. S. Steering Self-Assembly of Amphiphilic Molecular Nanostructures via Halogen Exchange. *J. Phys. Chem. Lett.* **2017**, *8* (13), 2895–2901.

(211) Bondarenko, A. S.; Patmanidis, I.; Alessandri, R.; Souza, P. C. T.; Jansen, T. L. C.; De Vries, A. H.; Marrink, S. J.; Knoester, J. Multiscale Modeling of Molecular Structure and Optical Properties of Complex Supramolecular Aggregates. *Chem. Sci.* **2020**, *11* (42), 11514–11524.

(212) Egelman, E. H. The Iterative Helical Real Space Reconstruction Method: Surmounting the Problems Posed by Real Polymers. *J. Struct. Biol.* **2007**, *157* (1), 83–94.

(213) Dubochet, J.; McDowall, A. W. VITRIFICATION OF PURE WATER FOR ELECTRON MICROSCOPY. *J. Microsc.* **1981**, *124* (3), 3–4.

(214) Dobro, M. J.; Melanson, L. A.; Jensen, G. J.; McDowall, A. W. Plunge Freezing for Electron Cryomicroscopy. *Methods Enzymol.* **2010**, *481* (C), 63–82.

(215) Egelman, E. H. A Robust Algorithm for the Reconstruction of Helical Filaments Using Single-Particle Methods. *Ultramicroscopy* **2000**, *85* (4), 225–234.

(216) Egelman, E. H. Reconstruction of Helical Filaments and Tubes. *Methods Enzymol.* **2010**, *482* (C), 167–183.

(217) Egelman, E. H. Ambiguities in Helical Reconstruction. *Elife* **2014**, *3*.

(218) Emsley, P.; Lohkamp, B.; Scott, W. G.; Cowtan, K. Features and Development of Coot. *Acta Crystallogr. Sect. D Biol. Crystallogr.* **2010**, *66* (4), 486–501.

(219) Adams, P. D.; Afonine, P. V.; Bunkóczi, G.; Chen, V. B.; Davis, I. W.; Echols, N.; Headd, J. J.; Hung, L. W.; Kapral, G. J.; Grosse-Kunstleve, R. W.; et al. PHENIX: A Comprehensive Python-Based System for Macromolecular Structure Solution. *Acta Crystallogr. Sect. D Biol. Crystallogr.* **2010**, *66* (2), 213–221.

(220) Zivanov, J.; Nakane, T.; Forsberg, B. O.; Kimanius, D.; Hagen, W. J. H.; Lindahl, E.; Scheres, S. H. W. New Tools for Automated High-Resolution Cryo-EM Structure Determination in RELION-3. *Elife* **2018**, *7*.

(221) Goddard, T. D.; Huang, C. C.; Ferrin, T. E. Visualizing Density Maps with UCSF Chimera. *J. Struct. Biol.* **2007**, *157* (1), 281–287.

(222) Caram, J. R.; Bertram, S. N.; Utzat, H.; Hess, W. R.; Carr, J. A.; Bischof, T. S.; Beyler, A.

P.; Wilson, M. W. B.; Bawendi, M. G. PbS Nanocrystal Emission Is Governed by Multiple Emissive States. *Nano Lett.* **2016**, *16* (10), 6070–6077.

(223) Cui, J.; Beyler, A. P.; Bischof, T. S.; Wilson, M. W. B.; Bawendi, M. G. Deconstructing the Photon Stream from Single Nanocrystals: From Binning to Correlation. *Chem. Soc. Rev.* **2014**, *43* (4), 1287–1310.

(224) Feyter, S. D.; Schryver, F. C. D. Two-Dimensional Supramolecular Self-Assembly Probed by Scanning Tunneling Microscopy. *Chem. Soc. Rev.* **2003**, *32* (3), 139–150.